RICE UNIVERSITY

Investigation of Electrically Driven Transition in Magnetite, Fe_3O_4, Nanostructures

by

Alexandra Fursina

A Thesis Submitted
in Partial Fulfillment of the
Requirements for the Degree
Doctor of Philosophy

Approved, Thesis Committee:

Douglas Natelson, Chair
Associate Professor of Physics and Astronomy and Electrical and Computer Engineering

Jason Hafner
Associate Professor of Physics and Astronomy and Chemistry

Emilia Morosan
Assistant Professor of of Physics and Astronomy

Stephan Link
Assistant Professor of Chemistry and Electrical and Computer Engineering

Houston, Texas
May, 2010

Abstract

Investigation of Electrically Driven Transition in Magnetite, Fe_3O_4, Nanostructures

by

Alexandra A. Fursina

Magnetite, Fe_3O_4, is a strongly electronically correlated system and thus exhibits remarkable electrical and magnetic properties, including the Verwey transition at T_V 122 K, which has attracted much attention since its 1939 discovery. Fe_3O_4 has recently revealed a new effect. By performing experiments at the nanoscale, we have discovered a novel electric-field driven transition (EFD) in magnetite below T_V, from high- to low-resistance states driven by application of high bias. The EFD transition is detected both in Fe_3O_4 nanoparticles and thin films, is hysteretic in voltage under continuous biasing, and is not caused by self-heating. In this thesis we report on a thorough investigation of this new EFD transition. First, we unveil the origin of hysteresis observed in I-V curves. By applying voltage in a pulsed manner with controlled parameters, we unambiguously demonstrate that while the transition is field-driven, hysteresis results from Joule heating in the low-resistance state. A simple relaxation-time thermal model captures the essentials of the hysteresis mechanism. Second, by doing multilead (four-terminal) electrical measurements, we quantitatively separate the contributions of the Fe_3O_4 channel and each metal/electrode interface, and explore the contact effects upon testing devices incorporating various contact metals. We demonstrate that on the onset of the transition, contact resistances

at both source and drain electrodes and the resistance of Fe_3O_4 channel decrease abruptly. Finally, we measured the distribution of switching voltages, V_{sw}, its evolution with temperature, and its dependence on out-of-plane magnetic field. Based on the experimental facts collected in this work we suggest the possible mechanism of EFD transition in Fe_3O_4 as a charge gap closure by electric field. This is one of the first experimental observation of a theoretically predicted EFD transition in correlated insulators. These studies demonstrate that nanoscale, nonequilibrium probes can reveal much about the underlying physics of strongly correlated materials.

Acknowledgments

First of all I would like to thank my advisor, Prof. Douglas Natelson, for his excellent guidance as a mentor and patience and understanding as a human for the past 3.5 years of working in his lab. I am very grateful to him for giving me a project which perfectly suited my character and brought me a real joy to work on. I would like to thank Prof. Jason Hafner, Prof. Emilia Morosan and Prof. Stephan Link for taking their valuable time on reading this manuscript and attending the oral defense.

I also thank our research collaborators, Prof. Igor Shvets and Dr. Sumesh Sofin, who literally were laying the foundation of this work by growing high quality magnetite thin film to be investigated in this work. I also greatly appreciate their helpful discussions and valuable comments on our papers. I am grateful to my lab mates for the lab assistance and the discussions.

Out of numerous wonderful teachers I was lucky to meet and be taught in my life I would like to specially thank two persons: my Chemistry teacher Viktor Ya. Bashmakov for his incredible knowledge of chemistry and for his kindness and wisdom; and my figure skating coach Nataliya N. Burmagina for giving me an appreciation of a fair sport competition and making me a fighter both in sport and in life. I am thankful to my *alma mater*, Lomonosov Moscow State University, for teaching me the right approaches in learning, researching and teaching. I owe it the great happiness of meeting my best friends there.

I cannot thank enough my family: my the very the best parents, sister and grandparents. Without their everlasting love and care this journey would not have been possible. Finally, I would like to thank my husband Alex for support and patience and my little daughter Vicki whose angel sleeping face has been inspiring me during writing this thesis.

Contents

Illustrations

Preface

The primary interest of our laboratory research is electrical measurements at the nanoscale. This includes the investigation of a variety of objects by different methods, such as detection and characterization of a single molecule in electromigrated gaps by mean of surface-enhanced Raman spectroscopy [16] and by single molecule transistor measurements [17]; addressing contacts effect of polymer semiconductors (such as P3HT [18]); measurement of Kondo effect [19] and inelastic electron tunneling in single molecule transistors [20]; quantum corrections to the electrical conduction of magnetic semiconductors [21], etc.

Any investigation of electrical properties at the nanoscale inevitably consists of two steps: first, fabrication of a device (create a reliable and well-defined contact between investigated object and external electrodes) and, second, the actual measurement. In many cases device fabrication implies the "trapping" of the investigated object (nanoparticle, molecule, etc.) between two electrodes. Clearly, nanosized objects demand metallic electrodes separated by a distance comparable with the targeted length, *i.e*, a few nanometers.

There might be some confusion while discussing the "length" and the "width" of the gaps (several references have different terminology). In this thesis we work with devices in lateral, planar configuration and the length, L, of the gap is defined as the distance between two electrodes, while the width, W, of the gap is the lateral dimension of the electrode (fig. 1). The gap aspect ratio is defined as a ratio of gap's width to its length: W/L.

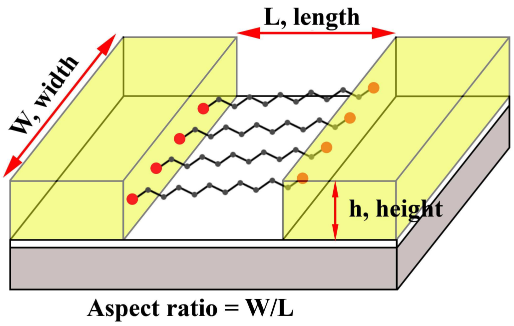

Figure 1 : Definition of geometrical parameters of the gap in lateral, planar configuration: length, L, width, W, and electrode thickness, h.

The figures without references to a paper: “[X]” or without words “adapted from [X]”, where X is a paper reference number, are either from my publications or are my sole creative work.

Chapter 1

Introduction and background literature

1.1 Nanogap fabrication. High-aspect ratio (HAR) nanogaps

Fabrication of nanogaps is an unavoidable part of electrical measurement at the nanoscale level, but at the same time it presents a significant challenge. Several techniques are known in the literature such as electromigration [22, 23, 24], electrodeposition [25, 26], mechanically controlled break junctions [27], electron beam lithography with some modifications (nanometer alignment with proximity effect correction [28], transmission electron beam utilization [29], over- [30] or underexposure [31] techniques, use of thin-film substrate to reduce electron back scattering [32]), on-wire lithography [33], etc. Interelectrode distances down to 1-2 nm may be achieved [24, 26, 29] by some of these methods, though without much control of the gap width. All the fabrication methods mentioned above have inherent limitations on the width of the electrodes. For example, electromigration is successful only for wires less than 100 nm wide [22, 23], and special conditions of e-beam lithography methods fail as well for extended gaps.

In some cases, though, both narrow (small L) and wide (large W) gaps, *i.e.* with high aspect ratio W/L, have a lot of advantages in electrical conduction measurements, such as:

- The total resistance of a channel with dimensions L, W and h (see fig. 1) is defined as $R = (\rho \times L)/(W \times h)$ where ρ is a resistivity $[\Omega \times m]$, a *characteristic* *parameter* of a material. Thus, keeping the length of the channel, L, and the thickness of the electrodes, h, at the constant values, an increase in electrode width, W, lowers the total resistance, which can be a key issue to investigate low-conductivity materials (semiconducting organic polymers, for example).

- Less influence of the surrounding on the object between electrodes (protection from the environment).
- Uniform electric field across the channel.

HAR nanogap fabrication has been demonstrated based on a selective etching of cleaved GaAs/AlGaAs heterostructures [34, 35]. However, this method comprises several steps, requires molecular-beam epitaxy (MBE) for substrate growth, and allows only restricted gap geometries. A much simpler HAR nanogap technique which potentially allows fabrication of HAR gaps was recently introduced by Prof. S. Wind group in Columbia University [36, 37]. The basic idea is the following: two separate lithographic patterning steps are used to define first and second electrodes, while the interelectrode separation is controlled by the oxidation of an Al sacrificial layer deposited upon the first electrode (fig. 1.1). The native aluminum oxide layer, Al_2O_3, overhangs the underlying metal and serves as a mask during the deposition of a second electrode. This layer must be removed afterward, but since Al_2O_3, corundum, is one of the most chemically inert materials [38], removal by direct chemical etching is very difficult. In a refinement, the authors deposited an additional sacrificial layer of SiO_2 underneath the Al layer and subsequently used etchant for SiO_2 to remove the SiO_2 and Al/Al_2O_3 layers [36]. The resulting gap sizes are as small as 2-5 nm, but the presence of the hardly removable Al_2O_3 layer and the use of SiO_2 etchant greatly limit the applicability of this approach in conjunction with conventional silicon electronics.

Although this method potentially allows fabrication of HAR nanogaps, the reported aspect ratios are less than 10 [36].

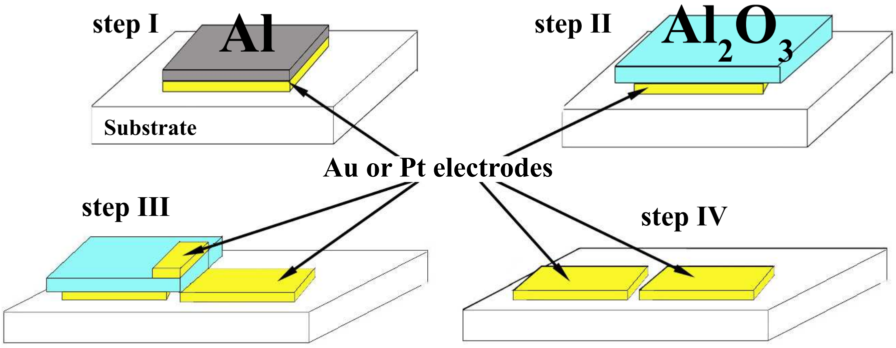

Figure 1.1 : Schematic of nanogap fabrication using oxidation of sacrificial Al layer.

1.2 Magnetite, Fe_3O_4, system.

1.2.1 Magnetite properties. Verwey transition.

Magnetite, Fe_3O_4, is known since ancient times, as a “lodestone” and was used to magnetize the mariner’s compass. It belongs to the family of strongly correlated materials (*i.e.*, with strong electron-electron interactions) and still attracts significant attention due to its interesting magnetic and electronic properties. Magnetite has a ferrimagnetic ordering, a classic example of the Néel two-sublattice model of ferrimagnetism, archetypical of the spinel ferrites. At temperature $T_N \sim 850$ K (Néel temperature) it undergoes a transition to a paramagnetic state. The anomalously high Néel temperature makes magnetite a good candidate for room temperature spintronic application.

In addition to magnetic behavior, it was discovered nearly 70 years ago that magnetite undergoes a first order phase transition at around 122 K accompanied both by a structural transition and by a drastic decrease in electrical conductivity: from "bad" metal ($10^3 < \sigma < 2.5 \times 10^4 Ohm^{-1} \times m^{-1}$) to insulator ($\sigma \sim 10\ Ohm^{-1} \times m^{-1}$) (fig. 1.2a). An anomaly in the temperature dependence of the heat capacity is also clearly detected (fig. 1.2b). This transition is called the Verwey transition (VT) after the name of the person who discovered it [39, 40] in 1939, and the temperature at which it occurs is the Verwey temperature, T_{V}. Similar metal-insulator transitions are known in a number of materials and are named as Verwey transitions as well [41, 42].

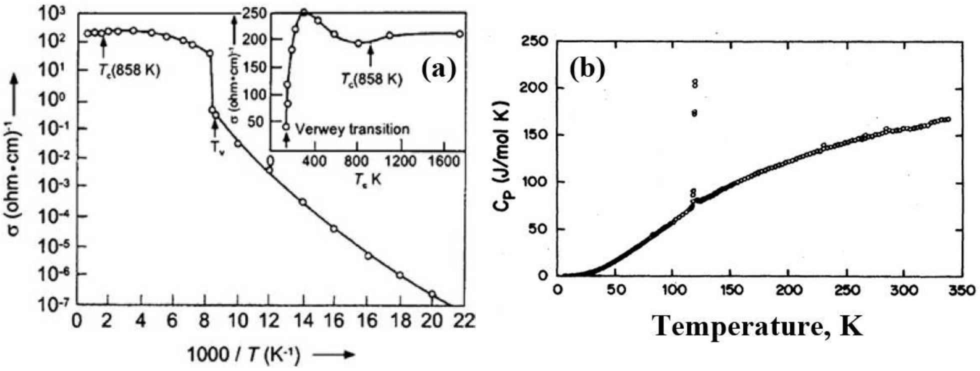

Figure 1.2 : (a) The temperature dependence of electrical conductivity in Fe_3O_4 [1] and (b) anomaly in temperature dependence of heat capacity at $T = T_V$ [2].

The mechanism and origin of this transition is still under hot debate. Originally, Verwey suggested a purely electronic mechanism of VT, *i.e.*, that high-temperature conduction ($T > T_V$) is due to continuous interchange of the electrons (thermally activated fast electron hopping) between Fe^{3+} and Fe^{2+} cations randomly distributed over the same crystallographic B-sites of spinel cubic structure (see sec. 1.2.2). The fact that other spinel ferrites, such as $CoFe_2O_4$, $NiFe_2O_4$ and $MnFe_2O_4$ with only Fe^{3+} cations in B-position are insulators strongly supports this explanation. A drastic decrease in conduction at T_{V} is caused by a long-range spatial ordering of Fe^{3+}

and Fe^{2+} cations upon cooling down below T_{V} and is accompanied by decrease in symmetry from cubic to tetragonal (as was originally suggested by Verwey). This charge ordering (CO) localizes electrons, effectively preventing the motion of carriers below T_{V}.

Since the very discovery of VT, magnetite is a subject of intense study. It was investigated by numerous (probably all possible) techniques [3, 43]. Many studies are very conflicting and full of controversy, with a common situation that different groups claim opposite results obtained by the same experimental technique.

The large discrepancies in experimental data might be caused by the fact that small amount of impurities or nonstoichiometry (deviation from ideal Fe_3O_4 stoichiometric composition) have a *detrimental* effect on Verwey transition [44, 45, 46]. Additionally, the presence of defects, structural deficiencies or inhomogeneities also lead to erroneous results. Along 70 years of study, the development of existing and emergence of new experimental techniques allow redefining previous measurements (many early experiments were proved to be erroneous) or making investigations at previously inaccessible levels.

1.2.2 Magnetite crystal structure. Charge ordering.

The main disagreement about VT can be formulated as following: one "community" believes that the origin of VT is a long range CO at T_{V}, and that the symmetry decrease and change in all macroscopic parameters such as resistivity, heat capacity, etc. are consequences of CO [3, 47, 48]. The second "community" thinks that VT is driven primarily by decrease in a lattice symmetry due to strong electron-phonon interaction, and that a weak CO is only a consequence of that symmetry change [43, 49, 50]. Of course, to resolve this problem the experimental data on low-temperature

$(T < T_V)$ structure, atom positions and charge distribution are need. This, however, appeared to be a problem: the argument about the occurrence, absence of CO or degree of charge disproportionation continues for nearly 70 years up to the present. Many groups around the world work on this problem, but the scientific community still did not achieve a consensus. Since the magnetite system is very complicated and many-sided scientists try to approach it from different directions. Fig. 1.3 illustrates the schematic representation of main investigation aspects along with experimental methods used.

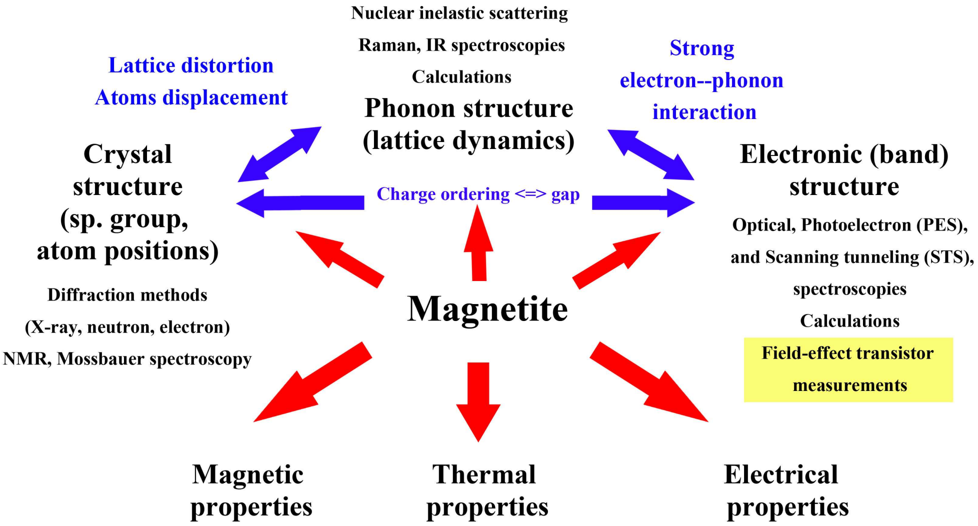

Figure 1.3 : Overview of various aspects of study in magnetite system. Top row represents microscopic properties, bottom row - selected macroscopic properties. The scheme depict the complexity of magnetite system, where both electron-electron and electron-lattice interaction are comparably important.

.

The first aspect is the “Crystal structure” (see fig. 1.3). Above T_{V}, magnetite has an inverse spinel structure AB_2O_4 (space group $Fd\bar{3}m, a = 8.3960\mathring{A}$, $Z = 8$). The oxygen anions form a cubic face-centered (fcc) lattice, and large interstices between

O^{2-} are partially occupied by iron cations. Tetrahedral A (8-fold) positions are occupied by Fe^{3+} cations, while octahedral B (16-fold) positions are equally occupied by Fe^{3+} and Fe^{2+} cations ($Fe^{3+}_{tetr}[Fe^{3+}Fe^{2+}]_{oct}O_4$) (fig. 1.4a). The spinel-like structure of magnetite remains unquestionable since the very early X-ray analysis while the symmetry of low-temperature ($T < T_V$) phase was argued over time.

Originally Verwey suggested a transition from cubic to tetrahedral symmetry [51, 40]). Later experiments showed it to be an orthorombic one [52, 53], and more recent studies proved low-temperature phase to have monoclinic symmetry [54, 55] (fig. 1.4b).

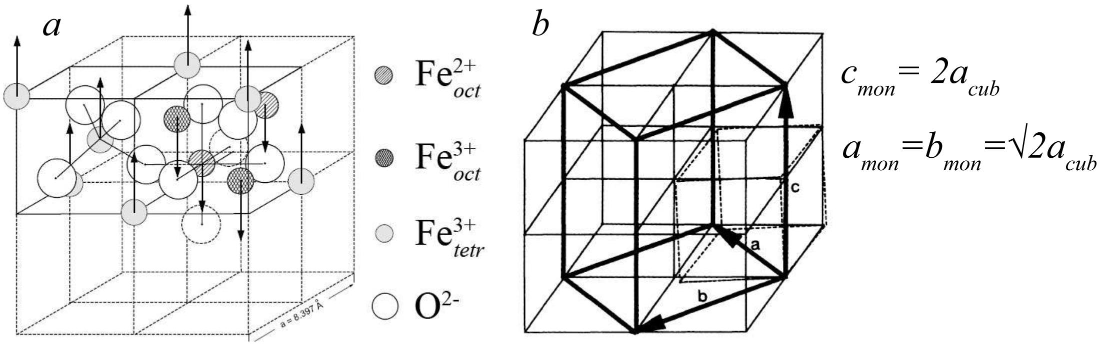

Figure 1.4 : (a) Simplified representation of high-T cubic structure of magnetite; inverse spinel $Fe^{3+}_{tetr}[Fe^{3+}Fe^{2+}]_{oct}O_4$. Only one octet is fully represented (adapted from [3]) (b) The relations between low-temperature monoclinic unit cell (double line) and the high-T cubic cell (dashed lines) of magnetite (adapted from [4]).

Only diffraction techniques (X-ray, neutron, electron) can probe *directly* the occurrence or absence of CO and determine the model of ordering. But for magnetite neither X-ray nor neutron diffractions can discriminate between two close valence states of the same atom, in this case, Fe^{3+} and Fe^{2+}. Electron diffraction study using atomic coordinates from [54] clearly disproved Verwey model of CO but was not able to define the exact charge distribution in the low-temperature phase [4]. The most recent diffraction experiments take advantage of the development of synchrotron radiation, and several groups performed X-ray resonant scattering experiments which theoretically are able to unambiguously distinguish Fe^{3+} and Fe^{2+} cations (due to noticeable difference in anomalous scattering factors f'' of Fe^{3+} and Fe^{2+} cations). Not surprisingly for magnetite, results from different groups again oppose each other: Garcia group claims the *absence* of CO based on X-ray resonant scattering at the Fe K edge [56]. At the same time other groups demonstrate the presence of fractional CO [47, 48] or total CO [57] by X-ray resonant scattering at the O K and Fe K edges.

Some other methods, such as Mössbauer spectroscopy and nuclear magnetic resonance, are also potentially able to distinguish Fe ions with different valence states and oxygen coordination. Although, as experiments demonstrated, the probing time of MS and NMR (10^{-8} sec) is not enough to resolve different valence states at octahedral B-sites in the magnetite structure at $T > T_V$ [58, 59, 60].

Summarizing “Crystal structure”(see fig. 1.3) data, one can say that most informative diffraction results proved original Verwey model of CO to be too simplified. The symmetry of low-temperature phase appeared to be monoclinic (not tetrahedral one as Verwey proposed) with doubling c-parameter and four-times increase in unit cell volume (fig. 1.4b). But, while the space group (Cc) and position of atoms are known, the *exact* charge distribution pattern, specifically, the location of 32 electrons in Fe^{2+}–Fe^{3+} octahedral positions, remains questionable and is still argued among the groups. The main reason is probably the very complicated monoclinic structure below T_{V} with 8 nonequivalent tetrahedral (A-site above T_{V}), 16 nonequivalent octahedral (B-site) positions and total 96 iron and 128 oxygen atoms in the unit cell.

1.2.3 Phonon and electronic structures.

Meanwhile, the "Phonon structure" (*i.e.*, lattice dynamics) (fig. 1.3) was probed by Raman and IR spectroscopies and nuclear inelastic scattering (NIS). The important role of the electron-phonon interaction was first emphasized by Iizumi, who proposed that the atomic displacements (and thus lattice distortion) at the T_{V} *result* from the condensation of phonons (neutron diffraction study [54]). Later, IR and Raman spectroscopies showed that phonon modes stiffen in the low-temperature phase, despite the lattice expanding below T_{V} [61]. And more recent NIS of synchrotron radiation showed a pronounced drop in vibrational densities of states in the vicinity of the Verwey transition and proved lattice stiffening below T_{V} [62]. Thus, experimental evidences were found for *lattice* participation in the mechanism of VT. That means VT is caused by a *combination* of strong local Coulomb interactions between 3d electrons (electronic component) and the electron-phonon coupling with the resulting decrease in total energy gained by symmetry lowering at T_{V} [63, 50].

The other aspect of magnetite internal microstructure is the "Electronic structure" (fig. 1.3). Electronic structure here relates to the energy distribution and nature of the electronic states. With the inability to get the distribution of charge within the init cell, the elucidation of electronic structure is very important. Experimental probing can be implemented by two main groups of methods: first, electron (scanning tunneling (STS), photoemission (PES)) and optical spectroscopies, and second, field effect transistor (FET) measurements.

Fig. 1.5 shows main aspects of magnetite electronic structure. The majority spin-down band and minority spin-up band are split by an exchange energy Δ_{ex}. The five degenerate *d*-electron levels of Fe ions are further split by the crystal field, Δ_{cf}, into three degenerate t_{2g} and two degenerate e_g levels. For both Fe^{2+} and Fe^{3+}

ions five electrons occupy the majority t_{2g} and e_g levels. The extra electron of the Fe^{2+} ion (depicted as red arrow pointed down) (fig. 1.5a) occupies the minority t_{2g} band, which is the only band located at E_f, giving rise to half-metallic behavior of magnetite [*i.e.*, its electronic density of states is spin polarized at the Fermi level, and the conductivity is dominated by these spin-polarized charge carriers (fig. 1.5a)]. The high room temperature conductivity of magnetite is attributed to the hopping of this electron between B-octahedral sites which dominate the DOS around E_f. Following the original Verwey model, charge ordering below T_V should open a gap at the Fermi energy in the magnetite band structure, *i.e.*, metal-insulator transition occurs (fig. 1.5b).

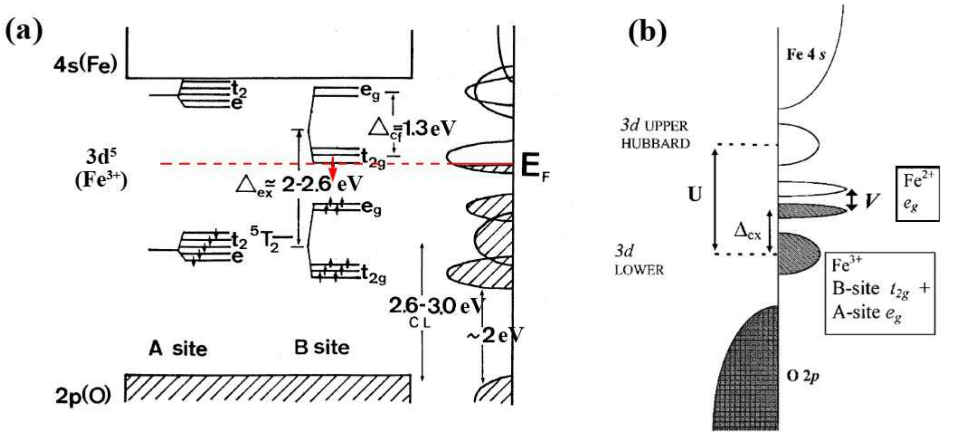

Figure 1.5 : Schematic representation of the (a) energy band-structure at $T > T_V$ in the assumption of the metallic state (adapted from [5]) (b) opening of the gap below T_V [6].

Experimental data on Fe$_3$O$_4$ electronic structure are again controversial (in the sense of having gapless excitation at the Fermi level): there is an argument about whether at $T > T_V$ magnetite is a metal [64, 65] (as Verwey implied) or a semiconductor with a small ($\sim$7meV) band gap [66, 67, 68] (fig. 1.5). PES and STS measurements made are not conclusive [64, 66, 65]. Besides, the latter methods characterize only the *surface*, while the bulk might behave in an entirely different manner.

An alternative method to probe band structure is through *field effect transistor* (FET) measurements. The same as STS, this is an electrical method (*i.e.*, in contrast to other spectroscopy methods which involve interaction of material with the radiation, *i.e.*, photons, STS and FET are electrical probing method (measuring I-V curves), *i.e.*, interaction with incoming electrons, not photons, takes place).

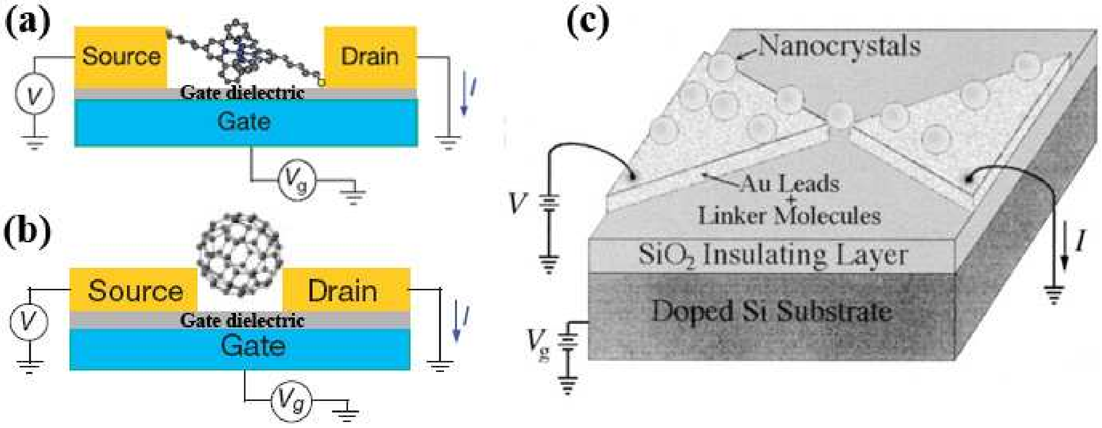

Figure 1.6 : Schematic respesentation of field effect transistors to investigate electrical properties of (a) organic molecule [7] (b) fullerene [8] (c) nanoparticle of CdSe (quantum dot) [9].

FET is a three terminal device and principle of operation can be briefly described as following: The voltage is applied to source and drain electrodes (V_{SD}). The third, so called gate electrode, is isolated from the source, drain electrodes and an object of study by some dielectric layer, called gate dielectric. By applying voltage to the gate electrode (V_G) one can tune the electronic structure of an investigated object. The schematic representation is shown in fig. 1.6. One measures source-drain current, I_{SD}, as a function of source-drain voltage, V_{SD}, ($I_{SD} - V_{SD}$ curves) at some constant gate voltage, V_G. $I - V$ curves then are recalculated to differential conductance - dI/dV vs V_{SD} - curves, which effectively reflect the density of states of an investigated material.

Thus, one can examine an electronic structure as different gate voltages (sign, values) are applied. Generally, heavily doped Si wafer with SiO_2 layer can function as FET with Si layer as a bottom gate electrode and SiO_2 layer as a gate dielectric (fig. 1.6c). FET measurements were successfully used to investigate electronic structure of organic molecules [69], fullerenes [8] and quantized energy levels of quantum dots [9] (fig. 1.6).

No FET measurements on magnetite system are reported yet . Given clear lack of agreement and understanding of Verwey transition based on numerous experiments (fig. 1.3) summarized above, such a new method might be of a great help.

1.2.4 Electrically driven phase transition in magnetite.

We started to study magnetite nanoparticles in our lab in the belief that electrical measurements at the nanoscale level in FET configuration can help in defining the band structure of magnetite, thus contributing to the resolution of a long-standing problem of VT mechanism. The starting material was Fe_3O_4 nanoparticles (10-20 nm in diameter) coated with oleic acid synthesized by our collaborators in Prof. V. Colvin's group (Rice University) [70]. The first measurements were made by Sungbae Lee (November, 2006) testing magnetite nanoparticles in a simple two-terminal (not yet FET) configuration (two electrodes defined by two-step electron beam lithography with a minimum gap size of ≈20-40 nm) on the surface of Si/SiO_2 wafers (fig. 1.7a).

Unexpected and surprising phenomenon was observed: *I*-*V* curves at low temperatures showed a transition from the insulating state to a state with much lower resistance upon application of a sufficiently high voltage (fig. 1.7c). The transition is hysteretic in voltage and symmetric for both positive and negative voltages. The main characteristic of this transition is the switching voltage, V_{SW}. V_{SW} is temperature dependent, and decreases as temperature increases (fig. 1.7c). But above a certain temperature this transition is not observable. The threshold temperature is ≈110-120 K, close to the Verwey temperature, suggesting that the voltage-driven transition happens only if Fe_3O_4 is in insulating state at a measurement temperature in an undisturbed state (without voltage application).

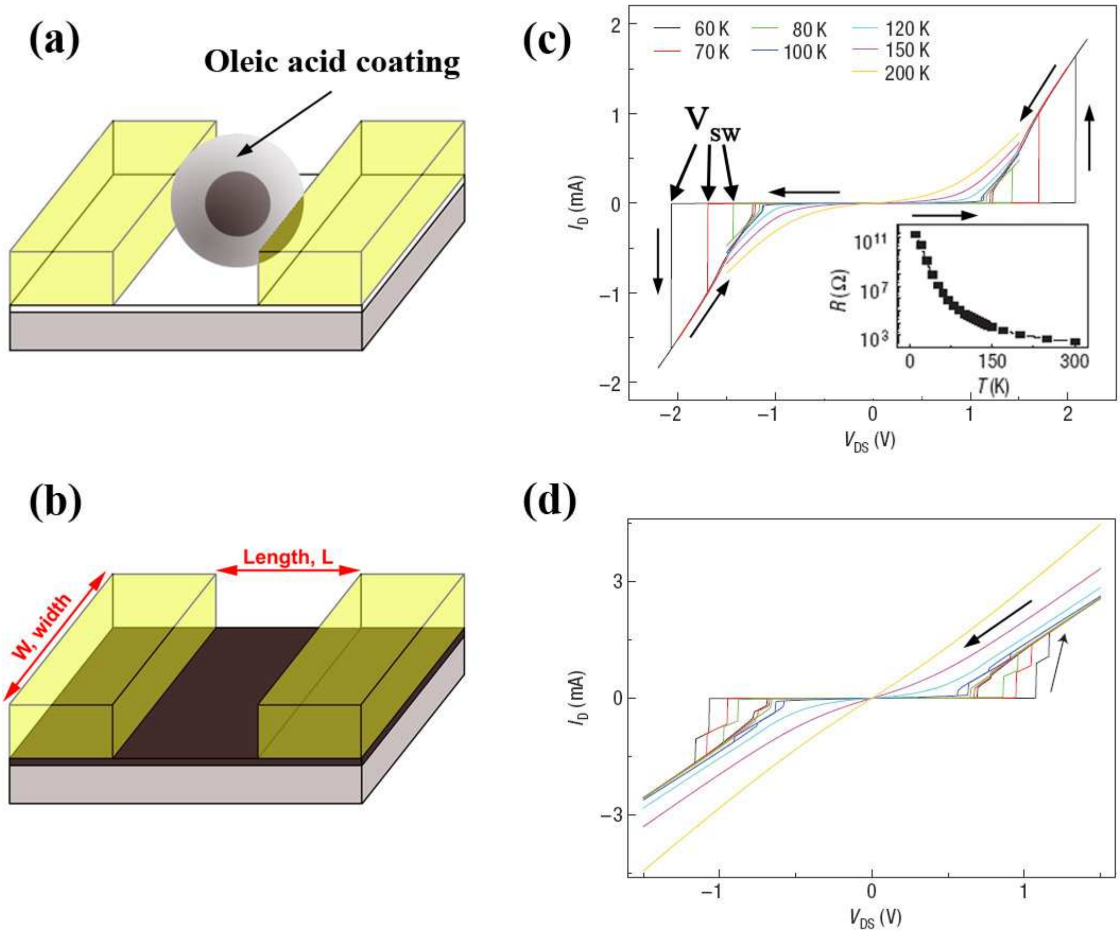

Figure 1.7 : Schematic representations of two-terminal device to examine (a) Fe_3O_4 nanoparticles and (b) Fe_3O_4 thin films; Current-voltage characteristics at different temperatures (c) for a device based on 10 nm NP(s) and (d) for a device produced on 50 nm-thick magnetite film. Arrows indicate the direction of voltage sweeping and the positions of switching-on voltages are shown. Inset to (c) shows temperature dependence of two-terminal zero-bias resistance. ((c) and (d) are adapted from [10]).

In addition to devices incorporating Fe_3O_4 nanoparticles, devices on the surface of thin Fe_3O_4 films (40-60 nm) (fig. 1.7b) were tested. They show characteristics quantitatively similar to nanoparticle (NP) devices in switching properties and trends with temperature (fig. 1.7d). Some devices (both NP- and film-based) show multiple switchings (fig. 1.7d), assigned, most probably to the switching of different structural domains in thin films and to switching of several nanoparticles in the gap.

The first suggestion by considering these jumps in current (*i.e.*, in resistance) might be that it is caused by local heating of the sample above T_{V} at a transition point. Such transitions, indeed driven by Joule heating of the samples above T_{V} under bias, were previously observed in bulk magnetite [71, 72]. But there are several experiments that disprove the hypothesis of a thermally driven transition and support an electric-field driven one.

(1) Thermally driven switching would correspond to raising the local temperature above T_{V}. The local steady-state temperature is determined by the power dissipated ($I \times V$) and the thermal path. The thermal conductivity, κ, of magnetite increases as T is decreased through and below T_{V} [73]. Thus, the material's thermal coupling (path) to the cryostat improves as T is reduced. At a fixed cryostat temperature, an improved thermal path would imply that more power dissipation would be required for a given local temperature rise. Therefore, assuming heating effect, the power at a transition point ($I \times V$) should be higher as the temperature gets lower to provide enough heat to warm up above T_{V}. But this is an opposite to what is observed experimentally: the lower the measurement temperature, the less power is dissipated at a transition point (fig. 1.8a). Furthermore, the power dissipated at a switching point does not approach zero as $\mathrm{T} \rightarrow T_{\mathrm{V}}$, again inconsistent with thermally driven switching [10].

(2) At a given T the power dissipated at the switching back point, V_{SW}(back), (point 2 in fig. 1.8b) significantly exceeds the one dissipated at the switching on point, V_{SW}(on), (point 1 in fig. 1.8b), inconsistent with thermal switching expectations [10].

(3) The shape of hysteresis and the position of switching on and back voltages remain unchanged in the experiments on varying sweep rates over two orders of magnitude (from 0.7 V/s up 70 V/s) (fig. 1.8a inset) [10].

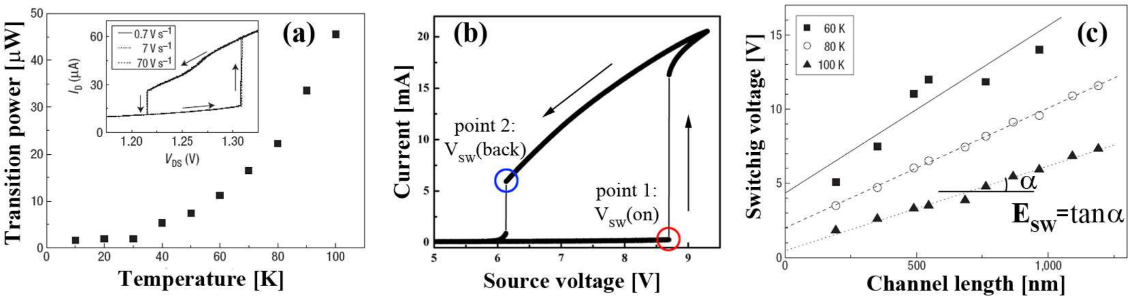

Figure 1.8 : (a) Power required to switch from the insulating into the less resistive state as a function of temperature, for a device based on ≈20 nm diameter Fe_3O_4 NPs. Inset shows hysteresis loop in the current of the same device at 80 K, showing essentially no change in switching characteristics as the voltage sweep rate is varied over two orders of magnitude [10]. (b) A fragment of I-V curve demonstrating switching on point, V_{SW}(on) (point 1), and switching back point, V_{SW}(back) (point 2). (c) Switching voltages as a function of channel length at several temperatures. The slope of $V_{SW}(L)$ trend line at each temperature gives a characteristic electric field required for switching (adapted from [10]).

The observed new transition in magnetite seems to be driven by electric field. Pattening on the surface of magnetite films allows fabrication of devices with different channel lengths, Ls, *i.e.*, the distance between two electrodes on the film surface (see fig. 1.7b). Plotting of V_{SW} as a function of L gives a straight line. Linear $V_{SW}(L)$ dependence strongly implies that at each temperature there is a specific *electric field*, $E_{sw} = V/L$, (not an absolute voltage) value to drive a transition (fig. 1.8c).

It is also worth mentioning that in two-terminal experiments the contact resistance, R_C, makes a dominant contribution to the total resistance. For pure Au electrodes R_C comprises more than 90% of the total resistance. The temperature dependence (fig. 1.7c, inset) of the zero-bias resistance, R(T), has no step at $T_{\rm V}$, showing that R(T) remains dominated by contact effects. Beside, the non-zero intercepts of the $\mathrm{V}_{SW}(L)$ trend lines (fig. 1.8c) indicate that some device-dependent threshold voltage must be exceeded for switching even when $L = 0$, suggestive of contact effects.

FET measurements using the doped-Si substrate as a bottom gate electrode and SiO_2 as a gate dielectric showed no discernible gate modulation in NP devices for gate biases between −80 V and +80 V. FET measurements of film-based devices in a bottom gate configuration are not possible, due to the very thick (≈0.5 mm) insulating MgO substrate. Other gating options should be explored for FET measurements of film-based devices.

One of the alternative gating configurations to use with film-based devices is the one with a *top* gate electrode. Instead of conventional SiO_2 layer as a gate dielectric one can use solid polymer-electrolyte layer. The latter was recently successfully used to gate organic FETs [74, 11]. Polymer-electrolyte (PE) solution consists of a polyethylene oxide (PEO) in acetonitrile with a dissolved Li^+ salt. Prepared solution is drop-casted or spin coated on a wafer with predefined electrodes. After solvent evaporation a solid thin layer is formed which has very high capacitance: $\sim 10\mu\mathrm{F}/cm^2$ compare with $\sim 10\mathrm{nF}/cm^2$ for conventional SiO_2 layer [11]. Large capacitance is achieved due to the presence of mobile ions (Li^+ cations and anions) which are separated under application of gate voltage creating strong electric field within PE layer and double charge layer on the surface of an investigated object (fig. 1.9a). The device operational mechanism was proved to be truly electrostatic (field-) effect, not chemical or electrochemical doping [11]. Schematic representation of polymer-electrolyte "gate effect" is shown in fig. 1.9 along with the possible FET configuration on the surface of magnetite thin films.

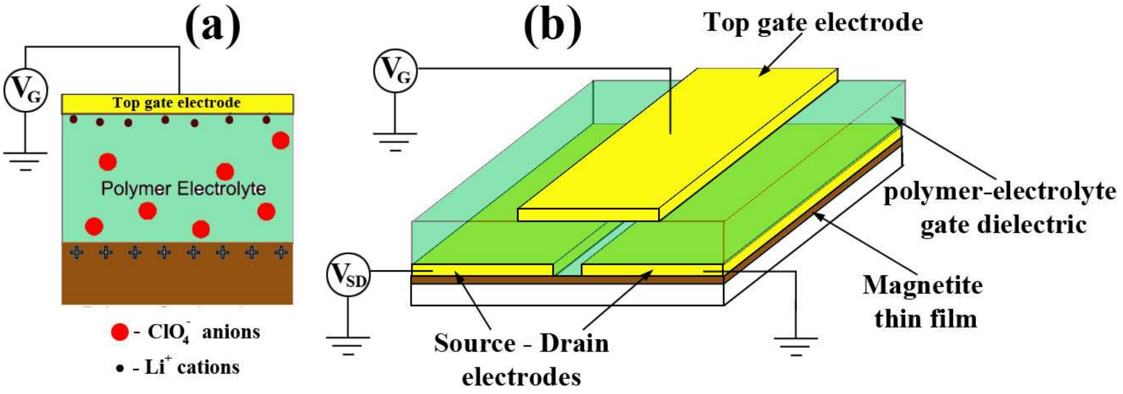

Figure 1.9 : Schematic representation of (a) Field-effect in polymer-electrolyte gated FET. The distribution on cations and anions is shown for negative gate voltage, V_G, applied (adapted from [11]) and (b) (not to scale) possible FET device with source and drain electrodes separated by HAR nanogap, top gate electrode is deposited on top of polymer-electrolyte layer across the gap.

1.3 Introduction to resistive switching systems

By definition, resistive switching (RS) is a phenomenon of a dramatic change of the material's resistance driven by the application of voltage, current, or an electric field [12, 75]. The system can be reversibly switched between high-resistance (or insulating) Off state and low-resistance On state. RS systems attracted both researcher's and engineer's attention, since switching from On state to Off state has a potential application in next-generation memories [76, 77], so called resistance random access memory (ReRAM).

The ReRAM memory cell has either a capacitor-like structure composed of insulating or semiconducting materials sandwiched between two metal electrodes (fig. 1.10a [12]) or a lateral, planar configuration with two metal electrodes placed on the surface of RS material (fig. 1.10b [78]). The variety of materials, both organic compounds [79, 80, 81] and transition metal oxides, have been reported to exhibit RS phenomenon. Among oxide RS systems are widely-studied colossal resistance manganites [82], perovskites (*e.g.* $SrTiO_3$ [83]), 1D cuprates Sr_2CuO_3 [84], NiO [85], TiO_2 [78] *etc.*

1.3.1 Classification

The numerous RS systems can be classified according to either (1) the shape of I-V characteristics and voltage polarity, (2) type of conducting path or (3) the switching mechanism.

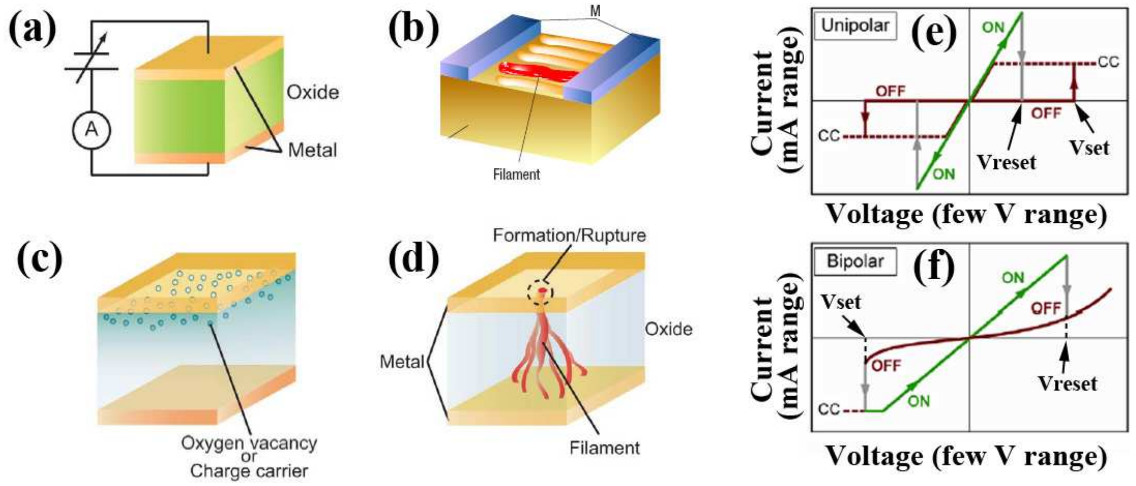

Figure 1.10 : (a) Schematics of a ReRAM memory cell with a capacitor-like structure in which an insulating or semiconducting oxide is sandwiched between two metal electrodes [12].(b) Lateral, planar configuration of RS system. The red tube indicates the filament responsible for the On state [13]. Classification of RS systems according to either (c) interface-type conducting path or (d) filamentary conducting path [12]. Unipolar (e) and bipolar (f) switching schemes, CC denotes the compliance current, often needed to limit the current in On state (adapted from [13] with modifications).

(1) On the basis of I-V characteristics, the switching behavior can be classified into two types: unipolar (or symmetric) and bipolar (or antisymmetric). In unipolar

resistive switching, the switching direction depends on the amplitude of the applied voltage but not on the voltage polarity (fig. 1.10e). An as-prepared (pristine) memory cell is originally in Off-state and first undergoes one-time "forming process", which is an application of high voltage for a certain amount of time (typically, from several seconds to several minutes), which results in a soft breakdown of the material and drives the system to the low-resistance state, On state. After the forming process, the cell in the On-state is switched to the Off-state by applying a threshold voltage ("reset process"). Switching from the Off-state to the On-state ("set process") is achieved by applying a threshold voltage that is larger than the reset voltage (fig. 1.10e [12]). In the set process, the current is limited by the current compliance of the control system or, more practically, by adding a series resistor . Bipolar resistive switching shows directional resistive switching depending on the polarity of the applied voltage (fig. 1.10f). The set to an On-state occurs at one voltage polarity and the reset to the Off-state on reversed voltage polarity.

(2) According to the type of conducting path RS systems can be categorized as having filamentary conducting or interface-type path. In the former case RS originates from the formation and rupture of conductive filaments in an insulating matrix (fig. 1.10b, d). First, in the forming process, filamentary conducting paths form as a soft breakdown in the dielectric material. Rupture of the filaments takes place during the reset process, and filament formation during the set process. In interface-type path RS takes place at the interface between the metal electrode and the oxide (fig. 1.10c).

(3) Conceivable switching mechanisms of RS are summarized in fig. 1.11. They often consist of a combination of physical and/or chemical effects. As a first approach, RS mechanisms can be classified according to whether the dominant contribution

comes from a thermal effect, an electronic effect, or an ionic effect [75].

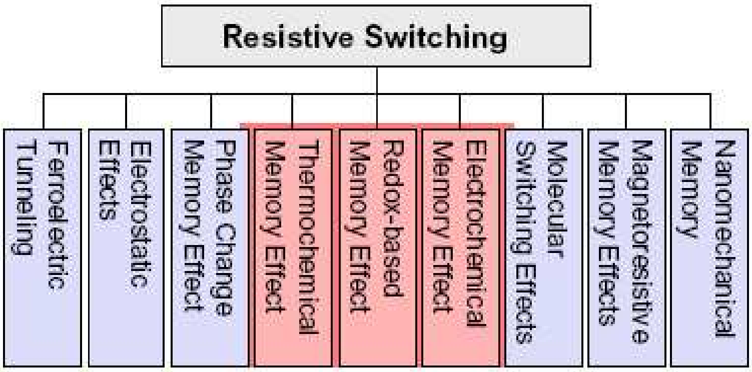

Figure 1.11 : Classification of resistive switching mechanisms. [13]

1.3.2 Resistive switching in magnetite

Hysteretic current jumps in current discovered in *I-V* curves in magnetite, described in sec. 1.2.4, can be classified as resistive switching (RS), since there is a transition from a high-resistance state below V_{SW} to a low-resistance state above it (fig. 1.7c) driven by high bias. Since voltage-driven transition in Fe_3O_4 was just discovered and there is a lack of direct analogy in literature, considering it as a RS is a good starting point.

On the other hand, attribution of RS in Fe_3O_4 to one of the existing classes is not straightforward, since transition characteristics bear significant differences from other RS systems discussed above (see sec. 1.3.1). Namely,

1. No one-time forming process is needed in order to start observing RS in magnetite system.

2. Bipolar/unipolar classification cannot be applied, since the shape of hysteresis in Fe_3O_4 system (fig. 1.7c, d) differs from the one for bipolar or unipolar

switchings (compare with fig. 1.10e, f). The main difference is that the On state in magnetite does not persist down to V=0 V, but rather is effective only in a limited voltage range [V_{SW}(back) - V_{SW}(on)] (see fig. 1.8b for definitions of V_{SW}(on) and V_{SW}(back)), where $|V_{SW}(\text{back})|$ is greater than zero.

3. Following the discussion in the previous item one can conclude that in Fe_3O_4 system there is essentially no memory effect. The On state does not exist without high voltage application, $V > V_{SW}$. Independent of the previous history of a voltage sweeping or applied voltage amplitude, application of *any* voltage pulse $V < V_{SW}$ to address ("read") the state of the system results in the Off state.

4. There is a lack of data on a type of conduction path and a switching mechanism.

This "special" place of Fe_3O_4 in the frame of RS systems makes it even more intriguing to investigate. One of the main objectives of the research in this thesis is to find out the mechanism of EFD transition in magnetite.

1.4 Thesis organization

In this thesis we mainly investigate the electric-field driven (EFD) transition in Fe_3O_4, just recently discovered in our laboratory [10] (sec. 1.2.4). Our main goal is to understand the origin of the observed transition and its mechanism. The magnetite in a form of high-quality epitaxial thin films [not nanoparticles (NPs)] is used in the present work due to the better scalability of film-based devices and better control of film stoichiometry, giving less device to device variation. Besides, coating of synthesized NPs with insulating layer of oleic acid gives rise to an increase of a total device resistance, resulting in a very low percentage of NP devices that display switching.

Magnetite (100) films with a 30-120 nm thickness were grown on ⟨100⟩ MgO single crystal substrates by oxygen-plasma-assisted molecular beam epitaxy by our collaborators at Trinity college, Dublin, Ireland (Dr. S. Sofin and Prof. I. Shvets) [86, 87]. To prove crystalline quality and stoichiometry of the samples all Fe_3O_4 films were characterized by reflection high-energy electron diffraction (*in situ*, during growing), high resolution X-ray diffraction measurements, Raman spectroscopy and resistance measurements [88, 89]. After "quality control" tests the films were shipped to our laboratory with some precautions taken to avoid possible oxidation of sensitive Fe_3O_4 films in air.

Most of the electrical measurements in this thesis were performed by applying voltage, measuring current, and then plotting and analyzing I-V curves. Further in thesis "I-V curves" or "I-V characteristics" imply this sort of measurements, unless otherwise specified. Zero bias resistance is defined as an inverted slope of I-V curve in the vicinity of zero volts (typically 0 - 100 mV voltage range), where I-V dependence is linear.

The thesis consists of one introductory (Chapter 1) and four experimental chapters with the results and analysis of the data. In Chapter 2 we first develop a new technique to produce high-aspect ratio (HAR) nanogaps. We apply it to fabricate magnetite devices with HAR gaps in the following chapters to investigate EFD transition in Fe_3O_4.

In Chapter 3 we find out the origin of hysteresis in I-V curves in Fe_3O_4. We apply voltage in a pulsed regime and demonstrate that, while the transition itself is electrically driven, the hysteresis originates from Joule heating of the sample once it is switched to the low-resistance On state. A simple relaxation-time thermal model is proposed that captures the essentials of the hysteresis mechanism.

In Chapter 4 we make four-terminal measurements which quantitatively separate the contributions of each electrode interface and the magnetite channel. We trace the changes of device (magnetite) and contact resistances and demonstrate that on the onset of the EFD transition contact resistances at *both* source and drain electrodes and the resistance of magnetite channel decreases abruptly. We further extend four-terminal measurements by doing experiments with *various* contact metals (with different work functions). This allows us to get better insight into the Me/Fe_3O_4 interface properties. This data allow us to make a suggestion about switching mechanism in Fe_3O_4 system.

In Chapter 5 we perform V_{sw} distribution measurements and trace the dependence of V_{SW} width on temperature. Besides, we address the influence of magnetic field (perpendicular to the surface of Fe_3O_4 films) on the EFD transition.

Finally, we propose a possible picture of mechanism of the EFD transition in Fe_3O_4 based on the experimental data collected in this thesis and give some directions for further continuation of this work.

Chapter 2

Development of the technique to produce high-aspect ratio (HAR) nanogaps

2.1 Starting point

As discussed in sec. 1.1, fabricating two electrodes separated by a nanometer gap running parallel over a macroscopic width (*i.e.* high-aspect-ratio (HAR) nanogaps) is a significant challenge. A couple of existing techniques have severe limitations and a new fabrication method is of high demand.

In this chapter we develop a simple, reproducible technique for HAR fabrication which allows the production of 10-20 nm gaps with aspect ratio up to 1000. The starting point was the publication of Prof. Wind's group in 2006 [36, 37] (sec. 1.1). In one of their fabrication steps the wafer is placed into SiO_2 etchant. But, as it is well known, Si wafers coated with thermal SiO_2 oxide are most commonly used both in research laboratories (including ours) and in industrial conventional Si-based electronics. Thus, direct reproducibility of this technique in most environments is impossible, since placing the Si/SiO_2 wafer into SiO_2 etchant will result in a complete removal of the structure, patterned on top of SiO_2 layer. In addition, this method potentially has no limitations on the gap width and thus allows fabrication of HAR nanogaps. However, authors of this work [36] demonstrated the gaps with aspect ratios less than 10 (W=20-40 nm). Thus, for the best benefits, we modify this technique to eliminate SiO_2 etching step and to produce HAR nanogaps.

First, we tried to deposit Al without underlying SiO_2 layer and then etch formed

Al_2O_3 (alumina) directly (see fig. 1.1). Alumina is one of the most chemically inert materials [38] and thus the etchant options are quite limited. We chose a mixture of 6 wt. % of H_3PO_4 and 2 wt. % of H_2CrO_4 in H_2O known in literature to remove anodized aluminum oxide films [90, 91]. The numerous attempts to find proper etching parameters to etch away Al_2O_3 were unsuccessful: we tried different etching temperatures (from room temperature up to the boiling point (~100° C)), duration (1-20 min), simple stirring and ultrasonication. As fig. 2.1 illustrates, despite the gap was clearly formed, some residuals of alumina with second-step gold were always present on the first-step Au electrode surface (fig. 2.1a). Further etching lead to damaging of gold electrodes themselves (fig. 2.1b).

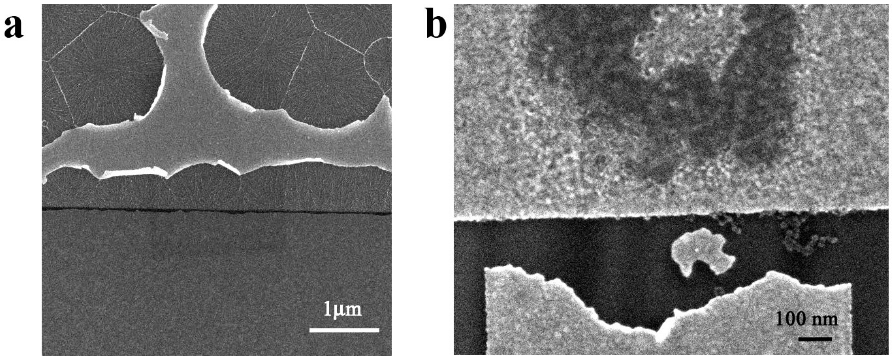

Figure 2.1 : Unsuccessful attempts to etch Al_2O_3 directly. (a) Gap is formed, but there are residuals of alumina with second-step Au layer on top; (b) Further etching to remove alumina residuals results in damaging of Au electrodes and significant widening of the gap.

Then, since direct alumina etching was proved to be impossible, we started to explore options of using other metals. Chromium, like aluminum, forms a native oxide at ambient conditions, but Cr oxide is much easier to etch away. Thus, we replaced Al/SiO_2 sacrificial layers by single Cr layer and adjusted lithography and etching parameters as discussed in detail (step by step) below.

2.2 Fabrication steps.

The electrode fabrication process consists of three main steps outlined in Fig. 2.2: two step electron beam lithography and etching. Starting substrates were silicon wafers with 200 nm thermally grown SiO_2 layer. Poly-(methylmethacrylate) (2% in chlorobenzene) was spin-coated at 3000 rpm on the wafers to form a 500 nm resist layer, followed by baking at 180°C for 2 min. Conventional electron beam lithography (JEOL 6500, 30kV) was used to define the first electrode without any special conditions or unusual regimes. The typical pad size used here is 100×100 μm^2 and the width and the length of the lead are 10-20 μm and 200 μm, respectively. After e-beam exposure the pattern was developed in a 1:3 volume mixture of methyl-isobutyl-ketone (MIBK) and isopropanol (IPA) at room temperature (RT). Metallization via electron beam evaporation of 1 nm Ti (adhesion layer), 15 nm Au and 10-45 nm Cr layers followed, with subsequent lift-off in acetone to complete the fabrication of first electrode (Fig. 2.2a).

Oxidation of Cr layer in ambient conditions results in a native oxide layer (Cr_xO_y). The oxygen incorporation into the original Cr lattice leads to expansion of the chromium layer both laterally and vertically (Fig. 2.2b). The second electrode is then fabricated by the same e-beam lithography process described above with only rough micrometer alignment of the second electrode relative to the first one. During the second-step deposition of 1 nm Ti (0.1 nm/sec) and 15 nm Au (0.2 nm/sec) layers, Cr_xO_y oxide expanded on top of the underlying Ti/Au layer protects an few-nm-wide area around first Ti/Au electrode from bridging with the second-step Ti/Au layer (Fig. 2.2c). As soon as the crossing of the first- and second-step leads is achieved the gap formation is assured. Misalignment of the second electrode does not have any impact on the size of the gap and displacement in direction perpendicular to the first lead (fig. 2.2c) does

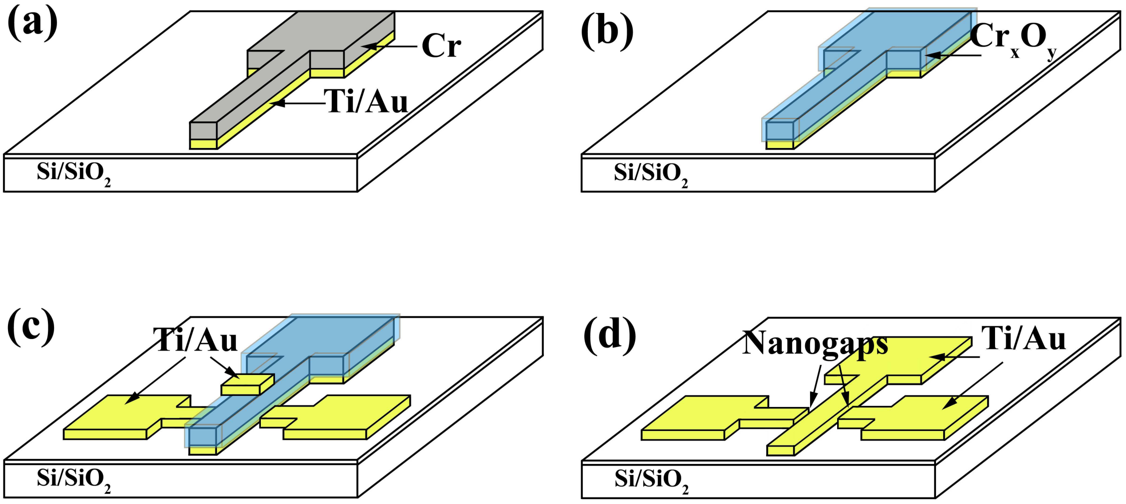

Figure 2.2 : Schematic of the fabrication process (not to scale) (a) First electrode fabrication and deposition 1 nm Ti, 15 nm Au and 25 nm Cr layers. (b) Oxidation of Cr layer in ambient conditions giving an oxide layer a few nm thick (c) Second electrode patterning and deposition, with chromium oxide acting as a mask. (d) Etching away Cr/Cr$_x$O$_y$ and overlying second-step Ti and Au layers.

not even influence the gap location (position). The suggested “double pad” geometry of the second-step electrode (Fig. 2.2c) simultaneously produces two addressable gaps in one step.

Finally, the wafer was placed into chromium etchant solution (CR-7, Cyantek Co.) at room temperature for 90 sec. to remove the Cr/Cr$_x$O$_y$ layer and overlying second-step Ti and Au layers on top of the first-step electrode. As a result two pairs of electrodes separated by nanogaps with separations defined by the thickness of Cr$_x$O$_y$ layer are produced (Fig. 2.2d). For fixed Cr thickness, the aspect ratio of the gap is set by the width of the second-step lead and can be varied over a large micron-sized range. Fig. 2.3a shows representative scanning electron micrographs of the produced electrodes on Si/SiO$_2$ wafer, with the gap separation of 10-20 nm and the gap width of 20 μm. The aspect ratio, thus, exceeds 1000.

The overall yield of the process (unshorted devices) is limited by the etching yield,

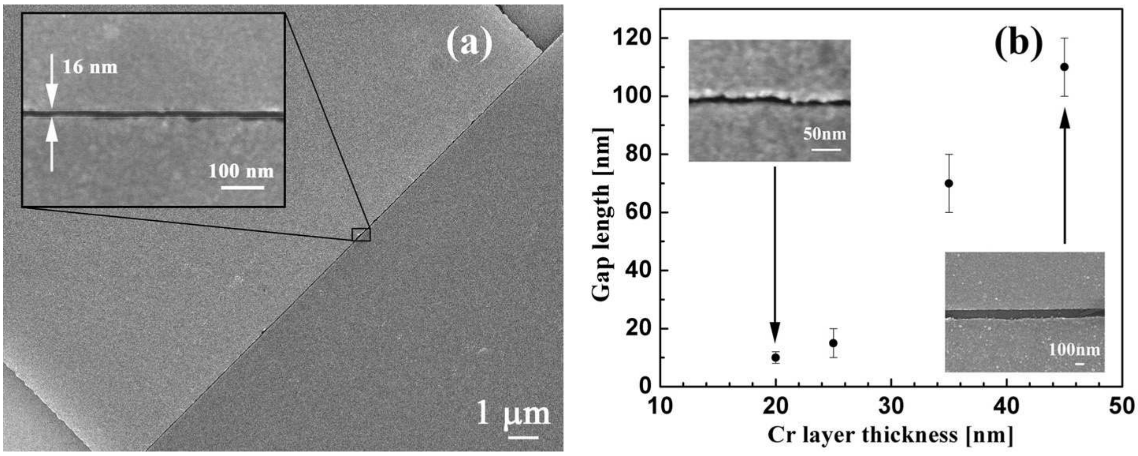

Figure 2.3 : (a) Scanning electron microscopy image of two gold electrodes on Si/SiO_2 wafer separated by 10-20 nm gap running along 20 μm (rotated by 45 deg.). The inset shows high magnification SEM image of a small fraction of the nanogap. (b) Dependence of the gap size on the thickness of deposited Cr layer. Each point represents an average over 16 devices fabricated under the same conditions. Insets show SEM images of produced gaps for 20 nm- (top) and 45 nm-thick (bottom) Cr layer.

and approaches nearly 100% when Cr layer thickness is optimized. Furthermore, the selectivity of the etchant is excellent, making this process suitable for a wide variety of substrates and metallizations. In addition to Ti/Au metallization, our technique was successfully applied to fabricate Pt, Al, Fe and pure Ti electrodes on Si/SiO_2 wafers.

It should be noted that another advantage of our method is the relatively mild requirement for the quality of the lithography and deposition (since neither gap size nor the uniformity of the gap depend on it). As a result, similar nanogaps can be produced by using conventional photolithography instead of much more time-consuming and less accessible electron beam lithography. The fabrication steps are the same as the ones outlined above, with the replacement of PMMA with positive photoresist (S1813) and using a standard MF-319 developer. Nanogaps as narrow as ~10 nm were produced on Si/SiO_2 wafers by using photolithography (fig. 2.4).

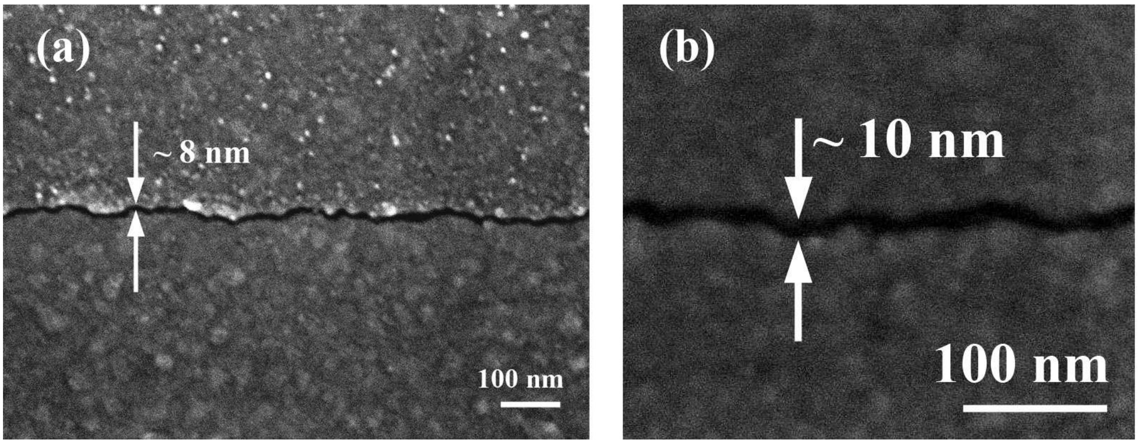

Figure 2.4 : Two examples ~10 nm gaps produced with Cr HAR method using conventional photolithography to define electrodes.

2.3 Gap size control. Cr layer thickness.

The resultant gap size of 10-20 nm is much larger than the expected thickness of native amorphous Cr_xO_y formed at ambient conditions (~2 nm [92]). To explore this issue we made a set of fabrication experiments with deposition of different Cr layer thicknesses. As fig. 2.3b shows, increasing the thickness of Cr layer leads to wider gaps. The latter is also inconsistent with the formation of only native oxide, since in this case the gap size should have been independent of Cr layer thickness.

To explain why the gap size is larger than the thickness of native oxide layer (2 nm), two factors may be considered.

The first factor is partial thermal oxidation of the Cr layer. The maximum temperature our sample experiences during the fabrication process is 180°C (PMMA baking for second step lithography) and this step lasts for only 2 minutes. According to literature data, Cr starts to extensively form thermal oxide at temperatures above 300 °C [93]. Based on this we believe it is unlikely that the *whole* layer is oxidized. Besides, we made estimates based on the crystal structure of Cr and Cr_2O_3 oxides

Table 2.1 : The expansion Δx of Cr layer in the assumption all Cr is oxidized

Cr layer thickness	20 nm Cr	25 nm Cr	35 nm Cr	45 nm Cr
Δx	19 nm	23 nm	37 nm	42nm
experimental gap size	$\approx$10 nm nm	$\approx$15 nm	$\approx$70 nm	$\approx$110 nm

(see below). If the entire Cr layer is oxidized the expected final volume will be about twice as much as the original one (see below). Taking into account the dimensions of our sample and assuming the uniform expansion Δx in all directions (except, of course, the direction toward underlying Au layer) the expansion Δx for different Cr thicknesses is summarized in Table 2.1.

Calculations:

Cr: cubic structure (space group Im3m), a= 2.895 Å. Z=2, thus each unit cell contains two Cr atoms $\rightarrow$ $V_{unitcell} = a^3$. Effective volume per one Cr atom is V_0(Cr)= $V_{unitcell}/2 \approx 12.1$ Å^3.

Cr_2O_3: rhombohedral structure (space group R3c), a = b = 4.92 Å, c= 13.495 Å. Z=6, thus each unit cell contains 2×6=12 Cr atoms. Effective volume per one Cr atom in Cr_2O_3: $V_0(Cr_2O_3)= V_{unitcell}/12 = a^2 \times \sin(120) \times c/12 \approx 23.6$ Å^3.

Thus, the ratio of V_0(Cr) : $V_0(Cr_2O_3)$ is 1 : 1.94. (i.e. the oxidized volume is almost twice larger than the original Cr layer).

At 20-25 nm Cr layer thicknesses the actual gap size is smaller than the expansion, Δx, in the assumption of the total oxidation, whereas at higher thicknesses (35-45 nm), on the contrary, expected expansion is much smaller than the experimental gap size (table 2.1). This suggests that total oxidation might not be the only reason for gap widening.

The second reason suggested is a formation of stresses in Cr layer. Although Cr_xO_y on polycrystalline Cr layer grows mainly due to the *outward* cation diffusion [93], there is a contribution of anion (oxygen) *inward* diffusion [94]. Thus, oxide is formed *within* the Cr layer, hence generating compressive stresses inside of it due to incorporation of oxygen into the lattice; mismatch in parameters of two different crystal structures (Cr and Cr_2O_3). Now let us refer to the sketch (fig. 2.5). In the presence of such shear (compressive) stresses, Cr layer is deformed (shifted) and the deformation, d, is proportional to the Cr layer thickness. Obviously, d defines the gap size and, thus, explains gap size dependence on the Cr layer thickness, which is observed in the experiment (fig. 2.3b).

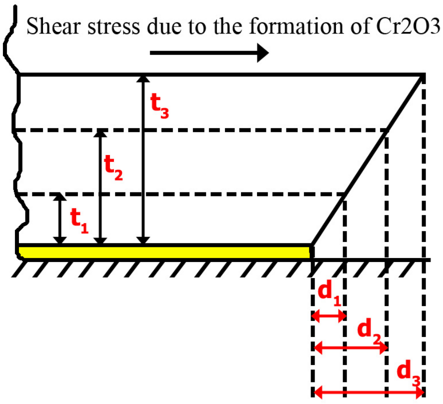

Figure 2.5 : Illustration of the correlation between the thickness of Cr layer (t) and the deformation (d) due to the formation of shear stresses (see text for details).

Besides, additional widening of the gap might be caused by the morphology of Cr/Cr_xO_y film itself, namely Cr/Cr_xO_y layer is not smooth and fine-grained (in contrast to, for example, Au film). Morphology studies known in literature and our SEM images show that the partially oxidized Cr/Cr_xO_y film is not smooth and has a fiber-like texture [92]. This fact also causes the non-uniformity (roughness) of the gap from the side of second-step electrode (since during second-step deposition the roughness of Cr/Cr_xO_y layer affects the profile of the second side of the gap). This difference in the profile of two sides is clearly seen in the SEM images (fig. 2.3a)

Significantly decreasing the thickness of the Cr layer to achieve narrow gaps increases the threat of accidental connections bridging the gap. An image of the gap produced by means of a 15-20 nm thick sacrificial Cr layer shows that the gap size is well below 10 nm (Fig. 2.3b inset), but the electrodes are not completely separated from each other with some minor connections being clearly observed in larger images.

The thickness of the Cr layer also appears to be critical in the etching process; when the Cr layer thickness is below 10 nm, the wet etching consistently resulted in the second-step Ti and Au layers landing partly on top of the first-step electrode, shorting the two electrodes. Atomic force microscopy to probe the layer thicknesses showed that Cr/Cr_xO_y layer underneath Ti/Au layer is totally etched away. Presumably, the etching rate of chromium layer is so rapid that upper Ti/Au layer sticks to the first lead before being washed away. Thus, the optimum thickness of Cr layer to assure the formation of narrowest but at the same time unconnected gaps without etching problems is 25 nm (Figs. 2.3a, 2.4, 2.6a).

2.4 Applicability of HAR gaps in Fe_3O_4 electrical characterization

First, electrodes produced with this technique on Si/SiO_2 wafers were electrically tested for shorting at room temperature (300 K). Upon voltage sweeps from 0 V to 0.1 V more than 90% of devices showed currents below the measurable limit (pA), indicating an interelectrode resistance exceeding tens of GΩ. This proves complete isolation of the two electrodes without any connections or gap irregularities narrow enough to allow tunneling.

Second, we followed the fabrication process discussed in sec. 2.2 for Si/SiO_2 wafers on the surface of 40-60 nm thick magnetite films, grown on MgO substrates [95]. The nanogaps of ≈20 nm were successfully produced (see fig. 2.6a for SEM image) without any apparent damage of the Fe_3O_4 film. We further examined the electronic properties of Fe_3O_4 devices.

As was discussed in sec. 1.2.4, recent nanoscale transport experiments of magnetite nanostructures (both nanocrystals and single-crystal thin films with lithographically defined electrodes) showed a sharp, voltage-driven transition in their electrical conduction at temperatures below T_V [10]. At a given temperature the transition voltage is observed to decrease with decreasing interelectrode gap size; thus HAR nanogaps are ideal structures for examining this transition.

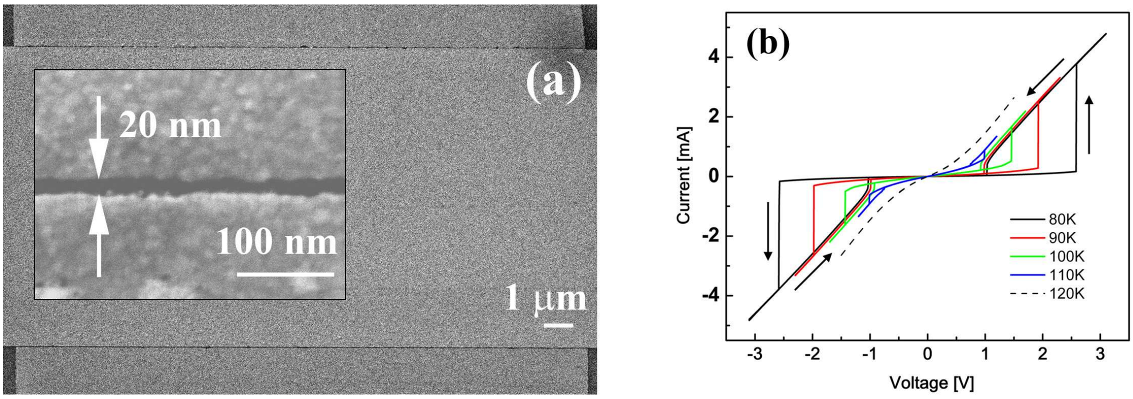

Figure 2.6 : (a) SEM images of the electrodes and gaps on magnetite film. (b) Current-voltage characteristics at different temperatures for a device produced on 50 nm magnetite film. Arrows indicate the direction of voltage sweeping.

As a representative example, Fig. 2.6b shows current-voltage characteristics of 50nm-thick film at different temperatures. Sharp conduction transitions hysteretic in voltage below 120 K are evident. Upon approaching a temperature-dependent switching-On voltage, the conductance (current) jumps 1-2 orders of magnitude, nearly approaching the conductance of the high-temperature "metallic" state of magnetite. The switching voltages increase as temperature decreases while conductance after the transition remains essentially the same.

Thus, a phenomenon, characteristic of Fe_3O_4 system [10], is observed and reproduced with electrodes, produced by the HAR fabrication technique. That means, that, first, there are no interelectrode connections (otherwise, the transport would occur through this metal bridges, not magnetite film, and show metallic behavior); second, relatively sensitive magnetite film is not damaged by the fabrication procedure and retain its properties.

Since the transition in magnetite is electric-field driven ($E = V/L$, where L is the gap size, sec. 1.2.4), the 10-20 nm gap-sized devices allow us to achieve the necessary electric field strengths for switching at relatively modest voltages (below 1V at 110 K (Fig. 2.6b), thus reducing the risk of sample damage and heating. Besides, the HAR nanogaps lead to uniform electric fields across the channel. Fabrication of magnetite devices with the required small gap spacings via the Cr HAR method has been much more reliable and consistent than attempts to do so using conventional two-step e-beam lithography [10].

2.5 Conclusions

We have developed a highly reproducible and flexible method for nanometer-sized (10-20 nm) gap fabrication with aspect ratios exceeding 1000. Modifying the original method [36] by replacing the Al layer with Cr (which also forms a “sheltering” native oxide) results in a significantly more flexible process. In addition to eliminating the sacrificial layer of SiO_2 and making etching process more chemically friendly, a recipe for effectively unlimited aspect ratios is presented with nearly 100% yield. In addition to Ti/Au metallization our technique was successfully applied to fabricate Pt, Al, Fe and pure Ti electrodes on Si/SiO_2 wafers, although we must admit that the process does not work for GaAs wafers since etchant easily damages GaAs.

Fabricated nanogap devices were used for nanoscale electrical characterization of magnetite thin films. A characteristic conductance phenomenon related to magnetite thin films [10] was observed indicating that electronic transport is dominated by the nanometer region between electrodes and there are no interelectrode connections ("shorts") along gaps tens of μm wide. The Cr HAR gaps technique is a powerful method which opens a door for investigation of many systems. This technique will be referenced as "Cr HAR method" in the following chapters.

Chapter 3

The origin of hysteresis in *I*-*V* curves of magnetite

3.1 Introduction

In sec. 1.3.1 we introduced the concept of resistive switching phenomenon (RS) and gave classification and a brief overview of numerous RS systems. Depending on the mechanism and nature of the RS system, the shape of observed *I*-*V* curves is different. In most cases, corresponding forward (up) and reverse (down) sweeps of *I*-*V* characteristics show hysteresis, *i.e.* in sweeps up and down in bias voltage, the current does not retrace itself (see fig. 1.10e, f in sec. 1.3.1 for examples).

In the majority of RS systems, while sweeping out a hysteresis loop in *I*-*V* with a switch to a low resistance state at high bias, the low resistance state persists down to zero current as voltage approaches zero. This behavior is often the case for RS systems where the switching is based on metallic filament formation at a transition point [83, 96]. However, for some RS systems, the low-resistance state persists only in some voltage interval, and the system returns to the high-resistance state before voltage returns to zero. This is the case for some metal oxides [82, 97, 98] as well as for magnetite nanostructures [10, 99]. Compare, for example, the shape of $\log|I|$ vs V plots (a common data representation for RS systems) for NiO [13] and Fe_3O_4 in fig. 3.1a.

In this part we determine the origin of hysteresis in magnetite structures. We sweep voltage in a pulsed manner (in contrast to conventional continuous sweeping) with controlled pulse parameters. We demonstrate that the shape of the hysteresis

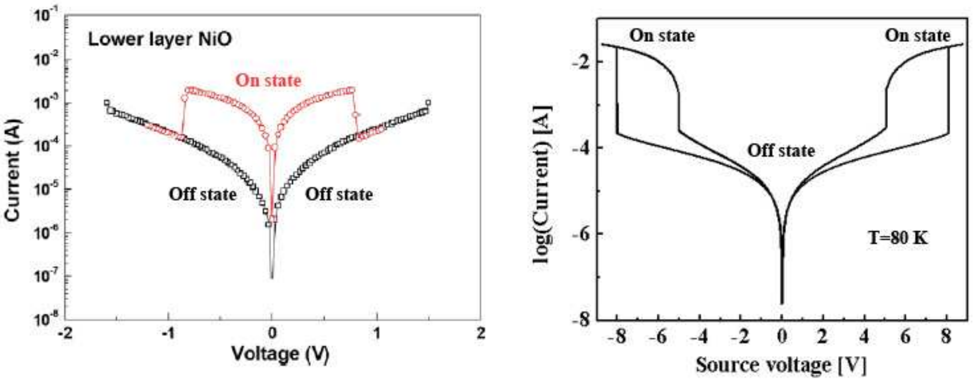

Figure 3.1 : (a) An example of unipolar I-V curve in log$|I|$ vs V coordinates (NiO system) demonstrating that the On state persists down to zero current as voltage approaches zero [13]. (b) An I-V curve of Fe_3O_4-film device in the same coordinates showing that the On state persists only in some voltage interval.

loop depends on pulse parameters, and reduces to a hysteresis-free "jump" of the current if thermal relaxation time is rapid compared to the time between voltage pulses. A simple relaxation time thermal model is proposed that captures the essentials of the hysteresis mechanism.

3.2 Experimental details. Continuous and pulsed voltage sweeps.

For this set of experiments we used magnetite thin films on MgO substrate with a 50 nm thickness. Devices for two-terminal measurements were prepared by electron beam lithography. A channel length 190 - 900 nm is defined by two 5 - 10 μm wide current leads (Fig. 3.3a inset) which are connected to micrometer-size pads (300 × 300 μm). Upon testing several different contact metals (Au, Pt, Cu, Fe and Al), copper showed the lowest contact resistance with the magnetite film. Thus, the electrodes were made of 6 nm Cu / 15 nm Au thin layers deposited by electron beam evaporation.

Electrical characterization of the samples was performed by a standard two-terminal method using a semiconductor parameter analyzer (Hewlett Packard 4155A). The voltage was applied to the source lead with the drain grounded, and current flowing through the channel was monitored. Two different measurement regimes were used: a continuous (staircase) or pulsed voltage sweeps. In continuous regime the voltage was increased (sweep up) or decreased (sweep down) in a "staircase" manner (fig. 3.2a). The duration of each voltage step is defined by integration time (short, medium or long) and can be 640 μs (short), 16.7 ms (medium), or 266 ms (long). In a typical continuous voltage sweep medium intergration time was used.

In the pulsed regime, right after sourcing each voltage pulse the source voltage returns to the so-called V_{base} value before sourcing the next voltage pulse (fig. 3.2b). In the pulsed regime we can control the duration of voltage pulse (pulse width), the time between two sequential pulses (pulse period) and the base voltage, V_{base} (see fig. 3.2b). The key point of using the pulsed regime rather than the continuous regime is that, if V_{base} is set to zero volts, the channel has an opportunity to cool down between pulses, thus minimizing Joule heating.

Each voltage sweep consists of 1000 points equally spaced in voltage. Measurements were performed in the temperature range 80-300 K with 5 K steps.

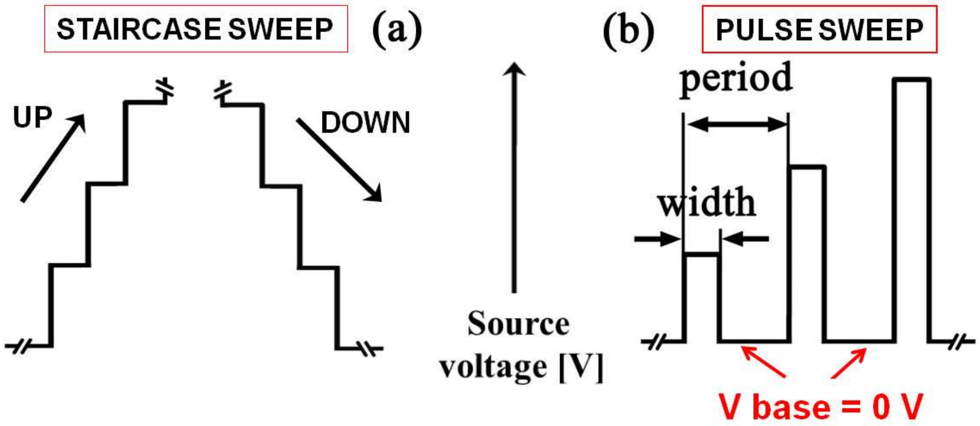

Figure 3.2 : Schematics demonstrating the voltage sourced in continuous (a) and pulsed (b) manner.

In addition to "quality control" tests of magnetite films conducted in Trinity

College (sec. 1.2.4), two-terminal zero-bias resistance, R_0, of devices was measured over 50-300K temperature range after fabrication steps. The films show a jump in the temperature dependence of resistance, R_0(T), at $T \sim$ 105-110 K (Fig. 3.3b), characteristic of the Verwey transition in Fe_3O_4. Slightly lower Verwey temperature, T_V, of 105-110 K, compare to the bulk T_V=120K, must be related to some oxidation of the film surface during the fabrication process.

3.3 Dependence of hysteresis shape on pulse parameters

At high temperatures I-V curves have a slightly non-linear shape (Fig. 3.3a, b) typical for many transition metal oxides. Below a certain temperature, coincident with the Verwey temperature inferred from measurements of the zero-bias resistance, a sharp jump in current was observed as the source voltage reached a critical value (fig. 3.3c), characteristic of Fe_3O_4 system (sec. 1.2.4, [10, 99]). At 80 K, for example, the current changes abruptly by a factor of 100 at a particular switching voltage. The state after transition (On state) shows an approximately linear I-V dependence with a much smaller differential resistance than that of high-resistance (Off) state prior to the transition. At a given temperature and device geometry, the switching happens at a critical voltage, V_{sw}^{On}, and as the voltage is swept back the system remains in the On state until it switches back to the Off state at a switch-off voltage, V_{sw}^{Off}. For a continuous staircase sweep V_{sw}^{Off} is always lower than V_{sw}^{On}, resulting in well defined hysteresis (Fig. 3.3c). The transition is symmetrical along V-axis, with identical transitions occurring at positive and negative voltage sweeps.

Switching phenomena are observed at temperatures right below the Verwey temperature (~108 K) and, thus, magnetite is comparatively insulating in the undisturbed state (see zero-bias R vs T dependence in Fig. 3.3b). In sec. 1.2.4 and in [10] we demonstrated that the observed transition is driven by electric field, not by

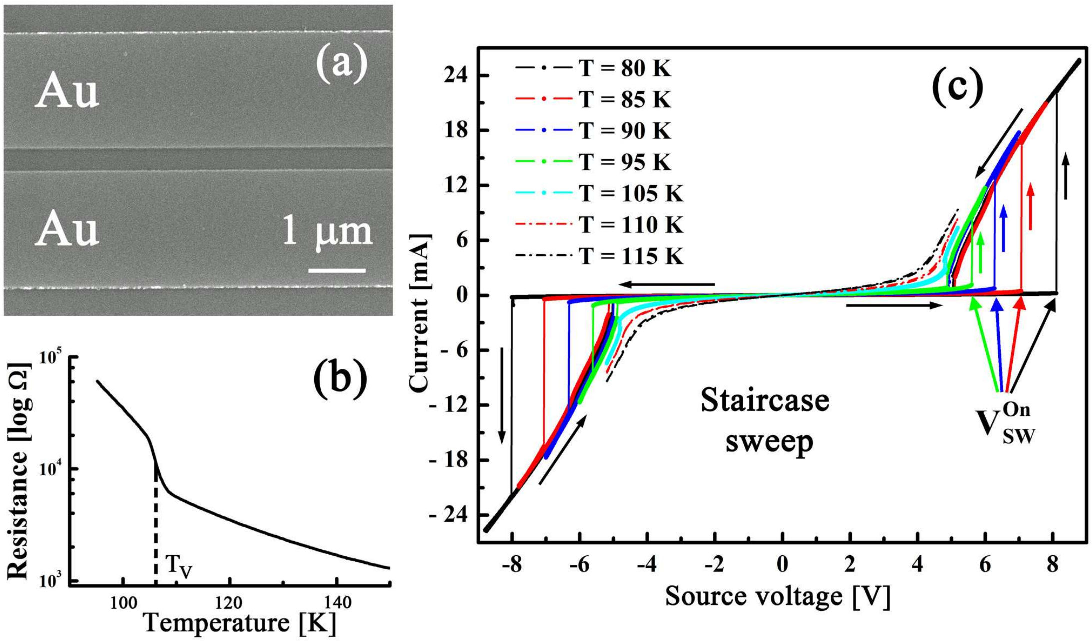

Figure 3.3 : (a) An example of SEM image of a two-terminal device (current leads) on the surface of a magnetite film. (b) A temperature dependence of resistance demonstrating Verwey transition at $T_V \sim 108$ K.(c) Typical I-V curves at different temperatures in staircase mode. Arrows indicate the direction of voltage sweeps. Above a certain temperature (in this case $\sim$ 105 K) sharp jumps in current are not observable.

thermal heating of the magnetite sample above Verwey temperature. In the high resistance state ($|V| < V_{sw}^{On}$) heating of the sample is comparatively negligible, whereas in the On state dissipated power significantly increases, making Joule heating of the sample much more likely. To explore this issue, we applied voltage in a pulsed manner (fig. 3.2b).

In the very first try of applying voltage in pulsed regime at 80 K (0.5 ms width, 10 ms period) we could see that the shape of hysteresis in I-V curve dramatically changes compared to that observed in a staircase sweep (fig. 3.4b). In the staircase regime there is a smooth, nearly linear I-V branch when voltage is swept down. While in the pulsed regime, an abrupt jump in current back to high-resistance state is observed at higher voltages. The switching back voltage, V_{sw}^{Off}, moves closer to switching On voltage, V_{sw}^{On} (fig. 3.4b).

3.3.1 Different pulse periods.

We further investigated the system response to pulse sweeps with different *periods*, while keeping the pulse width constant (fig. 3.4a). Fig. 3.4b shows resultant I-V curves (only positive voltages for better visualization) at 80 K. V_{sw}^{Off} position moves closer to V_{sw}^{On} value as period is increased, while V_{sw}^{On} remains independent of pulse period. Fig. 3.4c shows another example of hysteresis shape dependence on pulse period, demonstrating the same trend (pulse width is 1 ms).

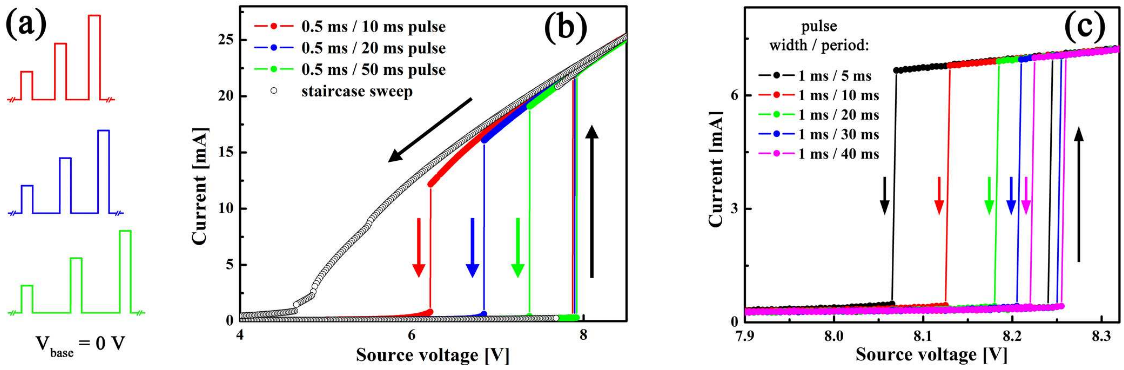

Figure 3.4 : Hysteresis shape dependence on pulse period: (a) Pulse schemes showing increasing pulse period, while pulse width remains the same. (b) Comparison of hysteresis (I-V curve) shapes in continuous and pulsed regimes and demonstration of V_{sw}^{Off} shift as pulse period increases. The colors of I-V curves correspond to the colors of pulse schemes in (a). (c) Another example of hysteresis shape dependence on pulse period while pulse width is kept the same (1 ms). Base voltage, V_{base}, is always set to 0 V, T=80 K.

At long enough period times (> 50 - 100 ms) V_{sw}^{On} and V_{sw}^{Off} are the same value. Fig. 3.5a shows I-V curves at different temperatures obtained by pulse sweeps with a 100 ms pulse period. One may compare them with the I-V curves for the same device at the same temperatures in continuous regime (fig. 3.3c). Instead of hystereses there are sharp jumps in On state and back to Off state at almost the same voltage: $V_{sw}^{Off} \approx V_{sw}^{On}$.

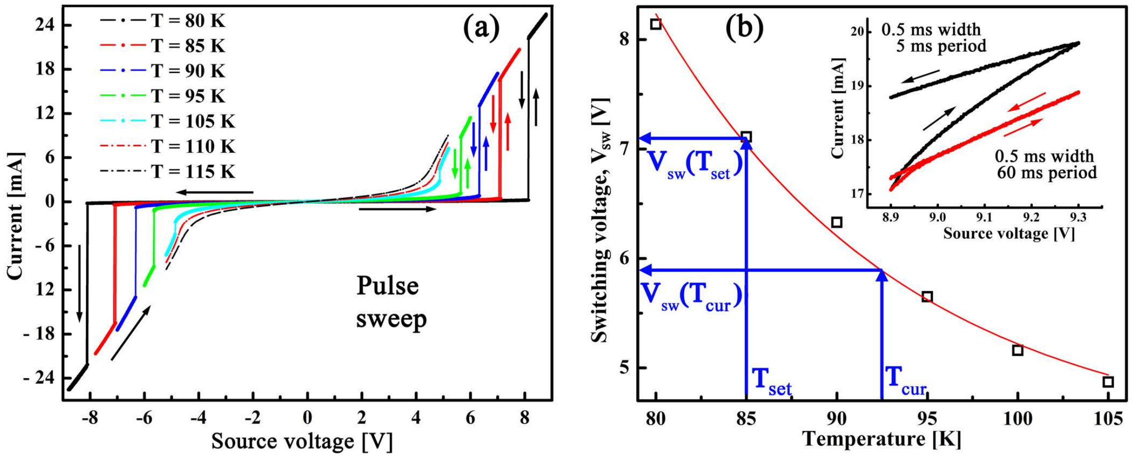

Figure 3.5 : (a) Typical *I*-*V* curves at different temperatures in pulsed mode (0.5 ms width, 100 ms period). Arrows indicate the direction of voltage sweeps. (b) Temperature dependence of switching voltage (open squares) and its exponential fit (solid line). The inset demonstrates *I*-*V* curves in the On state in pulse sweep mode with the same pulse width (0.5 ms) but different pulse periods.

While hysteretic RS (with differentiated V_{sw}^{On} and V_{sw}^{Off} values) was previously observed in many systems, here we demonstrate that in magnetite there is a single *intrinsic* switching value, $V_{sw} = V_{sw}^{On} = V_{sw}^{Off}$, and no intrinsic hysteresis. Thus, the switching voltage is a characteristic parameter of the system: at every temperature and device geometry, there is a certain switching voltage required to drive the transition. This V_{sw} decreases as temperature approaches T_V, following a nearly exponential dependence (Fig. 3.5b).

In fact, at a fixed temperature and fixed pulsed parameters switching position, V_{sw}^{On} is *not* exactly the same in different sweeps, but there is several mV sweep-to-sweep variability, *i.e.*, V_{sw}^{On} is distributed with some width along V-axis. Besides, the width of the distribution seems to vary from one temperature to another, becoming broader at lower temperatures. The V_{sw}^{On} distributions will be thoroughly investigated and explained in sec. 5. For now we point out that even the biggest oscillation at 80K is only about ± 20 - 30 mV which is very small compare to the V_{sw}^{On} value itself and further in this part, we will reference to V_{sw}^{On} at a certain temperature as a single characteristic value, V_{sw} (fig. 3.5b).

As can be clearly seen in fig. 3.5a, at a certain measurement temperature, T_{set}, if applied voltage is smaller than a characteristic V_{sw} at this temperature, $V_{source} < V_{sw}(T_{set})$), then the system is in Off state. If $V_{source} > V_{sw}(T_{set})$, then the system is in On state. Keeping this in mind, the separation of V_{sw}^{On} and V_{sw}^{Off} values, shifting of V_{sw}^{Off} position in various pulse period (as well as pulse widths, see below) sweeps, and the observation of hysteresis are easily explained by heating of the sample in the On state above the initial temperature, T_{set}.

The sample begins at an initial temperature T_{set}; for this temperature and a given channel length, there is a corresponding switching voltage, $V_{sw}(T_{set})$ (fig. 3.5b). Let us consider performing a sweep with pulse parameters selected to give hysteresis. First, as we start sweeping voltage from 0 V up, the system remains approximately at T_{set} prior to the transition point due to the comparatively small amount of Joule heating (because magnetite is in insulating state and current is low). After application of a pulse with $V > V_{sw}(T_{set})$, the system is driven into the On state. With the resulting increased conductance (and, thus, current) the Joule heating of the channel is much larger, elevating the local effective temperature of the channel to $T_{cur} > T_{set}$. Non-steady-state warming of the sample continues further in the On state. This is clear from the non-linear increase of the current and the fact that the I-V trace in the On state does not retrace itself (Fig. 3.5b inset). Note that sufficiently increasing the pulse period does allow I-V curves to retrace themselves on up and down sweeps (Fig. 3.5b inset). As the pulse voltage is swept back below $V_{sw}(T_{set})$, the channel remains in the On state because the channel is at the elevated effective temperature, T_{cur}, and the switching voltage is therefore lower: $V_{sw}(T_{cur}) < V_{sw}(T_{set})$.

If the channel cools down to T_{set} between two consecutive pulses, the system remain in the Off state for any voltage applied that is lower than $V_{sw}(T_{set})$ and jumps are observed instead of hysteresis (Fig. 3.5a). If the pulse period is short compared to the thermal relaxation time, then the channel remains at $T_{cur} > T_{set}$, and we observe the separation of $V_{sw}^{On} = V_{sw}(T_{set})$ and $V_{sw}^{Off} = V_{sw}(T_{cur})$, and resulting hysteresis. Upon increasing the pulse period (system stays longer at $V_{base} = 0$ V), the channel has more time to cool after application of previous pulses, T_{cur} is closer to T_{set} and V_{sw}^{Off} moves closer to V_{sw}^{On} in excellent agreement with the experimental data (Fig. 3.4b, c).

3.3.2 Different pulse widths.

To further support the heating origin of hysteresis we made a set of experiments with different pulse *widths*, while keeping fixed the time system stays at base voltage (pulse period - pulse width = const, ($V_{base} = 0$ V), see fig. 3.6a). The shape of the hysteresis clearly changes as well as pulse width increases.

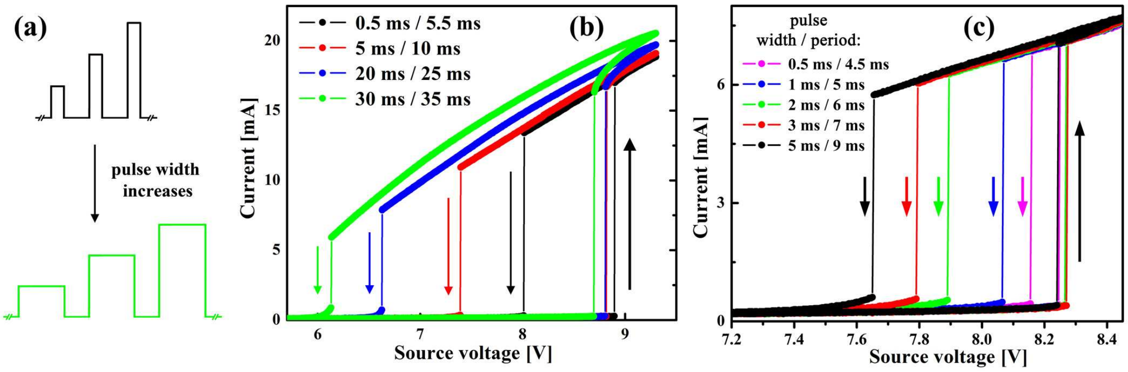

Figure 3.6 : Hysteresis shape dependence on pulse width: (a) Pulse schemes showing increasing pulse width, while the time system stays at base voltage is kept fixed. (b) Evolution of hysteresis shape as pulse width changes and demonstration of V_{sw}^{Off} decrease (left shift along V-axis) as pulse width increases. The colors of *I*-*V* curves correspond to the colors of pulse schemes in (a). (c) Another example of hysteresis shape dependence on pulse width. Base voltage, V_{base}, is always set to 0 V, T=80 K.

Fig. 3.6b shows a set of *I*-*V* curves with widths varying from 0.5 ms to 30 ms and time at $V_{base} = 0$ V equals to 5 ms. The increase of pulse width, though, has an opposite effect on V_{sw}^{Off} position than the increase of pulse period: V_{sw}^{Off} moves farther away from V_{sw}^{On} as the pulse width increases (fig. 3.6b). Fig. 3.6c shows another example of hysteresis shape dependence on pulse width, demonstrating the same trend (time at $V_{base} = 0$ V is 4 ms).

This behavior is completely consistent with the heating picture. Obviously, longer pulses heat the channel more than shorter pulses. Thus T$_{cur}$ is higher for longer pulses and switching back happens at lower voltages $V_{sw}(T_{cur})$. Note, also, that the current in On state is consistently higher for longer pulses (fig. 3.6b, c), proving the heating of the channel once again. At the same time V_{sw}^{On} position remains independent of pulse width (fig. 3.6b, c) as well as of pulse period (fig. 3.4b, c).

3.4 Modelling V_{sw}^{Off} position.

3.4.1 Relaxation time model.

As was qualitatively described above, V_{sw}^{Off} position is related to the current local temperature of the channel. To quantitatively describe the movement of V_{sw}^{Off} position in sweeps with different pulse parameters, we should consider a model to estimate the effective channel temperature as a function of applied pulsed voltage (and time). Detailed thermal modeling is very challenging because of the highly local character of the heating and the difficulty of capturing all the relevant heat transfer processes in these nanostructures. Instead we consider a simple model where the return to equilibrium state (relaxation) is described by a relaxation time, τ [100], and the temperature change is:

$$\frac{\partial T}{\partial t}(relaxation) = -\frac{T - T_{set}}{\tau} \tag{3.1}$$

where T is a current temperature of the channel. The heat flux into the sample is obviously $dQ_{in}/dt = V \times I$. We further assume the heat dissipation can be simply described as

$$\frac{dQ_{out}}{dt} = -C_v \frac{T - T_{set}}{\tau}, \tag{3.2}$$

where C_v is a heat capacity of the sample (in Joule/K).

Note that this model assumes C_v and τ to be independent of temperature, which is clearly an idealization. The temperature variation with respect to time, $\partial T/\partial t$, considering total heat flux through the system, *i.e.* $\frac{\partial}{\partial t}(Q_{in} + Q_{out})$, is given by:

$$C_v \frac{\partial T}{\partial t} = \frac{\partial}{\partial t}(Q_{in} + Q_{out}) = V \times I - C_v \frac{T - T_{set}}{\tau}. \tag{3.3}$$

By solving Eq. (3.3) we derive an expression for a temperature, $T(t + dt)$, given the current temperature, $T(t)$, in a moment of time, dt:

$$T(t + dt) = T_{set} + \frac{V \times I \times \tau}{C_v}[1 - \exp{(-\frac{dt}{\tau})}] +$$

$$+[T(t) - T_{set}] \exp{(-\frac{dt}{\tau})} \tag{3.4}$$

When $V \neq 0$, both heating and cooling (by relaxation to equilibrium T_{set}) processes occur described by second and third terms of the right side of Eq. (3.4), respectively. Between pulses (V_{base}=0 V) only heat dissipation takes place and Eq. (3.4) reduces to the expected exponential decay of the temperature with the relaxation time, τ, as a scaling factor:

$$T(t + dt) = T_{set} + (T(t) - T_{set}) \times \exp{(-\frac{dt}{\tau})} \tag{3.5}$$

There are two fitting parameters in this model that govern the evolution of the current temperature: heat capacity, C_v, and relaxation time, τ.

An example of T variation calculated by Eq. (3.4) is shown in fig. 3.7 with real experimental data for sourced voltage, V, and measured current, I (3 ms-width, 7 ms-period pulse sweep), and C_v and τ values as will be discussed below.

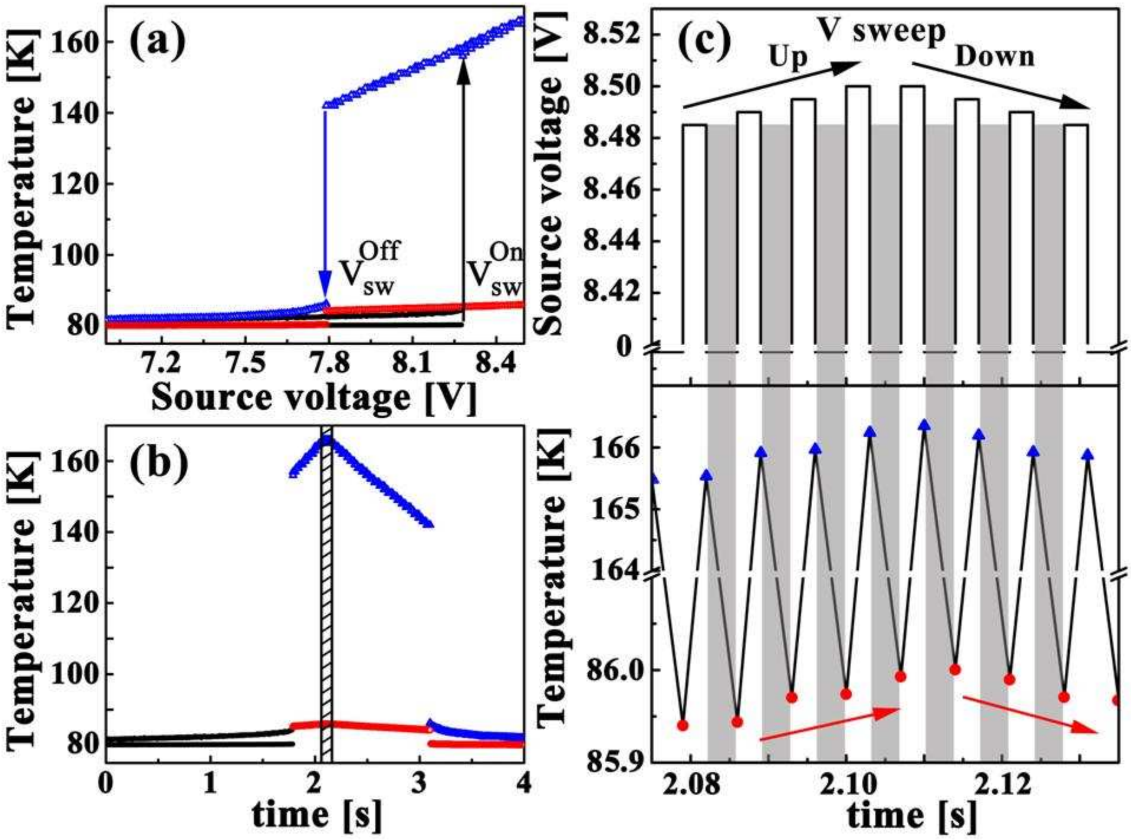

Figure 3.7 : Calculated temperature in relaxation-time model [see eq. 3.4] with respect to (a) source voltage and (b) corresponding time for a voltage pulse sweep with 3 ms pulse duration and 7 ms pulse period. Black points reflect T values before the transition point $V < V_{sw}$. After the transition point, blue triangles show T immediately after pulse application and red circles show T after relaxation between two sequential pulses. The hatched area in (b) indicates the time interval depicted in detail in (c): Applied pulsed voltage as a function of time (top) with corresponding calculated temperature of the channel (bottom). Shaded areas indicate time intervals when system is not under bias (*i.e.*, source voltage is zero) and only relaxation to T_{set} is taking place [see eq. 3.5].

Figs. 3.7a and b show the calculated temperature of the channel as a function of source voltage and corresponding time, respectively, over a large voltage range around transition point. Black points represent T values before the transition to the On state and they do not deviate much from T_{set} (80 K in this case). As the system is switched to the On state the temperature profile changes drastically: As pulse voltage is sourced, T increases and blue triangles show the calculated T values right after pulse application ("high-T" state). After relaxation for a time between pulses, the channel cools down to temperatures represented by red circles ("low-T" state) which are only slightly higher than original T_{set}. For better visualization, Fig. 3.7c zooms into the small region indicated by the hatched area in Fig. 3.7b at a turning point of a sweep (from sweep up to sweep down in voltage). It clearly demonstrates how the temperature first rapidly rises as the pulse is applied and then decreases as the system rests at $V_{base} = 0V$ (shaded regions), relaxing back toward $T_{set} = 80$ K. Both "high-T" and "low-T" temperatures follow the applied voltage: T increases as V is swept up and starts decreasing as sweep is reversed and V decreases [follow the red circles and blue rectangles in the bottom of Fig. 3.7c].

Each device has its defined single-valued $V_{sw}(T)$ function (an example is shown in Fig. 3.5b) with V_{sw} being a characteristic parameter at a certain temperature. During a voltage sweep *down*, the temperature at the moment the pulse is applied decreases (follow the red circles in Fig. 3.7c) while V_{sw} corresponding to this temperature increases. Note that when the pulse voltage is applied the relevant temperature is that of the "low-T" state (red circles in Fig. 3.7c bottom), thermally relaxed after application of the preceding pulse. Switching from On to Off states happens as soon as applied pulse V value is lower than V_{sw} for the *current* temperature of the channel at the time the pulse is applied.

3.4.2 Experimental data fit.

We found that the proposed model can match experimental V_{sw}^{Off} positions with appropriately chosen C_v and τ values. For each device at a given T_{set} we can find a C_v and τ pair which accurately describes the shifting of V_{sw}^{Off} position for sweeps with different pulse widths and the same time between pulses (pulse period - pulse width = const). An example of temperature dependence on applied pulsed voltage is shown in Fig. 3.8a corresponding to experimental *I*-*V* curves in fig. 3.6c. The adjusted optimum values of C_v and τ are 10^{-6} Joule/K and 1.5×10^{-3} seconds, respectively.

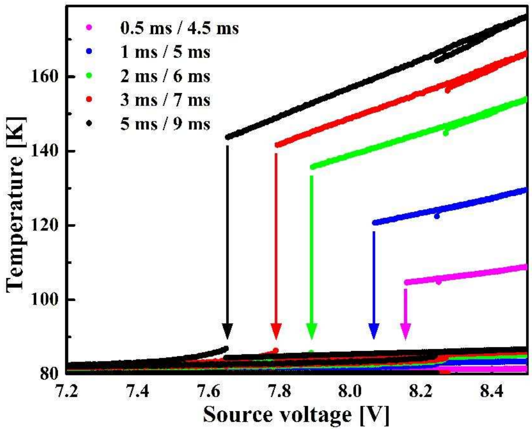

Figure 3.8 : The dependence of calculated temperature on source voltage for sweeps with different pulse widths and the same time between pulses (4 ms), T_{set} = 80 K. “High-T” (immediately after pulse application) and “low-T” (after relaxation between pulses) state temperatures are plotted in the same color, with the latter apparent at the bottom of the figure. Arrows indicate switching back position for each sweep which happens when applied voltage becomes lower than V_{sw} for a current temperature of the channel.

To get a sense of what these parameter values imply, we note that the estimated heat capacity value based on specific heat capacity and density of magnetite [$C_v \sim$ 40 Joule/(mol×K) at 80 K [2], $\rho = 5.18$ g/cm^3] and geometrical parameters of the channel is $\sim 10^{-13}$ Joule/K. This is much lower than C_v value required by the model to match the observed trends, strongly implying that heating is not confined only to the channel, but involves a much larger volume. This also implies that the MgO substrate and Au electrodes are relevant to the thermal relaxation process.

For sweeps with different pulse periods and the same pulse width, V_{sw}^{Off} positions cannot be satisfactory modeled with a single C_v and τ pair. For a fixed C_v, sweeps with longer pulse periods demand larger τ values to match the experimentally observed V_{sw}^{Off} positions. Longer period times imply larger temperature variation over the time, relaxation process takes place (see Eq. (3.5)). This is almost certainly due to the failure of the idealized assumption of C_v and τ being independent of temperature. A much more sophisticated thermal model (incorporating the spatial temperature distribution and the temperature dependent thermal properties of the magnetite, the substrate, and the electrodes) is likely necessary for a complete quantitative picture.

Since heating effects in the On state are responsible for hysteresis in this system, it is worthwhile to review the arguments that the high resistance to low resistance transition itself is *not* driven by heating the sample above T_V, but indeed is driven by electric field [10] (see sec. 1.2.4). First, a strong argument against heating effect is the temperature dependence of the power, P_{sw}, dissipated at the transition point. It was shown in Ref. [10] for two-terminal devices that $P_{sw}^{2T} = V \times I$ at V_{sw}^{On} decreases as temperature decreases. This behavior is incompatible with the assumption that raising of the channel temperature above T_V (here T_V ~108 K) is responsible of the resistance switching (see sec. 1.2.4 for detail). Assuming a heating effect, the lower the set temperature the more power should be provided to warm up a channel

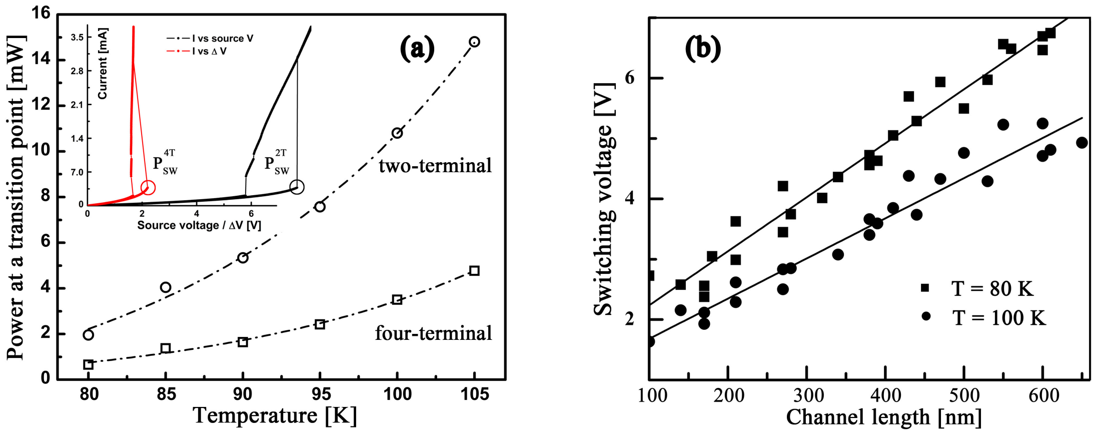

Figure 3.9 : (a) Temperature dependence of the power at a transition point in two-terminal ($P_{sw}^{2T} = V \times I$) and four-terminal ($P_{sw}^{4T} = \Delta V \times I$) experiments. Inset shows transition points in I-V and I-ΔV curves. (b) Dependence of the two-terminal switching voltage, V_{sw}, on the channel length at two different temperatures. Solid lines represent linear fit, the slope of the line reflect the electric field strength to drive a transition.

above T_V, the opposite of the trend observed in the experiment. We made two-terminal measurements, calculated P_{sw} at a transition, and the results confirmed the P_{sw} vs T dependence in the two-terminal geometry (fig. 3.9a). Additionally, we performed four-terminal measurements (see sec. 4.2) and calculated the corresponding local switching power dissipated in the channel, $P_{sw}^{4T} = \Delta V \times I$ at a transition point, where ΔV is a voltage difference between two voltage probes within the channel. P_{sw}^{4T} is much lower than P_{sw}^{2T} because of the significant contact voltage drop at the electrode/Fe_3O_4 interface. The power dissipated directly in the channel, P_{sw}^{4T}, shows the same temperature dependence as P_{sw}^{2T} (Fig. 3.9a), arguing further against simple heating driving the transition.

A second argument for that the transition is electrically driven is the dependence of V_{sw} on the length of the channel. At each temperature V_{sw} scales *linearly* with the channel length, L (fig. 3.9b). This implies that at each temperature there is a certain electric field necessary to drive a transition. Extracted from the slope of V_{sw} vs. L, the critical electric field value is about 7×10^4 V/cm at 105 K and it increases slightly up to ∼10^5 V/cm down to 80 K (Fig. 3.9b). These values are much lower than the catastrophic dielectric breakdown field (∼10^7 V/cm) [101] for most insulators.

Third, pulse experiments that widely span heating conditions show no shift in V_{sw} position upon varying either pulse width or pulse period. Longer pulses deliver more energy to the channel [$= I \times V \times t$, where t is the duration (width) of the pulse]. Assuming a thermal switching mechanism, the switching would be expected at lower voltages for longer pulses, which is not the case in the experiments. Different pulse widths and periods have tremendous effects (both in V_{sw}^{Off} positions and current values) on the behavior of the system in the On state (Fig. 3.6b, c, 3.4b, c) when heating is clearly an issue. In the Off state only minor changes in I-V curves were detectable for sweeps with all available widths and periods. Finally, sourcing a constant voltage for minutes right below V_{sw} value at a certain temperature does not induce or alter the transition.

3.5 Conclusions.

In this chapter we have found out the origin of hysteresis in I-V curves of magnetite. Through extensive voltage pulse measurements with controlled pulse parameters, we unambiguously show that the hysteretic behavior originates from local Joule heating of the channel once the system is switched to the low-resistance, On state. We addressed once again the arguments, why the observed switching itself is indeed driven by electric field, and provided some additional supporting experiments. We found that a simple relaxation time model of the thermal processes can describe the shifting of V_{sw}^{Off} positions for sweeps with different pulse parameters. Model parameters (heat capacitance, C_v, and relaxation time, τ) indicate that the substrate and electrodes are important in determining the thermal dynamics of the system.

The EFD transition observed in magnetite is inconsistent with several mechanisms suggested for RS in widely investigated perovskites, such as dynamics of oxygen vacancies and interfacial effects. First, the lack of intrinsic hysteresis differentiates magnetite RS from that in the perovskites. Second, magnetite RS can be induced only *below* the Verwey temperature, T_V, whereas RS in perovskites is observed in a wide range of temperatures [83]. Below T_V magnetite is in a correlated ordered state [57, 48]. Thus, RS in Fe_3O_4 is a strong candidate for the theoretically predicted breakdown of *charge-ordered* states by electric field [102].

Chapter 4

Interplay of bulk and interface effects in the electric-field driven transition in magnetite

4.1 Introduction. Contact resistance, R_C.

In the investigation of EFD transition in magnetite, the channel length is a crucial parameter. On the one hand, two electrodes should be separated by only several hundreds of nanometers or less in order for the transition to be observed. This is why the EFD transition in magnetite was not discovered during 70 years of intense investigation of $\mathrm{Fe_3O_4}$ [3, 43], and only recent advances in nanofabrication and film growth allowed electrical characterization at previously inaccessible scales. Only for small channel lengths is the electric field needed to drive the transition accessible at relatively low voltages, thus preventing both excessive heating and damage of the sample. Application of high bias to "bulk" magnetite induced transitions driven by Joule heating of the samples above T_V [71, 72].

On the other hand, the downside of such small channel length experiments is an unavoidable, dominant contribution of the contacts, which prevents direct insight into the properties of magnetite before and after transition. For example, in the two-terminal geometry, magnetite film and nanoparticle devices do not show jump (or even kink) at the Verwey temperature in their temperature dependence of two-terminal zero-bias resistance (see fig. 1.7 in sec. 1.2.4, [10])

In order to estimate the magnitude of contact resistance, R_C at each temperature, we measured the two-terminal resistance for several devices with different channel lengths, L. Then, $R(L)$ linear dependence is extrapolated to $L = 0$ in order to get a R_C value (fig. 4.1). R_C of Au/magnetite interfaces comprises more than 70 % of the total resistance. A high potential Schottky barrier at the Au/magnetite interface might be the reason of the observed behavior, and care in selection of electrode metal is required.

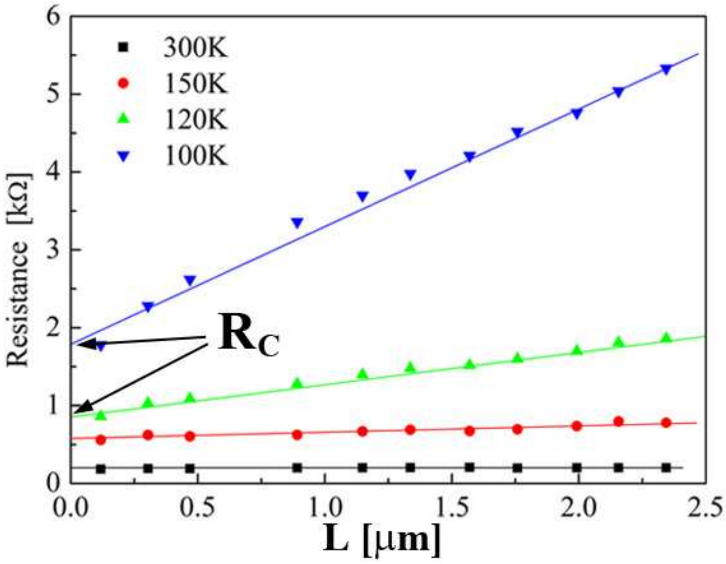

Figure 4.1 : Dependence of two-terminal zero-bias resistance on the channel lenghts at several different temperatures. Electrodes are made of 15 nm of gold. Extrapolation of linear $R(L)$ dependence to $L = 0$ gives R_C at each temperature.

One of the most effective ways to differentiate between bulk and interface effect is to make multilead measurements. Four-terminal experiments allow, first, addressing properties of solely magnetite channel without contribution from the contacts. Second, changes in the interface behavior can be monitored as a function of applied voltage or temperature.

In this chapter we describe four-terminal experiments in a lateral electrode configuration using magnetite thin films. The channel length is less than 2 μm and voltage-probe wires ~100 nm in width are directly inserted into the channel. These multilead experiments quantitatively and unambiguously separate the role of each interface and the magnetite channel. We study the changes in contact and channel resistance contributions at the onset of the EFD transition in magnetite. We first investigate the behavior of the devices made of the same metals as source and drain electrodes (Cu-Cu, Au-Au and Pt-Pt). Second, we analyze and compare the behavior of the devices with one contact electrode made of one metal and the other contact electrode made of the different metal: *i.e.*, source-drain electrodes in the following combinations: Cu-Au and Cu-Pt. Finally, we propose a switching mechanism compatible with the observed behavior.

4.2 Fabrication of four-terminal devices.

Fabrication of devices for four-terminal measurements on the surface of magnetite film with channel lengths below 1-2 μm is a great fabrication challenge. This is because two voltage probes should be patterned between source and drain electrodes to sense a voltage drop across the channel. For such small channel lengths the V probes should be very narrow wires in order to avoid shorting of source, drain and voltage probe electrodes. Devices were prepared by electron beam lithography (JEOL-6500 SEM) with careful adjustment of exposure parameters for voltage probe wires.

The metal contacts were fabricated by the electron-beam deposition. Upon preliminary testing of several different contact metals (Au, Pt, Cu, Fe and Al) in two-terminal geometry it was noticed that Cu and Fe adhere much better to the surface of Fe_3O_4 films, than Au, Pt and Al do. Good adhesion of metal contacts is critical during the In soldering step (see below) to make electrical connections to the measurement puck. Iron has a disadvantage since, being in contact with magnetite film, Fe contact layer might change the stoichiometry of Fe_3O_4 either by adsorbing oxygen or by Fe "building" into the crystal structure of Fe_3O_4. Thus, Cu was chosen to act as the adhesion layer to magnetite. In the first part of this chapter (sec. 4.4) both source and drain contacts were made of 6 nm Cu/10 nm Au. Au acted as a cover and protective layer against Cu oxidation. In the second part of this chapter (sec. 4.5) we worked with different contact metal devices and, thus, deposited 15-20 nm of an appropriate metal (see sec. 4.5.1 for fabrication details).

The patterning of electrodes directly on the surface of magnetite film has its disadvantage: relatively conductive magnetite films make possible the current paths outside of the confined channel between current electrodes, *i.e.*, offset currents. They may lead to false voltage values read by voltage probes. One of the way to avoid offset currents problem is to etch away magnetite film everywhere except the very measurement spot. We made this kind of devices by performing the following steps:

Small rectangles (10×6 μm) covered with photoresist were defined by conventional photolithography to mark the position of the central parts of the future devices. Further, photoresist acted as a protective mask during Ar^+ ion milling of magnetite film down to the MgO substate. Thin (1 nm) layer of Cr was deposited right after ion milling while photoresist was still protecting the rectangular of magnetite films and then lift-off of photoresist was performed. Conductive Cr layer helps to prevent charging effect of dielectric MgO substrate during subsequent electron beam lithography process to define leads and pads. Alignment of the e-beam pattern is performed in a way that the central part of device with source-drain leads and voltage wires were positioned right in the center of remained (unetched) magnetite rectangular while the rest of the pattern including pads rested on MgO substrate. Wet chemical etching of Cr layer (Cyantek Co., CR-7 chromium etchant, ≈300 K, 1 min.) finished the fabrication process.

Fig. 4.2a shows cross-sectional SEM image of device with one pair of voltage probe wires within the channel. A channel length of $\approx 1\mu$m is defined by two 5 μm wide source and drain leads. In most cases, though, challenging geometry and Cr protective layer lowered the resolution of electron beam lithography and prevented fabrication of voltage wires inserted deep into the channel so that no wires were patterned and only several nanometers of voltage probes were confined within the channel (fig. 4.2b).

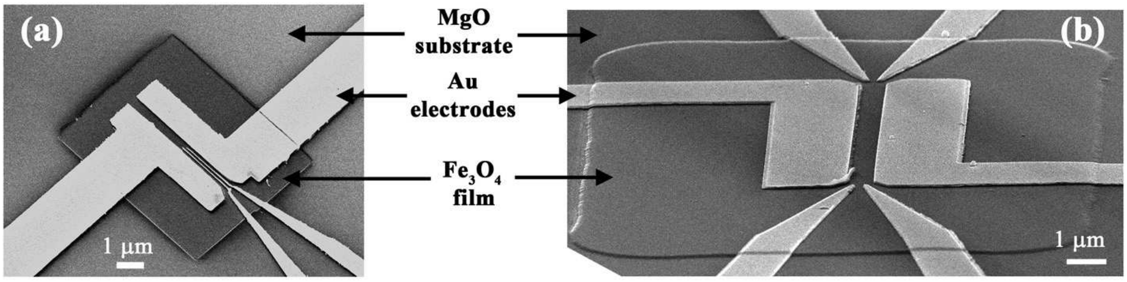

Figure 4.2 : Cross-sectional SEM images of the devices for four-probe measurements with Fe_3O_4 film etched everywhere except the very measurement spot (rectangles in the center). Device in (a) has one pair of voltage wires inserted deep into the channel. Device in (b) has two pair of voltage probes, but no wires within the channel.

As a result, these devices for four-terminal measurements should be free from offset currents during electrical measurements. But, upon electrical testing, these devices did *not* show repeated transitions (jumps in current) under high bias at $T<T_V$. In a typical experiment, once below $T<T_V$ (usually, at 80 K), when voltage was first swept in a continuous manner starting from negative value, $-V_{max}$ and its magnitude was sufficiently high, the device appeared in On state fig 4.3 and continued to be in On state as $|V|$ was decreasing just like in a regular successful *I-V* curve showing hysteresis transition. Upon reaching $+V_{max}$, however, the device did *not* show jump in current (transition to On state) at positive voltages. And upon reverse sweeping (from $+V_{max}$ to $-V_{max}$) the device remains in Off state all the way back to $-V_{max}$ (fig. 4.3) without switching to On state. Every consequent high voltage sweeps did not show any switching to On state; the sample remained in Off state at all voltages. Increasing voltage range did not induce the transition as well.

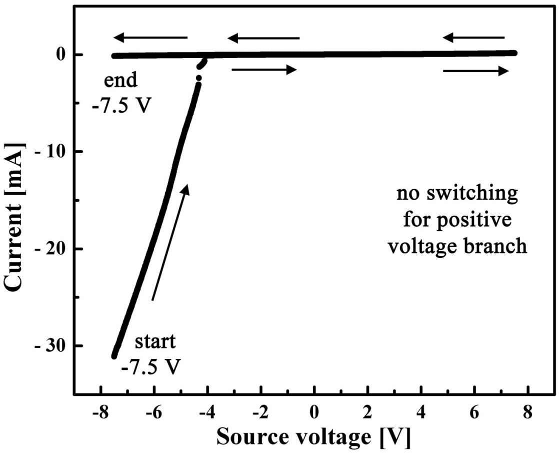

Figure 4.3 : A typical example of the first-time high voltage I-V curve at 80 K for devices with etched Fe_3O_4 films. The On state is only observed in the beginning of the sweep at the negative voltages. The system remains in Off state at both positive and negative voltages during the sweep back.

After-measurement SEM imaging revealed that magnetite films were highly damaged: apparent cracks were seen between source and drain electrodes and Au electrodes were melted (fig. 4.4a and b). The damaging of Fe_3O_4 films and the absence of hysteresis were repeated for many tested devices with etched Fe_3O_4 films.

For devices prepared directly on the surface of continuous Fe_3O_4 films (all devices discussed in sec. 2, 3 as well as in ref. [10]) no visible film damages were detected after electrical measurements. Thus, cracking of the films and the absence of hysteresis must be related to the fact that instead of continuous films there are just micrometer-sized (10 μm × 6 μm) "islands" of magnetite. We believe that the cracking of the "islands" is caused by inability of the small-sized Fe_3O_4 regions to release stresses (due to the lattice mismatch between Fe_3O_4 film and MgO substrate and possible structural changes once Fe_3O_4 is in On state) and dissipate heat effectively. Melting of Cu/Au electrodes (fig. 4.4a and b) proves that devices experienced high temperature during the voltage sweep while being in the On state.

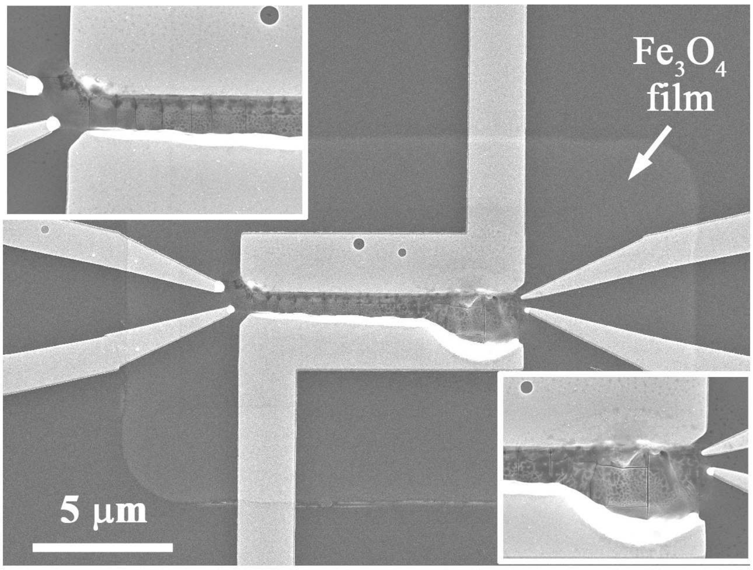

Figure 4.4 : After-measurement SEM image of four-terminal devices with Fe_3O_4 film etched everywhere except the very measurement spot (rectangular in the center). For better visualization of the cracks top and bottom insets show enlarged images of left and right parts of the device, respectively.

Since measurements of etched magnetite devices were proved not to be experimentally feasible, we have explored another way to ensure measurements free from the influence of the offset currents. Instead of etching away magnetite film one can protect its surface with some dielectric material everywhere except the very measurement region. We chose Al_2O_3 as an insulating protective layer. We first defined by photolithography the following pattern on the surface of magnetite film: a 200 μm × 200 μm square with a 12 μm × 10 μm hole in it, then deposited $\approx$ 100 nm of Al_2O_3 on top of it and then made lift-off of the photoresist. As a result, insulating Al_2O_3 covered 200 μm × 200 μm square except the 12 μm × 10 μm "islands" of magnetite film defining the position of the central part of the future device.

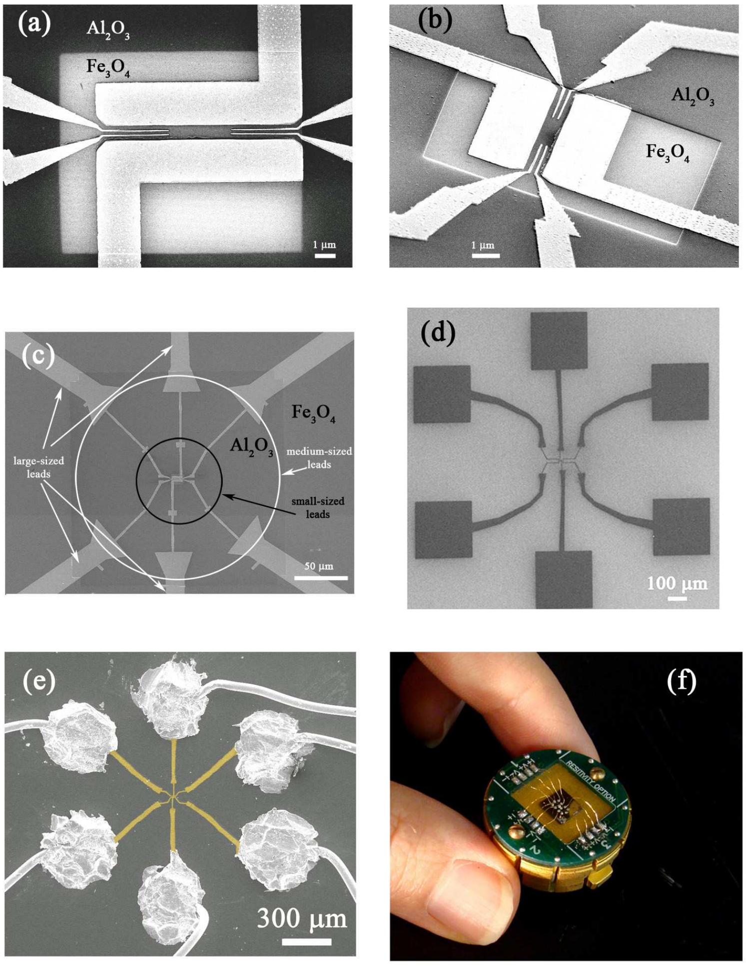

Figure 4.5 : An example of four-terminal device with Al_2O_3 protective layer. (a) Regular SEM image. The size of Fe_3O_4 rectangular is 12 μm × 10 μm (b) Cross-sectional SEM image of the same device. (c) Low-magnification SEM image demonstrating that the large-sized leads and pads (not visible here) are on the surface of magnetite film. The size of Al_2O_3 square is 200 μm × 200 μm. (d) Zoom out SEM image showing all parts of the device including 300 μm × 300 μm pads. (e) Colored SEM image demonstrating electrical contacts to the pads with further In soldering to attach Au wires. (f) Photograph of PPMS puck with Au wires attached to 12 pins.

Second, the patterns for four-probe measurement were defined by electron beam lithography. For resulting devices voltage leads touch magnetite films only in the very channel between source-drain electrodes (fig. 4.5a and b) while all other small-sized and medium-sized leads are on top of insulating Al_2O_3 layer, thus preventing any current flow through voltage probes outside of the channel. We left the large-sized leads and pads on the surface of magnetite film due to the better adhesion of Cu/Au electrodes to Fe_3O_4 rather than to Al_2O_3 (fig. 4.5c). Since they are far away from the measurement spot the possible offset currents are not to be measured.

Fig. 4.5a and b show regular and cross-sectional SEM images of four-terminal device with Al_2O_3 protective layer. The leads were connected to micrometer-size pads (300 × 300 μm) (fig. 4.5d) to which Au wires are attached by In soldering and then connected to external contacts of the puck (fig. 4.5e and f). The puck was placed into the chamber of a Quantum Design Physical Property Measurement System (PPMS, model 6000) for variable temperature measurements (300 K - 80 K). The lower temperature bound of these measurements is limited by the increasing switching voltages and concerns about device damage as T is further decreased. Devices with Al_2O_3 protective layer showed stable hysteretic transitions symmetric both at positive and negative voltages and are used for four-terminal electrical

measurements in this chapter (see below).

4.3 Calculation of R_C and resistance of Fe_3O_4 channel, R_DEV.

Electrical characterization of the devices was performed by standard four-terminal methods using a semiconductor parameter analyzer (HP 4155A). The schematic of device electrical connections is presented in Fig. 4.6a. The voltage, V_out, is applied to the source lead with the drain grounded, and current flowing through the channel is recorded. The pair of voltage probes, directly inserted into the channel between source and drain leads, senses voltages V_1 and V_2. A voltage drop in the channel without the contact contribution is then calculated as $\Delta V = V_1 - V_2$. Only one pair of voltage probes (either left or right, see fig. 4.5a) is active in a given measurement, with the second pair being intact. Having two pairs of voltage probes allows two independent sets of measurements (one for each pair of voltage probes) in a given channel, to verify data consistency in these four-terminal devices. In this chapter the voltage was always swept in a *pulsed* regime with the shortest available pulse duration (500 μs) and with pulse period $>$ 5 ms to minimize Joule heating of the channel (see sec. 3 and ref. [103]). This pulse measurement procedure greatly reduced apparent hysteresis in the transition as a function of bias sweep.

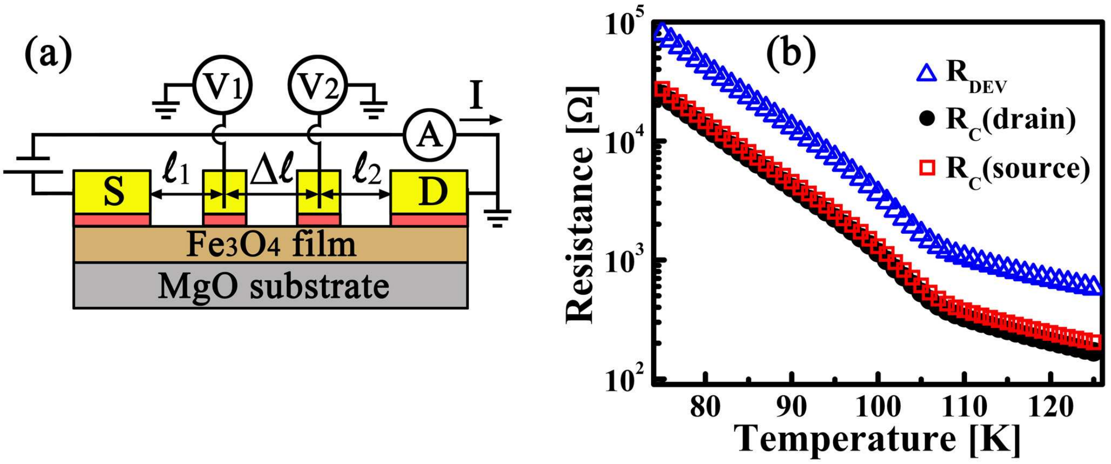

Figure 4.6 : (a) Schematics of electrical circuit of four-probe measurements. Letters S and D denote source and drain contact, respectively. Contacts are made of 6 nm Cu adhesion layer (reddish) and 10-20 nm cover layer of Au (yellow). (b) Temperature dependence of the low-bias resistance of magnetite channel (R_{DEV}) and corresponding contact resistances (R_{C}) at source and drain electrodes.

At any V_{out}, voltage first drops at source electrode/Fe_3O_4 interface (V_{C}(source)). We assume that at low source-drain biases the contact interface contributions are dominated by an Ohmic contribution, R_{C}(source)$\equiv V_{\mathrm{C}}$(source)$/I$. Then, in the assumption of a homogeneous film (medium) between the electrodes, voltage *linearly* drops across the channel, and two values are recorded at the two locations of the voltage probes (fig. 4.7). The remaining potential drop to zero volts (grounded drain electrode) occurs at Fe_3O_4/drain electrode interface (V_C(drain)$\rightarrow$ R_C(drain)) (fig. 4.7). Conventionally, the total device may be represented as a voltage drop over three resistors in series, R_C(source), R_{DEV} and R_C(drain). By knowing the geometrical characteristics of our devices from SEM images (i.e., ℓ_1, $\Delta\ell$, and ℓ_2, see Fig. 4.6a) we can calculate the values of all three voltage drops and, by dividing over measured current, corresponding resistances.

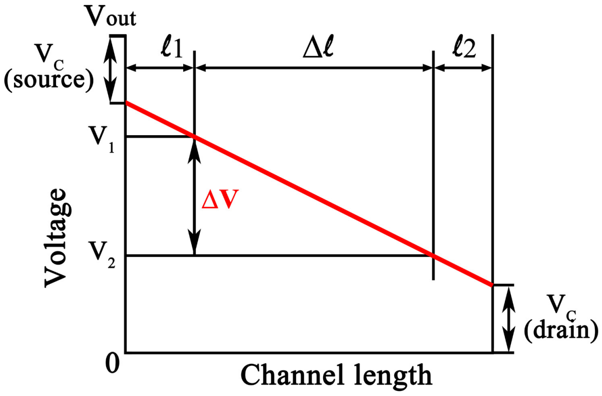

Figure 4.7 : Schematic demonstration of voltage distribution along the magnetite channel. Voltage first drops at source electrode/Fe_3O_4 interface, V_C(source). Then linearly drops across the Fe_3O_4 channel and finally goes to zero (grounded drain electrode) at Fe_3O_4/drain electrode interface, V_C(drain). The pair of voltage probes measures voltages V_1 and V_2.

The procedure of R_C(source), R_{DEV} and R_C(drain) calculation is the following: At each V_{out} after the initial voltage drop at the source electrode/Fe_3O_4 interface the voltage drops linearly across the channel, as defined by an equation:

$$V = a \times \ell + b$$

where V and ℓ are voltage and distance from source electrode, respectively (Y-axis and X-axis in fig. 4.7), and a and b are coefficients describing the straight line. By knowing measured V_1 and V_2 values as well as ℓ_1, $\Delta\ell$ and ℓ_2 from SEM images and considering (fig. 4.7)

$$V_1 = a \times \ell_1 + b$$

$$V_2 = a \times (\ell_1 + \Delta\ell) + b$$

we calculate the coefficients a and b as:

$$a = (V_2 - V_1)/\Delta\ell$$

$$b = V_1 - a \times \ell_1$$

Then, the voltage drops at the source and drain electrodes are calculated as

$$V_{\mathrm{C}}(\text{source}) = V(\ell = 0) = b$$

$$V_{\mathrm{C}}(\text{drain}) = V(\ell = L) = a \times L + b$$

where L is the total channel length $L = \ell_1 + \Delta\ell + \ell_2$ (fig. 4.7). Corresponding resistances are calculated by dividing V_{C}(source) and V_{C}(drain) over measured current: R_{C}(source)=V_{C}(source)$/I$; R_{C}(drain)=V_{C}(drain)$/I$. The voltage drop across the device is

$$V_{out} - V_{\mathrm{C}}(\text{source})\text{-}V_{\mathrm{C}}(\text{drain}) \text{ or } \Delta V \times L/\Delta\ell$$

Device resistance is calculated as $R_{\mathrm{DEV}} = \frac{\Delta V}{I} \times \frac{L}{\Delta\ell}$.

The calculations were performed using MatLab code.

An example of the temperature dependence of R_{DEV}, R_{C}(source) and R_{C}(drain), calculated this way at $V_{\mathrm{out}} = 100$mV, is presented in fig. 4.6b in the temperature range around T_{V}. The Verwey temperature is inferred for each device as an inflection point in R_{DEV}(T) dependence; and for the various devices studied in this chapter T_{V} range from 100 K to 110 K. For source and drain electrodes made of the same metal (Cu in this case), R_{C}(source) $\approx$ R_{C}(drain). We note that R_{DEV} and R_{C} have nearly identical temperature dependence (Fig. 4.6b).

4.4 Same source/drain contact metal devices

4.4.1 Channel length dependence of R_{C} and R_{DEV}

Now, let us consider the relative contributions of contacts and magnetite channel to the total voltage drop. Our assumption of linearity in the channel conduction presumes that R_{DEV} linearly scales with the channel length, L, while R_{C}(source) and R_{C}(drain) should remain independent of L. This is supported experimentally. To demonstrate this, we made a set of devices on the same piece of magnetite film with different channel lengths while all other geometrical parameters (film thickness and the width of source and drain leads) remained exactly the same for all devices. Two representative SEM images of such devices with L=1.1 μm and L=1.9 μm are shown in fig. 4.8b and c, respectively. The total (two-terminal) resistance at each temperature linearly depends on the channel length as demonstrated in Fig. 4.8a at several temperatures (85 K, 90 K and 95 K).

The calculations of contact resistances based on ℓ_1, $\Delta\ell$ and ℓ_2 for each device show that at each temperature R_{C}(source) and R_{C}(drain) are equal to each other and are the same for devices with different lengths, L. It is worth mentioning that R_{C}(source) and R_{C}(drain) do not change upon switching the grounds, *i.e.*, exchanging the place of injecting and grounded electrodes. Calculated resistances in Fig. 4.8d and e represent the data for the devices shown in Fig. 4.8b and 4.8c, respectively. While R_{C}(source) and R_{C}(drain) remain independent of channel length, R_{DEV} increases as L increases

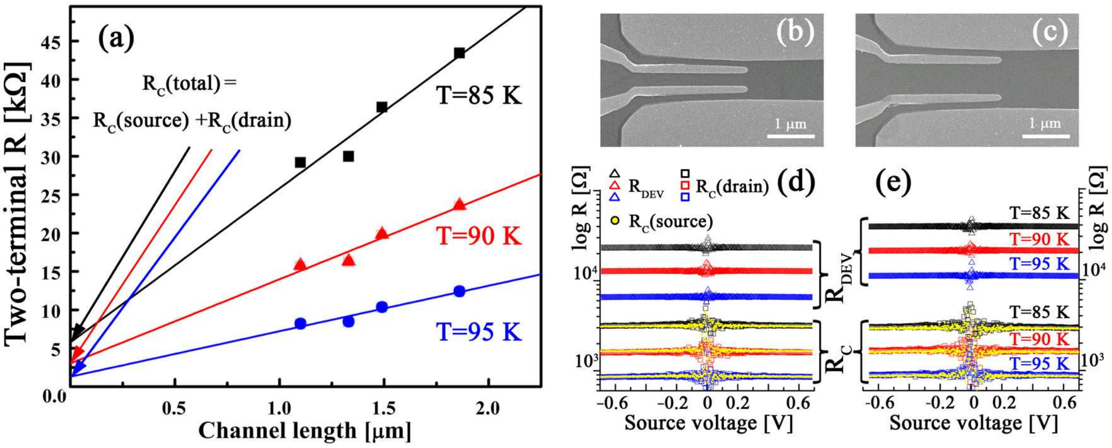

Figure 4.8 : (a) Examples of two-terminal resistance dependence on the channel length at three different temperatures (85 K, 90 K and 95 K) with corresponding linear fits. Extrapolation to zero channel length gives the total contact resistance, R_C(total), at each temperature. (b) and (c) show SEM images of devices with different channel lengths. (d) and (e) plot calculated values of device resistances, R_{DEV}, and contact resistances, R_C(source) and R_C(drain), around zero source voltage for devices in (b) and (c), respectively.

which is obvious from comparison of Fig. 4.8d and Fig. 4.8e. All three resistances increase significantly with decreasing the temperature (compare data at 85 K, 90 K and 95 K in Fig. 4.8d, e), as will be discussed below in detail. The contact resistance, R_{C}(source) + R_{C}(drain), comprises from 20% to 13% of the total, two-terminal R for devices with channel lengths ranging from 1 μm to 2 μm.

The increase in total two-terminal resistance with channel length (Fig. 4.8a) is caused by the increased contribution of R_{DEV} in longer devices. Moreover, the extrapolation of a two-terminal R vs L linear fit to zero channel length gives a resistance value very close to the sum of calculated R_{C}(source) and R_{C}(drain) at each temperature. The latter proves the consistency of our calculations and independence of contact resistances on the channel length within L range investigated here.

4.4.2 R_{C} and R_{DEV} jumps at a transition point.

At temperatures below $T_{\mathrm{V}} \sim 105K$, the current-voltage characteristics, I-V, show Ohmic behavior at low source voltage range (< 1V), while starting to exhibit non-linearities at higher voltages, symmetrical for positive and negative source voltages. Examples at two selected temperatures (80 K and 85 K) are shown fig. 4.9a. Upon further increasing source voltage, I-V curves show a sharp jump in current (fig. 4.9b) as soon as the source voltage reaches a critical switching value, V_{sw}, at a certain temperature as was described in detail in sec. 1.3.2 and Chapter 3. This is a transition from high resistance (Off) state to a state with much lower resistance (On) state. Note the two-order of magnitude difference in current after transition by comparing I-V curves before (fig. 4.9a) and after transition (fig. 4.9b).

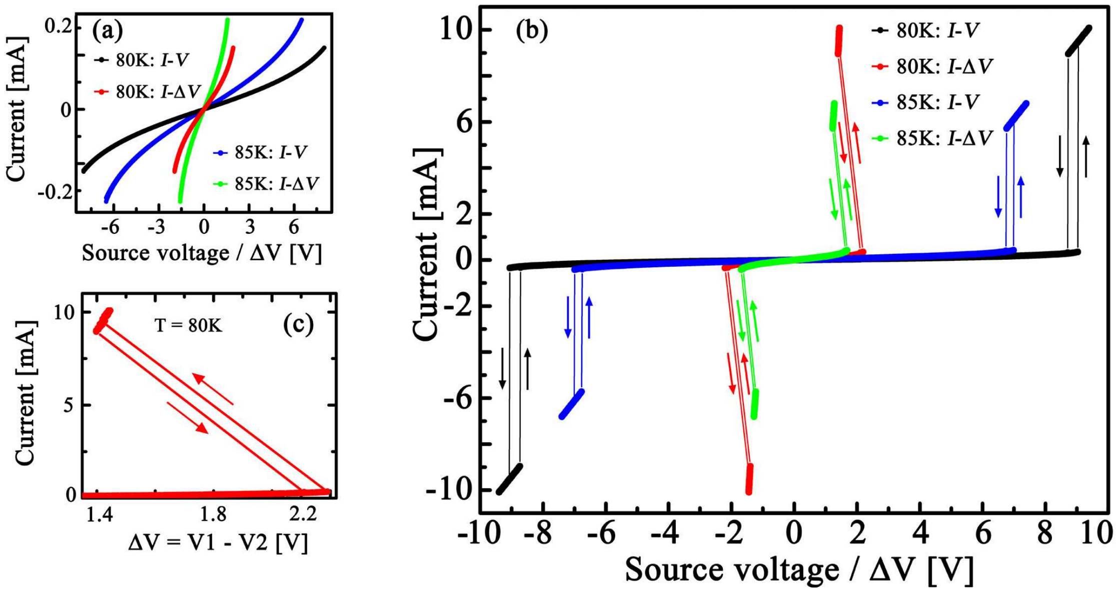

Figure 4.9 : Examples of I-V and corresponding I-ΔV curves at 80 K and 85 K (a) at the voltage range below switching voltage at each temperature (b) at the voltage ranges above switching voltage at each temperature. Arrows indicate the direction of the voltage sweep. (c) Zoom in to I-ΔV curve at 80 K around transition point demonstrating the discontinuity in measured ΔV value.

Corresponding I vs $\Delta V = V_1 - V_2$ plots (fig. 4.9b) have much lower switching

ΔV_{sw} values and reveal at a transition point not only a discontinuity in current, but also in the measured ΔV value, which decreases in absolute magnitude (fig. 4.9c). Since $\Delta V = V_1 - V_2$, in general, reflects properties of magnetite channel without contact effects, the discontinuity (jump) in ΔV at a transition point can be explained as a sudden decrease in device resistance, R_{DEV}.

Now let us turn to the quantitative description of contact effects at the onset of the field-induced transition. Calculations of R_{C}(source), R_{DEV} and R_{C}(drain) show that at a transition point the voltage drops at the contacts, V_{C}(source) and V_{C}(drain), increase in absolute value, while ΔV decreases. Compare the blue open squares (at the transition point) and red closed squares (at the next point after transition) in fig. 4.10a, which depict voltage distribution over the channel length. From this sketch the decrease in ΔV value is also clearly visible.

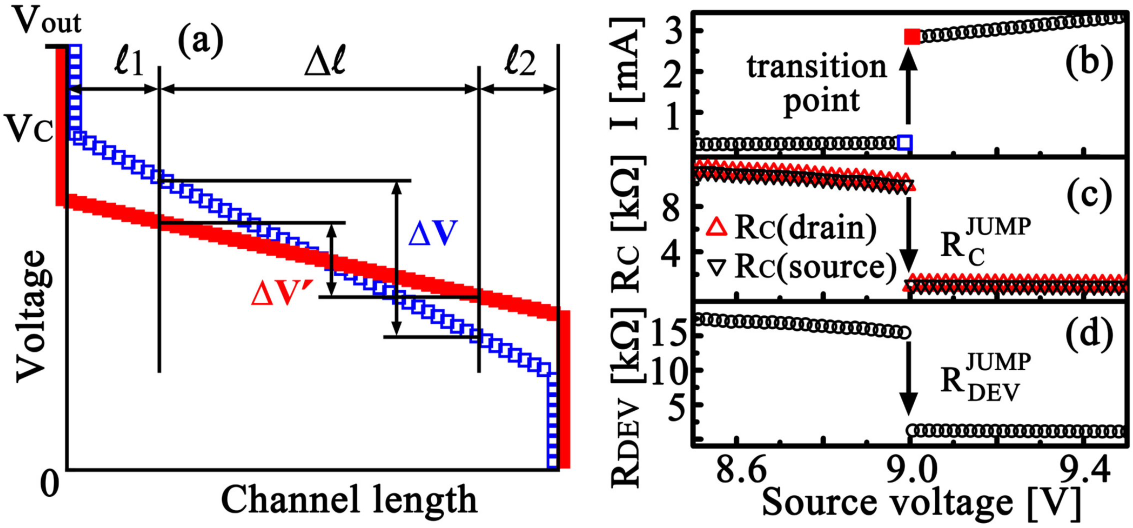

Figure 4.10 : (a) Schematic diagram of voltage distribution along the channel at a transition point (blue open squares) and right after transition (red closed squares). V_{C} denotes the voltage drop at the interfaces. (b) A fragment of I-V curve at 85 K in the vicinity of the transition. Blue open square marks the transition point and red closed square shows a point right after transition; blue and red squares in (a) correspond to the voltage distribution over the channel at these points. (c) and (d) are the voltage dependences of R_{C}(source), R_{C}(drain) and R_{DEV}, respectively, demonstrating the abrupt decreases (jumps) in all three resistances at the transition point.

Although V_{C}(source) and V_{C}(drain) increase, due to the overall increased current, R_{C}(source) and R_{C}(drain) actually *decrease* upon passing through the transition point. Fig. 4.10b,c, and d explicitly demonstrates these decreases (jumps) in R_{DEV} and R_{C} at a transition point, denoted further as R_{DEV}^{jump} and R_{C}^{jump}. For source and drain electrodes made of Cu, R_{C}(source) and R_{C}(drain) jumps at the transition point are equal to each other and remain unchanged in the experiments on exchanging the grounds.

Note that at the transition point *both* device and source and drain contact resistances decrease abruptly. This behavior is distinct from the one for other systems exhibiting voltage-driven transitions (such as manganites and doped $\mathrm{SrTiO_3}$). For these systems the leading role of oxygen vacancies drift under applied bias was demonstrated[83, 104], and source and drain contact resistances show variations of opposite sign [105]; *i.e.*, while source contact resistance increases, the drain contact resistance decreases. Since this is inconsistent with our observations, magnetite clearly must exhibit a different switching mechanism.

4.4.3 Temperature dependence of R_{C} and R_{DEV} jumps.

As temperature decreases, the jumps in contact resistance, R_{C}^{jump}, and device resistance, R_{DEV}^{jump}, remain negative, but increase in absolute magnitude (fig. 4.11a). Upon approaching the temperature when switching is not observed (T $\sim T_{\mathrm{V}}$ [10, 103]), R_{C}^{jump} and R_{DEV}^{jump} approach zero. The jump in ΔV is also temperature dependent and its magnitude exponentially decays with the temperature, approaching zero at T_{V}.

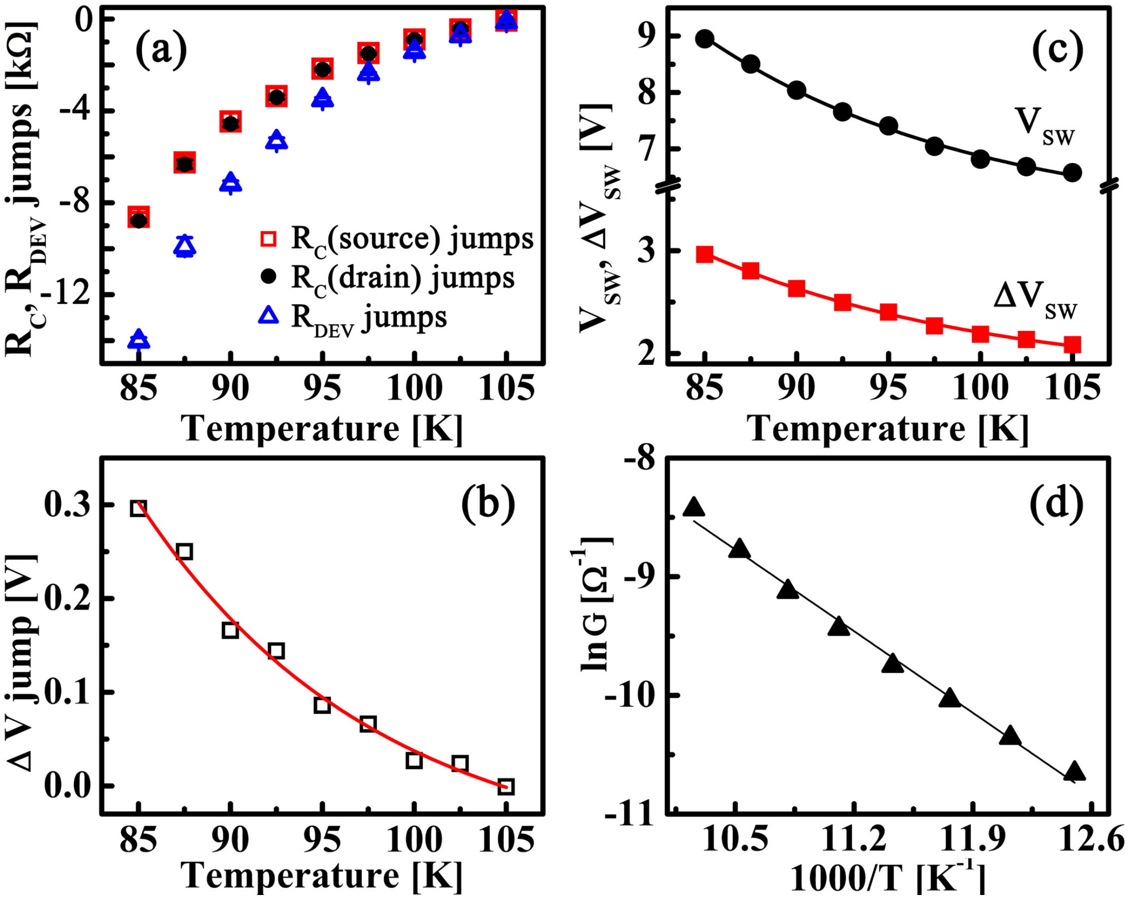

Figure 4.11 : Temperature dependences of (a) the jumps in R_C(source), R_C(drain) and in R_DEV at a transition point; each point represents an average over 8 independent measurements (left/right voltage pairs, different grounds, positive/negative switching voltages), standard deviation is within the symbol size (b) jumps in ΔV (squares) at a transition point and its exponential fit (solid line) (c) V_{sw} and ΔV_{sw} with corresponding exponential fits and (d) conduction ($1/R_\mathrm{DEV}$) of magnetite channel in Arrhenius coordinates and its linear fit.

V_{sw} and ΔV_{sw} depend on temperature exponentially as well, as demonstrated in fig. 4.11c.

The exponential dependences of the above parameters, particularly that shown in Fig. 4.11d, imply thermally activated transport below T_{V}. Indeed, plotting the inverse of R_{DEV} (in the Ohmic regime near zero bias) in Arrhenius coordinates gives a straight line in a given T range (Fig.4.11d). The activation energy, E_{a}, inferred from these data on the magnetite channel (device) lies in 85-89 meV range for several devices. These values match well with the size of the gap below T_{V}, inferred from photoemission [106, 107] and optical [108, 109] spectroscopies data. This suggests that transport below T_{V} involves charge carriers thermally activated over the gap.

4.4.4 Discussion

To explain the temperature dependence of the parameters related to the observed transition, *i.e.*, jumps in current, ΔV, R_{C} and R_{DEV} (Fig. 4.11), we should review the properties of magnetite below Verwey temperature, since the transition is only observed below T_{V}. We will consider the Verwey transition physics in magnetite from the electronic structure point of view. While magnetite has strong electron correlations, it is believed that a band-type description of its electronic structure is a reasonable approximation [110], with transport being dominated by low-lying electronic states near an effective Fermi energy, E_{F}.

The electronic structure of magnetite has been probed extensively by photoelectron and scanning tunneling spectroscopies and band-structure was calculated using different methods [106, 111, 68]. Above T_{V} there is a finite (non-zero) density of states (DOS) around E_{F}, which is dominated by Fe $3d$ states of the B-site sublattice of cubic structure. Below T_{V} the DOS near E_{F} exhibits a clear gap, causing two orders of magnitude increase in resistivity at T_{V} [106, 107].

Recently, it has been theoretically predicted that a gap to charged excitations (charge gap) in correlated insulators can be closed by applying external electric field, resulting in field-induced metal-insulator transition [112, 102]. Considering strongly electronically correlated system in nonequilibrium state under high electric field, Sugimoto *et al.* demonstrated, that metallic state is *energetically* favored if the electric field reaches a critical value, E_{sw}, which is lower than a Zener breakdown field [102]. Calculated I-E characteristics in the framework of this model resemble I-V curves observed in our magnetite experiments. Several systems exhibit this behavior, for example, charge-ordered state of complex manganese oxides [113, 82], as well as 1D cuprates [84] and 2D nickelates [114].

Our data on magnetite seem to be another experimental observation consistent with this sort of gap closure by electric field. The absence of hysteresis in forward and reverse bias sweeps, meaning that metallic state persists only if applied voltage (electric field) exceeds a critical value, $|V| > |V_{sw}|$, is expected from this mechanism and is indeed observed in $\mathrm{Fe_3O_4}$ (see Ref. [103] for details). The jump in $|R_{\mathrm{DEV}}|$ at the transition point is a natural consequence of the gap closure. The increase in the absolute value of $R_{\mathrm{DEV}}^{\mathrm{jump}}$ as T decreases (Fig. 4.11a) is also easily explained, as at lower temperatures there is a transition from more insulating state to the same metallic state with zero-size gap. Accompanying drops of contact resistances, R_C^{jump}, are direct consequences of gap closure and, thus, change in the position of magnetite E_{F} relative to the E_{F} of the contact metal.

4.5 Different source/drain contact metal devices

To further explore the $M/\mathrm{Fe_3O_4}$ interface properties, the effect of contact metals with various work functions is explored and results are discussed in this section. In the framework of the charge gap closure mechanism, the magnitude of contact resistance jumps at a transition point, R_{C}^{jump}, is expected to be dependent on the work function of the contact metal according to the relative alignment of E_{F} of the contact metal and the effective E_{F} of $\mathrm{Fe_3O_4}$. We systematically change the work function of the electrode metal, M, and have chosen 3 different contact metals: Cu, Au and Pt [ϕ(Cu)<ϕ(Au)<ϕ(Pt)] with Cu representing low- [ϕ(Cu)=4.65 eV], Au - medium- [ϕ(Au)=5.1 eV] and Pt - large- [ϕ(Pt)=5.65 eV] work function metals [115]. We trace the dependence of interface effects and their changes at a transition point as a function of contact metal work function, ϕ.

4.5.1 Pattern of devices. Fabrication details

We made a set of devices simultaneously incorporating two different contact metals (DCM) as source and drain electrodes: Cu-Au and Cu-Pt, as well as Au-Au and Pt-Pt devices on the same piece of magnetite wafer so that all junctions undergo the same fabrication steps. Fig. 4.12 illustrates the overall pattern containing six devices. Pairs of devices 1-6, 2-5 and 3-4 have a common pad (leading to source/drain electrode). This is designed to ensure as identical contact as possible of Cu (for devices 1 and 6), Au (for devices 2 and 5) and Pt (for devices 3 and 4), and assign the difference in behavior of mentioned pairs to the difference in ϕ of two other contacts (Pt and Au for devices 1 and 6; Au and Cu for devices 2 and 5; Pt and Cu for devices 3 and 4, see fig. 4.12).

The pattern (geometry) for each DCM device is the same as for regular (the same contact metals) four-terminal devices described in sec. 4.2, consisting of a pair of small-sized source/ drain leads (⌈ and ⌋ shape), two pair of voltage probe-wires and their small-sized leads, then small-sized leads are connected to medium-sized ones, which are attached to the large-sized leads and, in turns, to the 300 μm × 300 μm pads (see fig. 4.5c and d). In DCM devices, all parts, except for small-sized source/

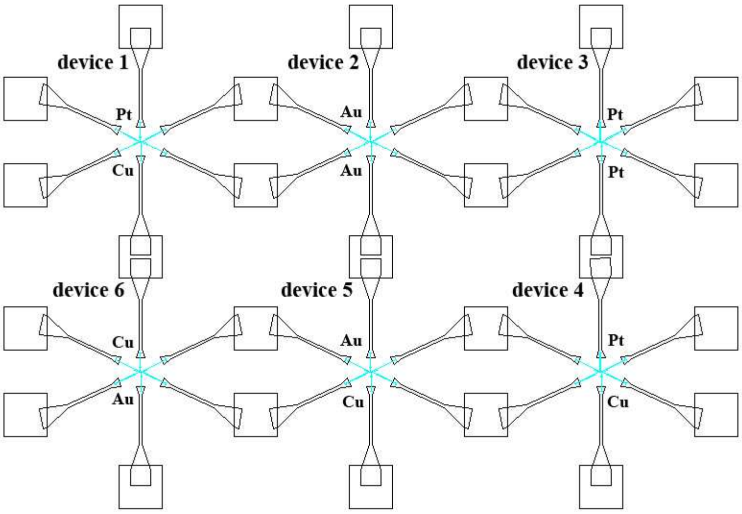

Figure 4.12 : The actual layout of different contact metal devices on the surface of Fe_3O_4.

drain leads, are made of 6 nm Cu adhesion layer and 10 nm Au cover layer (due to the best adhesion of Cu to the magnetite surface as discussed above in sec. 4.2). Only ⌈ and ⌋ source/drain leads are made of different metals: Cu, Au or Pt.

Fabrication of DCM devices on the same Fe_3O_4 film demanded two steps of e-beam lithography and three metal deposition steps. First, the whole pattern was defined by e-beam lithography except the only one or two small-sized source/drain leads (⌋ for devices 1, 4 and 5, ⌈ for device 6 and both ⌋ and ⌈ for devices 2 and 3, see. fig. 4.12) and 6 nm Cu/ 10 nm Au was deposited. This way the Cu contacts to devices 1, 4, 5 and 6 were made. Second, the remaining source/drain leads were patterned. An alignment with ≈100 nm precision is of need during the second lithography step and it was done by mean of two set of alignment marks. Then, devices 1, 3 and 4 were covered by Al foil and placed into evaporator for 20 nm Au deposition. After that the wafer was removed from the evaporator, devices 2, 5 and 6 were covered by Al foil and the wafer was put back into evaporator for, this time, 20 nm of Pt deposition. Only after these two deposition steps the lift-off process was performed. In result, devices 2, 5 and 6 contained Pt contact metals and devices 1, 3 and 4 - Au contact metals. Fig. 4.12 shows the device layout with the appropriate labeling of contact metals for each device.

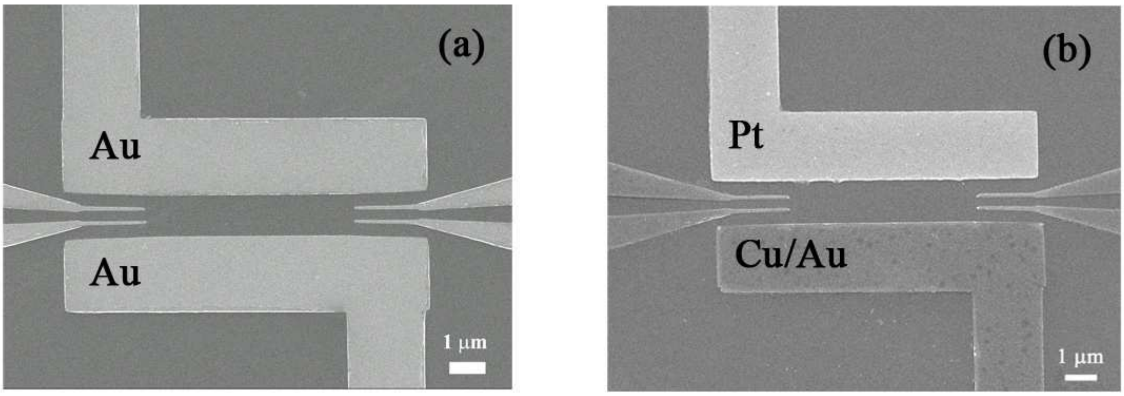

Figure 4.13 : SEM images of four-terminal devices with Au-Au (a) and Cu/Au-Pt (b) source-drain leads.

Representative SEM images of Au-Au and Cu-Au devices are shown in fig. 4.13. Thin gold wires were attached to the pads by In soldering and then to the pins of PPMS puck (fig. 4.5d-f in sec. 4.2). Electrical characterization of the devices was performed by standard four-terminal methods using a semiconductor parameter analyzer (HP 4155A) in PPMS in the same way as described in sec. 4.3 (see fig. 4.6a for circuit scheme).

Four independent measurements were conducted at a certain T for each four-terminal device with two pairs of voltage probes : left pair of V probes with one and then with the other contact electrode grounded; and the same different ground measurements using the right pair of V probes. Then, R_{C}(source), R_{DEV} and R_{C}(drain) were calculated according to the procedure described in sec. 4.3 for each measurement and values were compared with each other for data consistency. Namely, that calculations give the same values of R_{DEV}, R_{C}(source) and R_{C}(drain) for left and right pairs of voltage probes and that R_{C}(source) and R_{C}(drain) are switched upon exchanging the grounding options.

4.5.2 R_{C} dependence on contact metal

We first considered the behavior of the system before the transition. We made measurements in the linear I-V regime around 0 V (typically V sweeps from -1 V to 1 V) and calculated R_{DEV}, R_{C}(source) and R_{C}(drain) following the procedure described in sec. 4.3.

The same as for Cu-Cu devices described in sec. 4.4 $R_{\mathrm{C}}(\text{drain}) \approx R_{\mathrm{C}}(\text{source})$ for Au-Au and Pt-Pt devices (devices 2 and 3 in fig. 4.12). In contrast, DCM devices (Cu-Pt and Cu-Au) showed $R_{\mathrm{C}}(\text{drain}) \neq R_{\mathrm{C}}(\text{source})$; upon switching the grounds R_{C}(sourced) and R_{C}(drain) exchange their values.

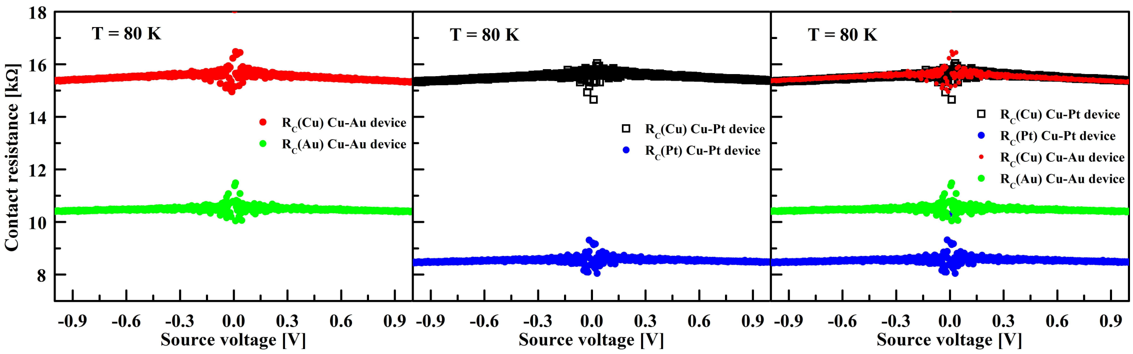

Figure 4.14 : Calculated R_{C} as a function of source voltage in linear I-V regime ($|V| < 1$ V, R=const) for (a) Cu-Au device and (b) Cu-Pt device. (c) superimposes graphs in (a) and (b) demonstrating R_{C} dependence on various contact metals: $R_{\mathrm{C}}(\mathrm{Pt}) < R_{\mathrm{C}}(\mathrm{Au}) < R_{\mathrm{C}}(\mathrm{Cu})$.

Fig. 4.14a and b demonstrate $R_{\mathrm{C}}(V_{out})$ dependence at T=80 K for Cu-Au and Cu-Pt devices, respectively, and fig. 4.14c superimposes $R_{\mathrm{C}}(V_{out})$ dependences from (a) and (b) to demonstrate, that $R_{\mathrm{C}}(\mathrm{Pt}) < R_{\mathrm{C}}(\mathrm{Au}) < R_{\mathrm{C}}(\mathrm{Cu})$. Note, that R_{C}(Cu) extracted from the independent measurements of Cu-Au and Cu-Pt devices is almost identical.

As fig. 4.15 demonstrates, $R_{\mathrm{C}}(\mathrm{Pt}) < R_{\mathrm{C}}(\mathrm{Au}) < R_{\mathrm{C}}(\mathrm{Cu})$ trend observed at T=80 K (fig. 4.14c) stands the same over a wider temperature interval below T_V. The error bars represent a standard deviation over all independent measurements of $R_\mathrm{C}(M)$ over all six devices (four measurements for each device, see sec. 4.5.1).

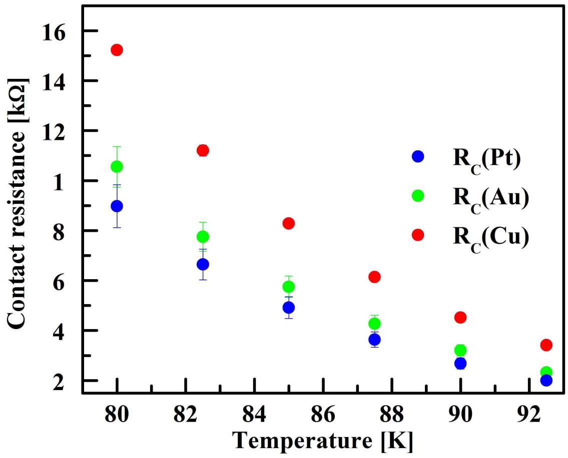

Figure 4.15 : Temperature dependences of contact resistances on various contact electrodes (Cu, Au and Pt).

To explain the observed trend we consider the properties of the electrode/Fe_3O_4 interface. The contact resistance of the electrode/Fe_3O_4 interface, *i.e.*, M/Insulator (semiconductor) interface, most likely originates from the offset between the metal Fermi level and the states responsible for transport in the magnetite. This offset is defined by the difference in the work function, ϕ, of a contact metal M and Fe_3O_4. The work function of bulk magnetite is $\phi_{bulk}(Fe_3O_4)$=5.78 eV. While $\phi(Fe_3O_4)$ of the (100) film on W(100) single crystal is measured by the cutoff of the photoelectron spectra and is equal to $\phi_{film}(Fe_3O_4)$=5.20±0.15 eV (reduction of ϕ indicates a decrease of the dipole moment induced on the surface) [116]. Thus, Fe_3O_4/Cu and Fe_3O_4/Au contacts are the ones with $\phi(Fe_3O_4) > \phi(M)$. $R_\mathrm{C}(T)$ dependence for devices with Pt contacts is qualitatively the same as the one for Cu and Au devices (fig. 4.15). Therefore, it is likely that the "nature" of the contact [*i.e.*, $\phi(Fe_3O_4) > \phi(M)$] is the same for all three metals; and that either ϕ of polycrystalline Pt foil is lower than the bulk value of ϕ_{bulk}(Pt)=5.65 eV or the effective E_F of Fe_3O_4 film on MgO substrate is higher than the one measured in literature at ~300 K (~5.2 eV) for (100) films on W (100) substrate.

Below T_V the charge carriers in Fe_3O_4 are holes (though the conductance value is very low). That is, Fe_3O_4 might be modeled as a p-type semiconductor (s/c) [117, 118]. The energy-band diagram for M/p-type s/c interface with $\phi(p\text{-type s/c}) > \phi(M)$ is schematically shown in fig. 4.16. The height of the Schottky barrier, $q\phi_b$ is defined by equation:

$$e\phi_b = E_g - q[\phi(M) - \chi] = E_g + q\chi - q\phi(M) \tag{4.1}$$

where E_g and χ are a band gap and an electron affinity of a semiconductor, respectively, and q is an electron charge ($q > 0$) [14]. According to eq. 4.1 $e\phi$ is inversely proportional to the work function of the metal in contact, $\phi(M)$: the heigher $\phi(M)$ is the lower $e\phi_b$ and, thus, R_C of the contact interface is.

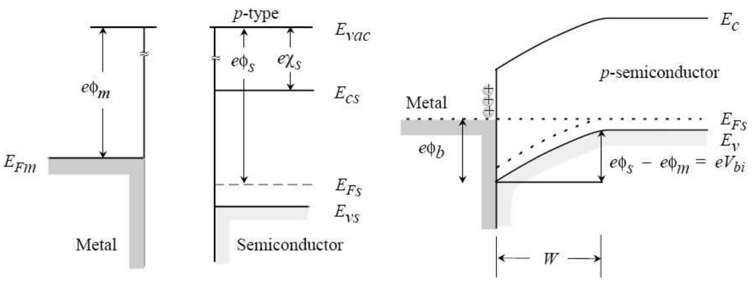

Figure 4.16 : Energy band diagram of M and p-type semiconductor, ϕ(s/c)> $\phi(M)$] ([14]).

Therefore, experimentally observed increase in R_C: R_C(Pt)< R_C(Au)< R_C(Cu) as ϕ of the contact M decreases: R_C(Pt)< R_C(Au)< R_C(Cu) is in agreement with the increase in the Schottky barrier height as $\phi(M)$ decreases (fig. 4.15). Thus, the behavior of the Fe_3O_4 under mild disturbing conditions (low sourced voltage, close to equilibrium) can be satisfactory described by Schottky barrier formation model.

4.5.3 Dependence of R_{C} jumps on contact metal

Now let us consider R_{C} behavior in the non-equilibrium, on the onset of the EFD transition. First of all, the EFD transition is observed for both low- and high-work function metals (4.65 eV - 5.65 eV range for Cu, Au and Pt). Besides, we were able to observe reproducible EFD switching in devices with the contacts made of Fe, Ti and Al, which have even lower ϕs of 4.5 eV, 4.33 eV and 4.28 eV [115], respectively. (see Chapter 5 for detailed experiments on Ti/Fe_3O_4 junctions).

For RS systems known in literature, for which the origin of RS is attributed to the change in Schottky barrier height (or width) by trapped charge carriers at the interface states, the switching is observed only if contact metal forms a rectifying contact with the oxide material. That is, p-type materials [such as complex manganite $Re_{0.7}A_{0.3}MnO_3$ ($Re =$ Pr, La; $A =$ Ca, Sr)] exhibit RS with low work-function, metals, M=Mg, Al and Ti, and does not show RS with high work function metals such as Au and Pt [119]. On the other hand, n-type materials (Nb or Cr doped $SrTiO_3$) demonstrate RS only when electrodes are made of high ϕ material, such as Au or $SrTiO_3$ [12].

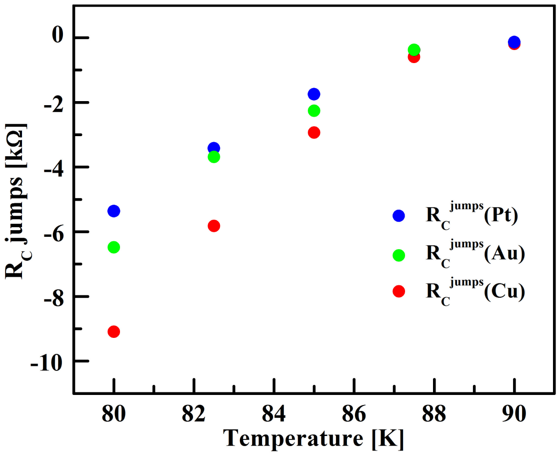

Figure 4.17 : Temperature dependences of jumps in contact resistances, R_{C}^{jump}, at a transition point on various contact electrodes (Cu, Au and Pt).

The fact that transition in magnetite is observed both with low- and high- ϕ contact metals again supports a different switching mechanism in Fe_3O_4. Calculated jumps in contact resistance, R_{C}^{jump}, at a transition point for Cu, Au and Pt are shown in fig. 4.17. The absolute values of the jumps for Cu contacts are higher than the ones for Au and Pt at all temperatures: $|R_{\mathrm{C}}^{jump}(\mathrm{Cu})| > |R_{\mathrm{C}}^{jump}(\mathrm{Au})| > |R_{\mathrm{C}}^{jump}(\mathrm{Pt})|$.

In the assumption of the Schottky-like barrier formation at $M/\mathrm{Fe_3O_4}$ interface and in the framework of charge gap closure mechanism, the jumps in resistance is caused the change in relative position of E_{F} of Fe_3O_4 and of E_{F} of the contact metal. That is effectively overcoming the barrier $e\phi$ in eq. 4.1 and, therefore, R_{C}^{jump}s should have the same dependence on ϕ of the metal as R_{C} as indeed is observed experimentally (fig. 4.17). The latter proves that charge gap closure by electric field is a valid origin of the resistance switching in magnetite system.

4.6 Conclusions

In conclusion, by doing four-terminal experiments at magnetite thin films below T_{V} we quantitatively separate the contributions of each electrode and the magnetite channel before and after EFD transition. For devices of increasing channel lengths we demonstrate the increase in total resistance to be caused by increased contribution of the magnetite channel, while contact resistances are unchanged for all channel lengths within 1 to 2 μm range. At all temperatures the transition is observed ($T < T_{\mathrm{V}}$), contact resistances of *both* source and drain electrodes and the resistance of magnetite channel decrease abruptly at the transition point. Temperature dependent electrical measurements below the Verwey temperature indicate thermally activated transport over the charge gap. The behavior of the magnetite system at a transition point is consistent with a theoretically predicted transition mechanism of charge gap closure by electric field [112, 102].

To further support charge gap closure mechanism we investigated devices with the contacts made of metals with various work functions, ϕ (Cu, Au and Pt). We demonstrate that experimentally observed dependence of contact resistance: R_{C}(Pt)< R_{C}(Au)< R_{C}(Cu) while ϕ(Pt)> ϕ(Au)> ϕ(Cu) is in agreement with the Schottky barrier formation at the metal/p-type semiconductor ($\mathrm{Fe_3O_4}$ below T_V) interface with ϕ(p-type s/c)> $\phi(M)$. Jumps in contact resistances at a transition point, R_{C}^{jump}, are also ϕ-dependent and evolve with ϕ as is predicted in charge gap closure mechanism. Namely, as ϕ of contact metals increases the jumps due to the gap collapse decrease: R_{C}^{jump}(Cu)> R_{C}^{jump}(Au)> R_{C}^{jump}(Pt).

Chapter 5

Switching field distributions and their dependence on magnetic field

5.1 Introduction

As was mentioned briefly in sec. 3.3.1 the switching voltage, V_{sw}, was noticed to fluctuate in repeating *I*-*V* cycles (*i.e.* there is a sweep-to-sweep variability in V_{sw} positions), meaning that there is a certain voltage range, not a single V_{sw} value, in which the transition to On state can be induced. The magnitude of fluctuations (the range of V_{sw} values) varies with temperature, becoming larger at lower temperatures.

A similar fluctuation of switching parameters over repeating switching cycles is known in literature for several different systems. First, superconducting nanowires (such as $Mo_{79}Ge_{21}$) exhibit a transition from superconducting (SC) state to a state with a finite resistance (resistive, normal state) if applied current exceeds a critical value, I_{sw} (fig. 5.1a). I_{sw} distributions broaden as T is lowered (fig. 5.1b) [15]. The driving force for switching from the SC state to the resistive state is a formation of a single or multiple phase slip(s) which heat the wire. The broadening of the I_{sw} distributions is successfully explained in a runaway overheating model [120, 15].

The second relevant system is magnetic amorphous microwires ($Co_{68}Mn_7Si_{15}B_{10}$ [121]) which undergo a magnetization reversal process (a transition between two stable magnetic states) as the applied external magnetic field reaches a threshold value, H_{sw}. The width of H_{SW} distributions also increases as temperature decreases, and this broadening is modeled in thermoactivated model with the basic principle that

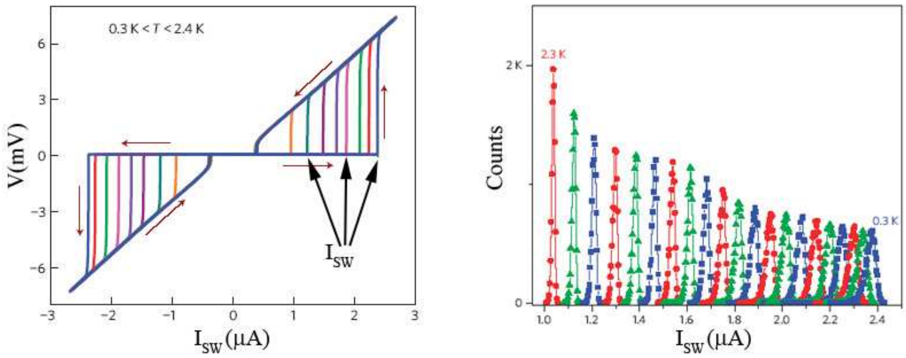

Figure 5.1 : (a) V vs. I dependence at various temperatures from 2.3 to 0.3 K. The switching currents, I_{SW}, are indicated for the data taken at 0.3, 1.2 and 2.1 K. The temperatures are T=0.3 (the highest I_{SW}), 0.6, 0.9, 1.2, 1.5, 1.8, 2.1, 2.4 K. (b) I_{SW} distributions for temperatures between 0.3 K (right-most) and 2.3 K (left-most) with ΔT=0.1 K (adapted from [15]).

the total free energy of the closure domain wall (which depinning and propagation govern the magnetization reversal process) is field- and temperature-dependent [121].

At the same time for RS systems the distributions of V_{sw}, E_{sw} or I_{sw} are poorly addressed both experimentally and theoretically. The most common statistical experiment in RS systems is a "memory" test, which is "set-read-reset-read" test. In this test (1) a single voltage pulse $V >_{set}$ is applied to drive the system into the On state; (2) small V$_{read}$ pulse is sent and current is measured to "read" (verify) the On state of the system; (3) $V > V_{reset}$ pulse is sent to drive the system into the Off state; (3) the same small V$_{read}$ pulse is sent and current is measured to "read" the Off state of the system. Depending on the type of RS system V_{set} and V_{reset} might be of the same polarity, but of the different magnitude: $|V_{set}| > |V_{reset}|$ (unipolar RS); or of the same amplitude, but of the opposite signs (bipolar RS) (sec. 1.3, fig. 1.10). The (1)-(4) cycle is repeated thousands and thousands of times to test the memory characteristics of the system. But this test is intended to just probe the state of the system (On or Off), while the reproducibility of the exact V_{set} value is not addressed. Besides, most RS systems are tested only around room temperature, without investigation over wide temperature range.

V_{sw} distribution and its evolution with temperature might give an insight into the switching mechanism, as it does for superconducting and magnetic nanowire systems mentioned above. In this part we perform detailed V_{sw} experiments at various temperatures in magnetite system with and without application of external out-of-plain magnetic field. We discover an interesting (and counter-intuitive) temperature dependence of V_{sw} distribution width: it increases as temperature decreases. Besides, magnetic field has an effect both on mean V_{sw} position and the width of V_{sw} distribution.

5.2 Experimental procedures

The distribution of V_{sw} was obtained by executing several thousand consecutive forward pulsed I-V sweeps in the vicinity of the transition point (typically 0.2-0.3 V range) at a fixed temperature and recording V_{sw} positions at each sweep.

We used devices with the smallest gap size possible to minimize the value of V_{sw}. Large channel devices ($L > 100$ nm) tended to change the gap size over numerous switching cycles and had distorted shape of V_{sw} histograms. Devices with gaps, produced "Cr HAR method" (see section 2.2 for fabrication steps) showed stable behavior. Typical gap sizes for investigated devices were 10-30 nm (see fig. 5.2 a for an example of SEM image).

The voltage was always applied in a pulsed regime with 500 μs width and 5 ms period to minimize the heating of the channel. In a typical experiment with these pulse parameters $V_{sw}^{On} \neq V_{sw}^{Off}$, but only V_{sw}^{On} is of interest in this set of experiments. Thus, only forward and no reverse I-V sweeps (to detect V_{sw}^{Off}) were done.

In contrast to continuous (staircase) regime, where the only single switching event happens, in pulsed regime either one (fig. 5.2 b) or several (fig. 5.2 c) switching events occur. This is because in a continuous voltage sweep, once the system is switched to On state, high current raises the local T of the channel, and upon application of consequent higher voltages, the system stays in On state.

As was discussed in details in sec. 3, in pulsed regime the channel has a chance to cool down between application of pulses. Thus, even if the system is switched to On state once at $V_{sw}(1)$ it may cool down between pulses and upon application of V>$V_{sw}(1)$ appear to be in Off state again, and then switched to On state at some higher voltage, $V_{sw}(2)$ and so on. Fig. 5.2b and c show two examples of *I*-*V* curve fragments with a single and multiple switching events.

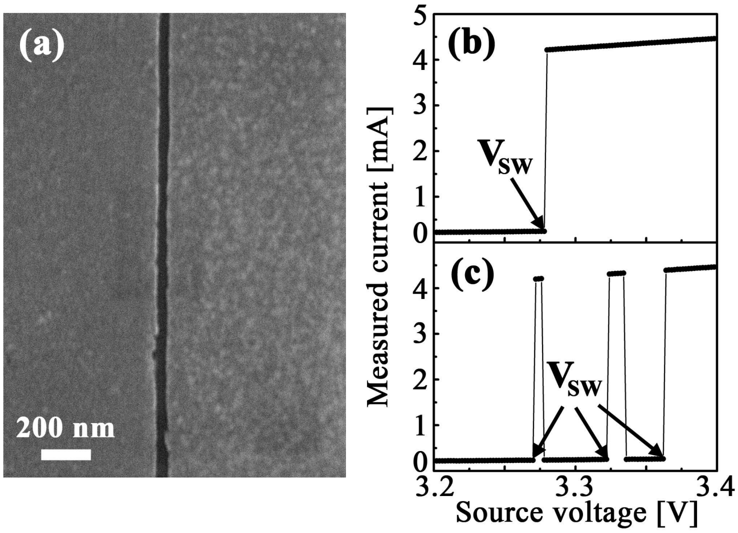

Figure 5.2 : Details of V_{sw} distribution experiment. (a) Typical SEM image of Ti/Au electrodes, patterned on magnetite film surface, separated by nanogap < 100 nm. (b) and (c) are the fragments of *I*-*V* curves in the vicinity of a transition (the V range, where switching is observed) demonstrating one (b) and three (c) switching events in a single *I*-*V* cycle.

Since V_{sw} distribution experiments were mainly conducted in conjunction with magnetic field (see below) experiments, only non-magnetic contact electrodes were used (either pure gold or Ti/Au contacts) to eliminated the possible influence of magnetic contacts on the outcome results.

The V_{sw} distribution at a certain temperature is built by recording all switching events over several thousands (3000-6000) I-V cycles and then counting the number of switchings at a certain V_{sw}, thus giving a number of counts vs V_{sw} histogram. An example of V_{sw} distribution at 90K is shown in fig. 5.3a. The distribution is a single peak, symmetrical around the most probable V_{sw} value. Some measured devices show an asymmetric distribution shape (fig. 5.3 b) or clearly display two peaks (fig. 5.3 c), which we attribute to the instability of the physical gap size during the measurement procedure. These devices are considered unsuccessful and are not taken into consideration.

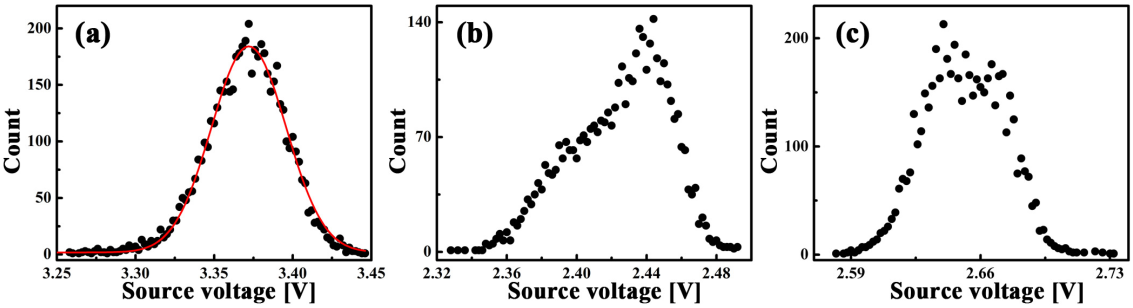

Figure 5.3 : Examples of V_{sw} distribution histograms. (a) Successful experiment with symmetric single peak. The red line is a guide for the eyes only. (b) and (c) show asymmetric peak and double peak histograms, respectively, typical for devices with unstable gap sizes.

The procedure of V_{sw} distribution collection was repeated at each temperature the transition was observed down to $\sim$ 75K. The measurements below 75K usually resulted in asymmetric V_{sw} histograms due to increased absolute mean value of V_{sw} and, thus, higher chance to degrade the gap size with repeating cycles. It is worth mentioning that at lower temperatures I-V cycles with multiple V_{sw} events (fig. 5.2c) were observed more frequently than the ones at higher temperatures. Thus, the total number of switching events varied from temperature to temperature, even though the number of I-V cycles at each temperature was kept the same. Therefore, for the sake of comparison of V_{sw} distributions at different temperatures, V_{sw} distributions were normalized, *i.e.*, plotted as $\frac{\#of counts}{max\#of counts}$ vs V_{sw}, where "max # of counts" is the number of counts at the most probable V_{sw} and "# of counts" is a number of counts at a certain V_{sw}. Fig. 5.4 demonstrate an example of normalized V_{sw} distributions in the 77 K - 105 K temperature range.

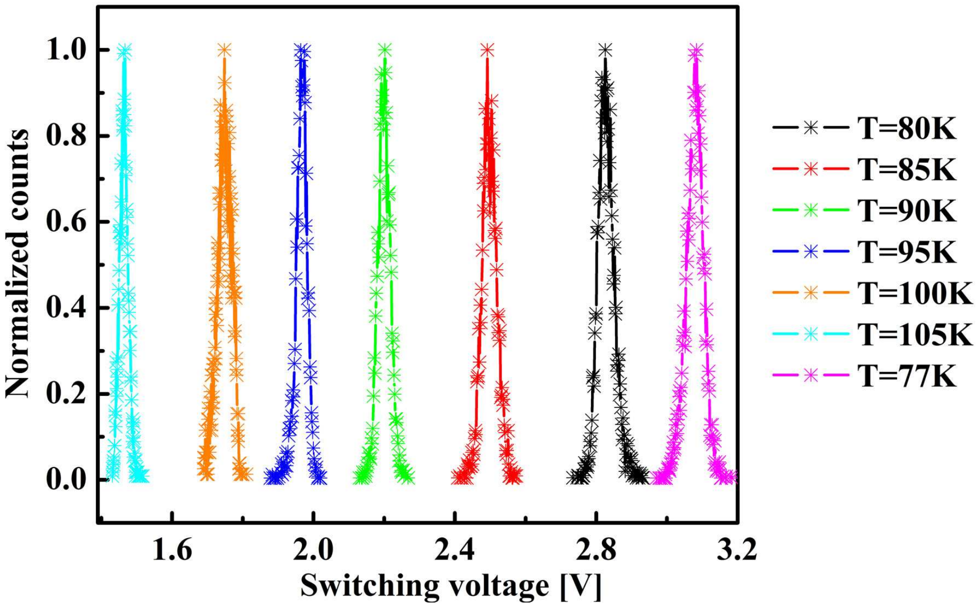

Figure 5.4 : Normalized V_{sw} distribution histograms at different temperatures (77 K - 105 K). The width of distributions increases as temperature decreases.

To perform magnetoresistance measurements the puck with devices attached was placed into the PPMS and magnetic field was swept continuously in the direction perpendicular to the film plane (out-of-plain), while either sweeping (0 - 100 mV range) or sampling (single V_{out}=100 mV) the voltage, simultaneously measuring the current. $R(H)$ is calculated as V/I and magnetoresistance value at a certain magnetic field as $MR(H) = \frac{R(H)-R(H=0T)}{R(H=0T)}$.

5.3 Temperature dependence of V_{sw} distribution width

The V_{sw} distribution at each temperature is characterized by two main parameters. First, the mean switching value $\bar{V}_{sw} = \frac{\sum_{i=1}^{n} V_{sw,i}}{n}$, where n is the total number of switching events. Second, the width of distribution, calculated as a standard deviation: $\sigma(V_{sw}, T) = \sqrt{\frac{\sum_{i=1}^{n}(V_{sw,i} - \bar{V}_{sw})^2}{n-1}}$. As expected, the $\bar{V}_{sw}(T)$ follows the same descending dependence on temperature as $V_{sw}(T)$ dependence in single I-V experiments described in earlier chapters (see fig. 5.5a and fig. 3.5b in sec. 3.3 for temperature dependence of V_{sw}). More interesting is $\sigma(V_{sw}, T)$ dependence, which demonstrates broadening of V_{sw} distribution (higher σ values) as the temperature decreases (fig. 5.5). There is a deviation from monotonous temperature dependence at 100 K reproducible for several devices tested. There is an anomaly of several physical parameters, such as resistance, heat capacity and magnetoresistance value, occurring at T_V, but for these devices T_V is ∼110K (see inset in fig. 5.5a), which is higher than 100 K. We do not know so far how to explain the observed anomaly in $\sigma(V_{sw}, T)$ at 100 K.

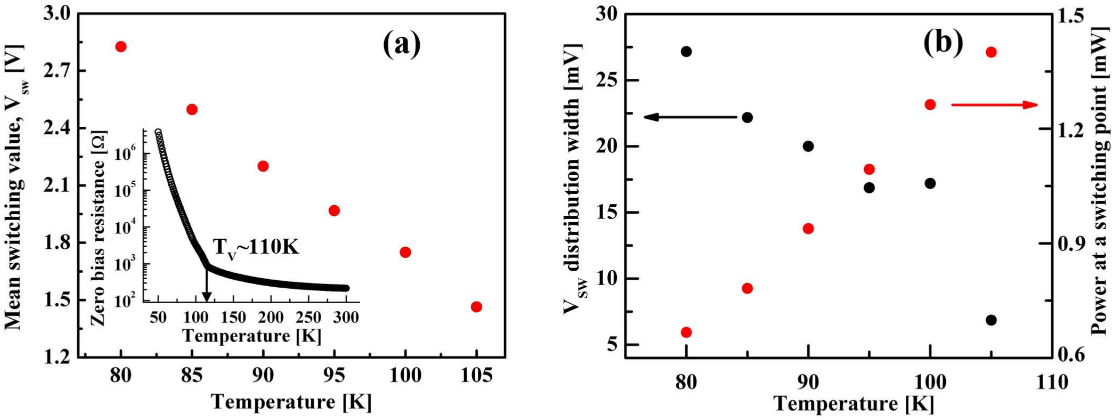

Figure 5.5 : (a) Temperature dependence of $\bar{V}_{sw}$ showing descending dependence on temperature. Inset shows zero-bias R vs T plot demonstrating T_V 110 K.(b) Temperature dependence of V_{sw} distribution width, $\sigma(V_{sw}, T)$ (black circles), and power at a transition point (red circles).

This increase in $\sigma(V_{sw})$ as temperature decreases is rather counter-intuitive. Indeed, one might expect "freezing" of temperature fluctuations and decrease in thermal noise as the set temperature, T_{set}, of the experiment decreases and, thus, narrowing of V_{sw} distributions. T_{set} may not be an accurate reference point, since the *local* temperature of the channel, T_{local}, at a transition point is the one of the main importance for this experiment. But, as was discussed in detail in the introduction (sec. 1.2.4), T_{local} is defined by the power dissipated at a transition point, P_{sw}, and it decreases as T_{set} goes down (fig. 1.8a and 3.9a). Fig. 5.5b shows temperature dependences of $\sigma(V_{sw})$ and the power at a transition point, P_{sw}, for the same device clearly demonstrating the opposite trend with temperature. Thus, the origin of $\sigma(V_{sw})$ broadening does not originate from the thermal fluctuations (noise).

To get more information about system behavior we made V_{sw} distribution experiments in the presence of magnetic field.

5.4 Magnetic field effect

Our first experiments on addressing the effect of magnetic field on the transition showed no evident change in the behavior of the system in the presence of out-of-plane magnetic field. Specifically, we have done two-terminal I-V measurements at a certain temperature with and without application of magnetic field (up to 7 T). Resulting I-V curves looked almost identical, with the only slight difference in V_{sw} position, which seemed to be within the sweep-to-sweep variations in V_{sw} values discussed in the above subsection.

But, more detailed (statistical) V_{sw} distribution experiments in magnetic field showed clear dependence of both $\bar{V}_{sw}$ and $\sigma(V_{sw})$ on the magnitude of out-of-plane magnetic field, H. V_{sw} distributions (3000 cycles each) were collected consecutively at 12 magnetic field values:

0 T (first) → 0.2 T → 0.4 T → 0.6 T → 0.8 T → 1 T → 2 T → 3 T → 4 T → 5 T
→ 6 T → 0 T(last).

Fig. 5.6a shows resultant V_{sw} distributions at 80 K at several selected magnetic fields. As can be seen, magnetic field shifts V_{sw} peak to higher V values and narrows V_{sw} distributions. To reassure that the observed $\bar{V}_{sw}$ right shift is not related to the degradation (increase in) of the gap size, the control distribution experiment at H=0 T (3000 cycles) was performed after experiments in all non-zero magnetic fields. V_{sw} distributions at H=0 T in the beginning [H=0 T (first)] and in the end [H=0 T (last)] are identical (see fig. 5.6), meaning that observed changes in V_{sw} distributions (shift and narrowing) are indeed caused by applied magnetic field.

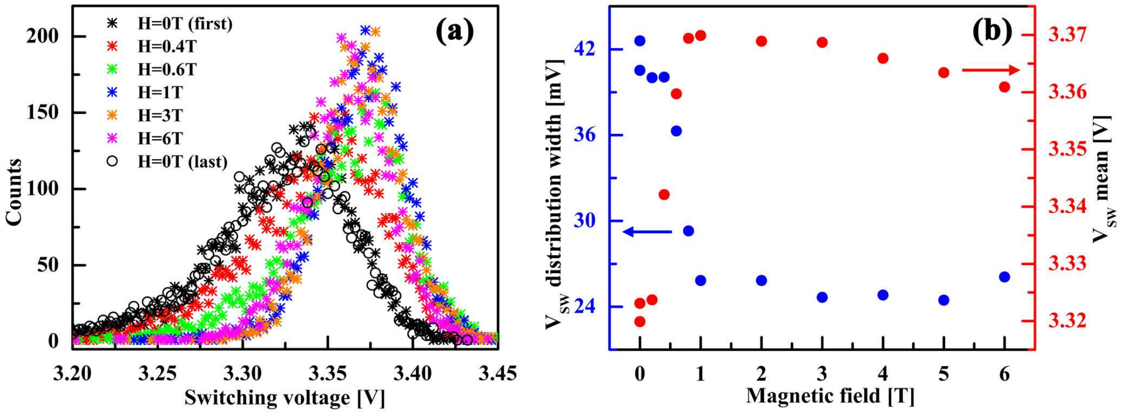

Figure 5.6 : (a) Examples of V_{sw} distributions at selected magnetic fields (T=80K).(b) Magnetic field dependence of the mean switching value, $\bar{V}_{SW}$ (red circles), and the width of V$_{sw}$ distributions, $\sigma(V_{sw})$ (blue circles).

Fig. 5.6b quantitatively demonstrates the mean switching value $\bar{V}_{sw}$ and $\sigma(V_{sw}, T)$ dependence on applied magnetic fields (all 12 H values) clearly showing an opposite effect of H to $\bar{V}_{sw}$ and $\sigma(V_{sw}, T)$: while $\bar{V}_{sw}$ increases, $\sigma(V_{sw}, T)$ decreases as H goes up. Both parameters, though, saturate at about 1 T, *i.e.*, further increase of the magnetic field up to 6 T effectively has no influence to $\bar{V}_{sw}$ and $\sigma(V_{sw}, T)$ (fig. 5.6b).

It is worth mentioning, that in the V_{sw} distribution experiments when H applied in the following sequence:

$$-6\text{ T} \rightarrow -4\text{ T} \rightarrow -2\text{ T} \rightarrow 0\text{ T} \rightarrow 2\text{ T} \rightarrow 4\text{ T} \rightarrow 6\text{ T} \rightarrow 0\text{T}.$$

Magnetic field of the opposite sign has exactly the same effect on the position and the width of V_{sw} peak (fig. 5.7) Besides, the order of H application does not matter as well.

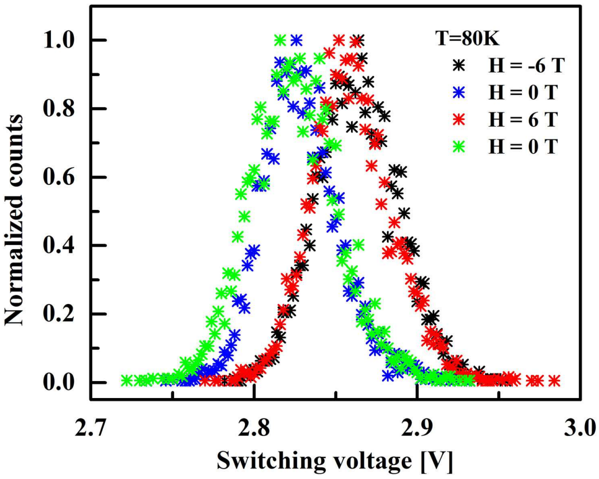

Figure 5.7 : Demonstration that $\bar{V}_{sw}$ and $\sigma(V_{sw})$ do not depend on the polarity of the magnetic field applied.

As we pointed out several times in this work, V_{sw} scales linearly with the channel length, L, (fig. 1.8c and 3.9b) *i.e.*, V_{sw} increases and L increases. Clearly as L increases, the resistance of the channel increases as well ($R \sim L$). One would imagine that the right shift of the $\bar{V}_{sw}$ might be related to the increases of R as the magnetic field is applied in a similar way. But it is known that Fe_3O_4 displays a negative magnetoresistance (MR) [122, 123], that is, R decreases as H is applied.

Our magnetoresistance data on the same devices, we made V_{sw} distribution experiments, also displays negative MR. Two examples (T=75 K and 105 K) of normalized resistance $[R/R(H=0T)]$ vs. H plots are shown in fig. 5.8. As can be seen, the resistance remains effectively unchanged up to ~0.4 T and ~0.2 T at 75 K and 105 K, respectively, and then gradually goes down as $|H|$ increases. Thus, when $\bar{V}_{sw}$ and $\sigma(V_{sw})$ experience the main changes upon H application ($H < 1T$, see fig. 5.6), resistance of the device either stays constant or decreases. On the other hand, in H range when R experiences significant changes (decreases, see fig. 5.8), $\bar{V}_{sw}$ and $\sigma(V_{sw})$ remain unchanged (fig. 5.6b). Therefore, the shift of $\bar{V}_{sw}$ in the presence of H cannot be explained as a simple consequence of a change in the resistance value.

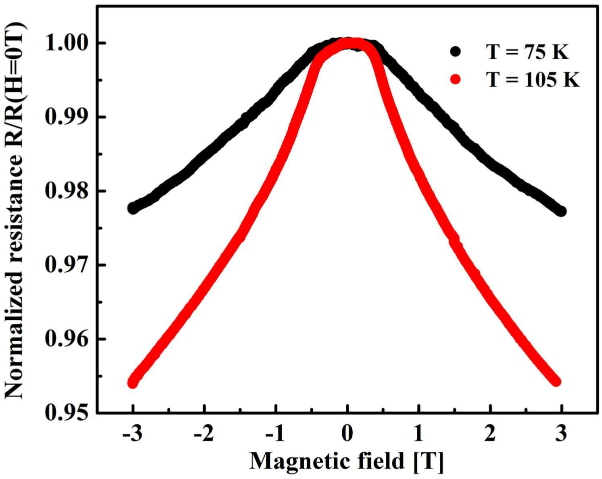

Figure 5.8 : Magnetoresistance data at 75 K and 105 K. Dependence of normalized resistance $(R/R(H=0T))$ on the magnetic field applied.

5.5 Discussion. Conclusions.

We have demonstrated above that $\sigma(V_{sw}, T)$ behavior is inconsistent with the thermal issue and $\bar{V}_{sw}$ shift in magnetic field does not relate to the change in R of the channel. In general, our experiment can be considered as an example of the case of a system being driven out of equilibrium by an external perturbation, such as electric or magnetic fields, or dc current. External perturbation changes free energy of the system, effectively lowering the potential well or altering the relative positions of local minima, thus making one or the other state more energetically favorable. This problem was generally addressed by A. Garg [124]. He considers the effective free energy for the system as a whole that (a) has two minima (or a minimum and an unbounded decrease); (b) evolves with T, so that at some critical temperature one minimum becomes lower than the other (this is the case of a first-order phase transition driven by temperature); (c) is tilted by the application of an external field.

So, the system stays in its thermodynamic ground state (the lower free energy minimum). As the external field is applied, the free energy tilts so that the other minimum is pulled down. In “equilibrium”, once the second minimum becomes lower than the first minimum, the system makes a transition to its new ground state. However, we are concerned with the kinetics of the process. What happens when the barrier gets sufficiently low is that fluctuations can drive the system over the barrier, this is called by Gang “escape from the well”. Generally, at higher T there are more fluctuations, so one might expect a broader distribution of switching fields that would sharpen up to approach the critical (barrier goes away completely) switching field as T decreases. It is complicated, though. As T decreases, thermal fluctuations go down, but the barrier itself becomes higher and broader. It’s also possible that disorder can mean that the actual free energy is somewhat rough and bumpy. At high T, one might be able to ignore those bumps, but local minima may be important at low T.

It is worth mentioning once again that at least two other physical systems (superconducting (SC) and anisotropic magnetic wires) demonstrate the broadening of the distribution of switching parameters (switching current, I_{sw}, in SC wires and switching magnetic field, H_{sw}, in magnetic wires) as temperature decreases (see sec. 5.1).

The mean and width of the escape-field distribution was also theoretically considered by A. Garg [124]. In this model the mean field value (in our case equivalent to E_{sw} or V_{sw}) versus the width of the escape-field distribution (in our case $\sigma(V_{sw})$) should be a straight line [124]. Plotting our experimental data as V_{sw} vs. $\sigma(V_{sw})$ at temperatures, the EFD transition is observed, at $H = 0T$ indeed demonstrates nearly linear dependence (except the 100 K data point which also shows inconsistent $\sigma(V_{sw})$ value) (fig. 5.9). Thus, escape-field model might be appropriate to describe our data.

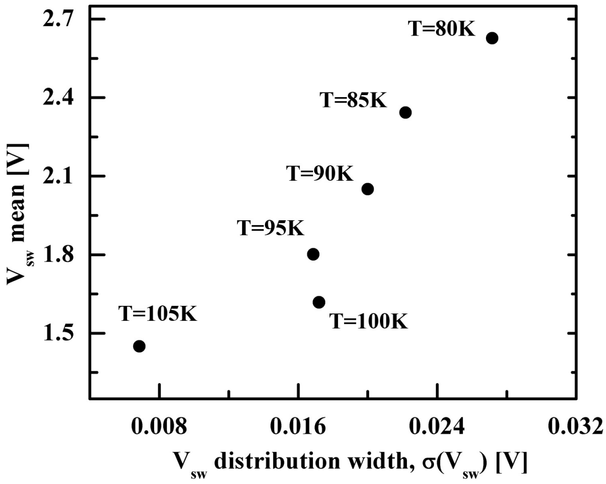

Figure 5.9 : Demonstration, that plotting $\sigma(V_{sw})$ versus $\bar{V}_{sw}$ results almost in straight line. Each point represent a certain temperature with the appropriate T label placed next to the point.

In our case, the Verwey insulating state below T_V is the initial condition. At sufficiently large electric fields, the electronic system could lower its energy by allowing charge to fall down the electrostatic potential. There is a barrier to this, though: the gap at the Fermi level to creating charged excitations. The kinetics of getting over this gap are being probed by these histogram experiments. One can imagine thermal activation over the barrier (thermally excited charge carriers are able to start flowing, leading to self-heating and lowering of the barrier, like in the SC case above). One can imagine quantum tunneling through the barrier (this is the Landau-Zener breakdown proposed by Sugimoto *et al.* in ref. [102]).

The hope, and we are collaborating currently with theorists on this, is to examine the T dependence of our data and see if we can determine consistently the mechanism of the EFD in our magnetite system.

The dependence of the histograms on the magnetic field is important for one major reason. Over the field range of interest, the external field is affecting d-orbitals in the material, both in the bulk and at the (disordered) surface. The fact that H affects the kinetics further supports the idea that we really observe electric-field driven charge gap closure. In particular, if the orbital ordering picture of Piekarz et al. [50] is right for the Verwey groundstate, then it makes sense that coercing the orbitals should affect the EFD transition. The charge gap should depend on what the d-orbitals are doing in detail. If the EFD transition were something else unrelated to the charge gap, then one would not expect a magnetic field to have an effect.

In conclusions, we have found out that the switching voltage, V_{sw} at a certain T is not a single value, but rather varies from sweep to sweep forming a certain range of voltages in which the transition can be induced. The distribution histogram of V_{sw} forms a well-defined peak symmetrical around the most probable V_{sw} value. We first explored the temperature dependence of the mean, $\bar{V}_{sw}$, and the width, $\sigma(V_{sw})$, of V_{sw} distribution. Both parameters increase as temperature decreases.

Secondly, we performed V_{sw} distribution experiments in the presence of out-of-plain magnetic field. The results showed that magnetic field up to ~1 T has an effect on the V_{sw} distributions. Namely, H left shifts and narrows V_{sw} distribution peak. For $H > 1T$ both $\bar{V}_{sw}$ and $\sigma(V_{sw})$ saturate and remain unchanged as H is swept up to 6T. The stochasticity of V_{sw} is again consistent with the charge gap closure mechanism of EFD transition in magnetite. Quantitative modelling of $\sigma(V_{sw})$ dependence on T and $\bar{V}_{sw}$ and $\sigma(V_{sw})$ dependences on H is currently under way by our collaborators.

Final remarks and future directions

In this thesis, we investigated electric field driven (EFD) transition in magnetite. This exciting phenomenon has remained obscured for 70 years of Fe_3O_4 intense investigations and was just discovered in our laboratory 4 years ago. There is no direct analogy to this transition in literature; experimental data on EFD transition in Fe_3O_4 differ one way or another from the behavior of other resistive switching systems, making the investigation process effectively "from scratch". This work has answered some questions, but definitely more work needs to be done to fully understand the mechanism of EFD transition in magnetite.

Electrical measurements by applying voltage in a pulsed manner demonstrated that the origin of hysteresis in I-V curves is Joule heating of the channel once the system switches to On state. The shortest pulse width available in our experimental setup was 500 μs (HP 4155A semiconductor parameter analyzer). The logical continuation would be to make experiments by applying shorter pulses (with pulse generator down to 10 nm) to determine a switching speed or to make time-resolved measurements with oscilloscope to trace *in situ* the heating of the channel as voltage pulse is applied and cooling between two consequent pulse application. In this way, resistance value might be an indirect indicator of a current temperature.

In the escape-field model, discussed in sec. 5.5, the width of the field distribution is dependent on the *rate* the field is applied. Thus, it would be interesting to collect V_{sw} histograms while applying voltage with various sweep rates. It can be experimentally implemented using data acquisition system (DAQ) to source voltage in a triangular waveform with different frequencies, f; and measuring the current with current amplifier.

Another experiment to continue this work might be field-effect transistor measurements in a top gate configuration using polymer-electrolyte as a gate dielectric as described in detail in introductory Chapter 1.

Four-terminal measurements on the same and different contact metal devices gave valuable information about the mechanism of EFD transition in magnetite. We suggested a charge gap closure in the presence of high enough magnetic field, theoretically predicted for correlated insulators [102], as an origin of EFD transition. More detailed statistical V_{sw} distribution measurements with and without application of magnetic field were supposed to give deeper insight into the mechanism of the trantion but not all experimental results can be explained so far. The theoretical work and modeling are of need to make a final conclusion and is currently underway.

In addition to the investigation of EFD transition in magnetite in this work we have developed a technique to produce high-aspect-ratio (HAR) nanogaps. The latter might be used for electrical characterization of numerous systems, which are otherwise not addressible. We have demonstrated a successfull applicability of HAR gap to study EFD transition in Fe_3O_4. Besides, HAR method was applied in our laboratory to study other systems such as organic semiconductors and to prepare junctions to observe surface enhanced Raman spectroscopy.

Bibliography

[1] P.A. Miles, W.B. Westphal, and V.A. Hippel, "Dielectric spectroscopy of ferromagnetic semiconductors," *Rev. Mod. Phys.*, vol. 29, pp. 279–307, 1957.

[2] J. P. Shepherd, J. W. Koenitzer, R. Aragón, C. J. Sandberg, and J. M. Honig. "Heat capacity studies on single crystal annealed Fe_3O_4," *Phys. Rev. B*, vol.31, pp. 1107–1113, 1985.

[3] F. Walz. "The verwey transitiona topical review,", *J. Phys.: Condens. Matter.*, vol. 14, pp. R285–R340, 2002.

[4] J. M. Zuo, J. C. H. Spence, and W. Petuskey. "Charge ordering in magnetite at low temperatures," *Phys. Rev. B*, vol. 42, pp. 8451–8464, 1990.

[5] D. L. Camphausen, J. M. D. Coey, and B. K. Chakraverty. "One-electron energy levels in Fe_3O_4," *Phys. Rev. Lett.*, vol. 29, pp. 657–660, 1972.

[6] G. Kh. Rozenberg, G. R. Hearne, M. P. Pasternak, P. A. Metcalf, and J. M. Honig. "Nature of the verwey transition in magnetite (Fe_3O_4) to pressures of 16 GPa,". *Phys. Rev. B*, vol. 53, pp. 6482–6487, 1996.

[7] P. Jiwoong, A. N. Pasupathy, J. I. Goldsmith, C. Chang, Y. Yaish, J. R. Petta, M. Rinkoski, J. P. Sethna, H. D. Abruña, P. L. McEuen, and D. C. Ralph. "Coulomb blockade and the kondo effect in single-atom transistors," *Nature*, vol. 417, pp. 722–725, 2002.

[8] H. Park, J. Park, A. K. L. Lim, E. H. Anderson, A. P. Alivisatos, and P. L. McEuen. “Nanomechanical oscillations in a single-$C_6$0 transistor,”. *Nature*, vol. 407, pp. 57–60, 2000.

[9] D. L. Klein, R. Roth, A. K. L. Lim, A. P. Alivisatos, and P. L. McEuen. “A single-electron transistor made from a cadmium selenide nanocrystal,” *Nature*, vol. 389, pp. 699–701, 1997.

[10] S. Lee, A. Fursina, J. T. Mayo, C. T. Yavuz, V. L. Colvin, R. G. S. Sofin, I. V. Shvets, and D. Natelson. “Electrically-driven phase transition in magnetite nanostructures,” *Nature Mater.*, vol. 7, pp. 130–133, 2008.

[11] M.J. Panzer and C.D. Frisbie. “Polymer electrolyte-gated organic field-effect transistors: Low-voltage, high-current switches for organic electronics and testbeds for probing electrical transport at high charge carrier density,” *J. Am. Chem. Soc.*, vol. 129, pp. 6599–6607, 2007.

[12] A. Sawa. “Resistive switching in transition metal oxides,” *Mater. Today*, vol. 11, pp. 28–36, 2008.

[13] R. Waser. “Resistive non-volatile memory devices,” *Microelectron. Eng.*, vol. 86, pp. 1925-1928, 2009.

[14] Jasprit Singh. *Semiconductor Devices: Basic Principles.* John-Wiley, 2001.

[15] M. Sahu, M.-H. Bae, A. Rogachev, D. Pekker, T.-C. Wei, N. Shah, P. M. Goldbart, and A. Bezryadin. “Individual topological tunnelling events of a quantum field probed through their macroscopic consequences,” *Nature Phys.*, vol. 5, pp. 503–508, 2009.

[16] D. R. Ward, N. K. Grady, C. S. Levin, N. J. Halas, Y. Wu, P. Nordlander, and D. Natelson. “Electromigrated nanoscale gaps for surface-enhanced Raman spectroscopy,” *Nano Lett.*, vol. 7, pp. 1396–1400, 2007.

[17] D. Natelson, L. H. Yu, J. W. Ciszek, Z. K. Keane, and J. M. Tour. “Single-molecule transistors: Electron transfer in the solid state,” *Chem. Phys.*, vol. 324, pp. 267–275, 2006.

[18] B. H. Hamadani and D. Natelson. “Nonlinear charge injection in organic field-effect transistors.” *J. Appl. Phys.*, vol. 97, pp. 064508, 2005.

[19] L. H. Yu, Z. K. Keane, J. W. Ciszek, L. Cheng, J. M. Tour, T. Baruah, M. R. Pederson, and D. Natelson. “Kondo resonances and anomalous gate dependence in the electrical conductivity of single-molecule transistors,” *Phys. Rev. Lett.*, vol. 95, pp. 256803, 2005.

[20] L. H. Yu, Z. K. Keane, J. W. Ciszek, L. Cheng, M. P. Stewart, and J. M. Tourand, and D. Natelson. “Inelastic electron tunneling via molecular vibrations in single-molecule transistors,” *Phys. Rev. Lett.*, vol. 93, pp. 266802, 2004.

[21] S. Lee, A. Trionfi, T. Schallenberg, H. Munekata, and D. Natelson. “Mesoscopic conductance effects in inmnas structures,” *Appl. Phys. Lett.*, vol. 90, pp. 032105, 2007.

[22] H. Park, A. K. L. Lim, A. P. Alivisatos, J. Park, and P. L. McEuen. “Fabrication of metallic electrodes with nanometer separation by electromigration,” *Appl. Phys. Lett.*, vol. 75, pp. 301–303, 1999.

[23] D. R. Strachan, D. E. Smith, D. E. Johnston, T.-H. Park, M. J. Therien, D. A. Bonnell, and A. T. Johnson. “Controlled fabrication of nanogaps in ambient

environment for molecular electronics," *Appl. Phys. Lett.*, vol. 86, pp. 043109, 2005.

[24] P. Jiwoong, A. N. Pasupathy, J. I. Goldsmith, C. Chang, Y. Yaish, J. R. Petta, M. Rinkoski, J. P. Sethna, H. D. Abruña, P. L. McEuen, and D. C. Ralph. "Coulomb blockade and the kondo effect in single-atom transistors," *Nature*, vol. 417, pp. 722–725, 2002.

[25] Y. V. Kervennic, H. S. J. Van der Zant, A. F. Morpurgo, L. Gurevich, and L. P. Kouwenhoven. "Nanometer-spaced electrodes with calibrated separation," *Appl. Phys. Lett.*, vol. 80, pp. 321–323, 2002.

[26] C. Z. Li, H. X. He, and N. J. Tao. "Quantized tunneling current in the metallic nanogaps formed by electrodeposition and etching," *Appl. Phys. Lett.*, vol. 77, pp. 3995–3997, 2000.

[27] M. A. Reed, C. Zhou, C. J. Muller, T. P. Burgin, and J. M. Tour. "Conductance of a molecular junction," *Science*, vol. 278, pp. 252–254, 1997.

[28] M. A. Guillorn, D. W. Carr, R. C. Tiberio, E.Greenbaum, and M. L. Simpson. "Fabrication of dissimilar metal electrodes with nanometer interelectrode distance for molecular electronic device characterization." *J. Vac. Sci. Technol. B*, vol. 18, pp. 1177–1181, 2000.

[29] M. D. Fischbein and M. Drndić. "Sub-10 nm device fabrication in a transmission electron microscope," *Nano Lett.*, vol. 7, pp. 1329–1327, 2007.

[30] K. Liu, Ph. Avouris, J. Bucchignano, R. Martel, S. Sun, and J. Michl. "Simple fabrication scheme for sub-10 nm electrode gaps using electronbeam lithography," *Appl. Phys. Lett.*, vol. 80, pp. 865–867, 2002.

[31] B.P. Van der Gaad and A. Scherer. “Microfabrication below 10 nm,” *Appl. Phys. Lett.*, vol. 56, pp. 481–483, 1990.

[32] M. D. Fischbein and M. Drndić. “Nanogaps by direct lithography for high-resolution imaging and electronic characterization of nanostructures.” *Appl. Phys. Lett.*, vol. 88, pp. 063116, 2006.

[33] L. Qin, S. Park, L. Huang, and C. A. Mirkin. “On-wire lithography,” *Science*, vol. 309, pp. 113–115, 2005.

[34] S. M. Luber, S. Strobel, H.-P. Tranitz, W. Wegscheider, D. Schuh, and M. Tornow. “Nanometre spaced electrodes on a cleaved algaas surface,” *Nanotechnology*, vol. 16, pp. 1182–1185, 2005.

[35] S. M. Luber, F. Zhang, S. Lingitz, A. G. Hansen, F. Scheliga, E. Thorn-Csányi, M. Bichler, and M. Tornow. “High-aspect-ratio nanogap electrodes for averaging molecular conductance measurements,” *Small*, vol. 3, pp. 285–289, 2007.

[36] J. Tang, Y. Wang, C. Nuckolls, and S. J. Wind. “Chemically responsive molecular transistors fabricated by self-aligned lithography and chemical self-assembly,” *J. Vac. Sci. Tech. B*, vol. 24, pp. 3227–3229, 2006.

[37] J. Tang, Y. Wang, C. Nuckolls, and S. J. Wind. “Single-molecule transistor fabrication by self-aligned,” *Microelectron. Eng.*, vol. 83, pp. 1706–1709, 2006.

[38] K. R. Williams, K. Gupta, and M. Wasilik. “Etch rates for micromachining processing — Part II,” *J. Microelectromech. Syst.*, vol. 12, pp. 761–778, 2003.

[39] E. J. W. Verwey. “Electronic conduction of magnetite (Fe_3O_4) and its transition point at low temperatures,” *Nature*, vol. 144, pp. 327–328, 1939.

[40] E. J. Verwey, P. W. Haayman, and F. C. Romeijn. “Physical properties and cation arrangement of oxides with spinel structures II. electronic conductivity,” *J. Chem. Phys.*, vol. 15, pp. 181–187, 1947.

[41] M. Imada, A. Fujimori, and Y. Tokura. “Metal-insulator transitions,” *Rev. Mod. Phys.*, vol. 70, pp. 1039–1263, 1998.

[42] M. Coey. “Condensed-matter physics: Charge-ordering in oxides,” *Nature*, vol. 430, pp. 155–157, 2004.

[43] J. Garcia and G. Subias. “The Verwey transition - a new perspective,” *J. Phys.: Condens. Matter.*, vol. 16, pp. R145–R178, 2004.

[44] R. Aragón, D. J. Buttrey, J. P. Shepherd, and J. M. Honig. “Influence of nonstoichiometry on the Verwey transition,” *Phys. Rev. B*, vol. 31, pp. 430–436, 1985.

[45] R. Aragón, R. J. Rasmussen, J. P. Shepherd, J. W. Koenitzer, and J. M. Honig. “Effect of stoichiometry changes on electrical properties of magnetite,” *J. Magn. Magn. Mater.*, vol. 54-57, pp. 1335–1336, 1985.

[46] J. P. Shepherd, J. W. Koenitzer, R. Aragón, J. Spalek, and J. M. Honig. “Heat capacity and entropy of nonstoichiometric magnetite $Fe_{3(1-\delta)}O_4$: The thermodynamic nature of the Verwey transition,” *Phys. Rev. B*, vol. 43, pp. 8461–8471, 1991.

[47] E. Nazarenko, J. E. Lorenzo, Y. Joly, J. L. Hodeau, D. Mannix, and C. Marin. “Resonant X-rat diffraction studies on the charge ordering in magnetite,” *Phys. Rev. Lett.*, vol.97, pp. 056403, 2006.

[48] R. J. Goff, J. P. Wright, J. P. Attfield, and P. G. Radaelli. "Resonant X-ray diffraction study of the charge ordering in magnetite," *J. Phys.: Condens. Matter.*, vol. 17, pp. 7633–7642, 2005.

[49] J. García, G. Subías, M. G. Proietti, H. Renevier, Y. Joly, J. L. Hodeau, J. Blasco, M. C. Sánchez, and J. F. Bérar. "Resonant "forbidden" reflections in magnetite," *Phys. Rev. Lett.*, vol. 85, pp. 578–581, 2000.

[50] P. Piekarz, K. Parlinski, and A. M. Oles. "Origin of the Verwey transition in magnetite: Group theory, electronic structure, and lattice dynamics study." *Phys. Rev. B*, vol. 76, pp. 165124, 2007.

[51] E. J. W. Verwey and E. L. Heilmann. "Physical properties and cation arrangement of oxides with spinel structures I. cation arrangement in spinels," *J. Chem. Phys.*, vol. 15, pp. 174–180, 1947.

[52] E. J. Samuelsen, E. J. Bleeker, L. Dobrzynski, and T. Riste. "Neutron scattering from magnetite below 119 K" *J. Appl. Phys.*, vol. 39, pp. 1114–1115, 1968.

[53] T. Yamada, K. Suzuki, and S. Chikazumi. "Electron microscopy of orthorhombic phase in magnetite," *Appl. Phys. Lett.*, vol. 13, pp. 172–174, 1968.

[54] M. Iizumi, T.F. Koetzle, G. Shirane, S. Chikazumi, M. Matsui, and S. Todo. "Structure of magnetite (Fe_3O_4) below the Verwey transition temperature," *Acta Crystallogr. B*, vol. 38, pp. 2121–2133, 1982.

[55] P. G. Radaelli J. P. Wright, J. P. Attfield. "Long range charge ordering in magnetite below the Verwey transition," *Phys. Rev. Lett.*, vol. 87, pp. 266401, 2001.

[56] G. Subías, J. García, J. Blasco, M. G. Proietti, H. Renevier, and M. C. Sánchez. "Magnetite, a model system for mixed-valence oxides, does not show charge ordering," *Phys. Rev. Lett.*, vol. 93, pp. 156408, 2004.

[57] D. J. Huang, H.-J. Lin, J. Okamoto, K. S. Chao, H.-T. Jeng, G. Y. Guo, C.-H. Hsu, C.-M. Huang, D. C. Ling, W. B. Wu, C. S. Yang, and C. T. Chen. "Charge-orbital ordering and Verwey transition in magnetite measured by resonant soft X-rat scattering," *Phys. Rev. Lett.*, vol. 96, pp. 096401, 2006.

[58] M. Rubinstein and D. W. Forester. "Investigation of the insulating phase of magnetite by NMR and the Mössbauer effect." *Solid State Com.*, vol. 9, pp. 1675–1679, 1971.

[59] F. J. Berry, S. Skinner, and M. F. Thomas. "Mössbauer spectroscopic examination of a single crystal of Fe_3O_4." *J. Phys.: Condens. Matter.*, vol. 10, pp. 215–220, 1998.

[60] P. Novák, H. Štěpánková, J. Englich, J. Kohout, and V. A. M. Brabers. "NMR in magnetite below and around the Verwey transition," *Phys. Rev. B*, vol. 61, pp. 1256–1260, 2000.

[61] L. V. Gasparov, D. B. Tanner, D. B. Romero, H. Berger, G. Margaritondo, and L. Forró. "Infrared and Raman studies of the Verwey transition in magnetite." *Phys. Rev. B*, vol. 62, pp. 7939–7944, 2000.

[62] B. Handke, A. Kozlowski, K. Parliński, J. Przewoźnik, T. Ślezak, A. I. Chumakov, L. Niesen, Z. Kakol, and J. Korecki. "Experimental and theoretical studies of vibrational density of states in Fe_3O_4 single-crystalline thin films." *Phys. Rev. B*, vol. 71, pp. 144301, 2005.

[63] H. Seo, M. Ogata, and H. Fukuyama. “Aspects of the Verwey transition in magnetite,” *Phys. Rev. B*, vol. 65, pp. 085107, 2002.

[64] A. Chainani, T. Yokoya, T. Morimoto, T. Takahashi, and S. Todo. “High-resolution photoemission spectroscopy of the Verwey transition in Fe_3O_4.” *Phys. Rev. B*, vol. 51, pp. 17976–17979, 1995.

[65] P. Poddar, T. Fried, G. Markovich, A. Sharoni, D. Katz, T. Wizansky, and O. Millo. “Manifestation of the Verwey transition in the tunneling spectra of magnetite nanocrystals,” *Europhys. Lett.*, vol. 64, pp. 98–103, 2003.

[66] J.-H. Park, L. H. Tjeng, J. W. Allen, P. Metcalf, and C. T. Chen. “Single-particle gap above the Verwey transition in Fe_3O_4,” *Phys. Rev. B*, vol. 55, pp. 12813–12817, 1997.

[67] D. Schrupp, M. Sing, M. Tsunekawa, H. Fujiwara, S. Kasai, A. Sekiyama, S. Suga, T. Muro, V. A. M. Brabers, and R. Claessen. “High-energy photoemission on Fe_33O_4: Small polaron physics and the Verwey transition,” *Europhys. Lett.*, vol. 70, pp. 789–795, 2005.

[68] K. Jordan, A. Cazacu, G. Manai, S. F. Ceballos, S. Murphy, and I. V. Shvets. “Scanning tunneling spectroscopy study of the electronic structure of Fe_3O_4 surfaces,” *Phys. Rev. B*, vol. 74, pp. 085416, 2006.

[69] D. Natelson, L. H. Yu, J. W. Ciszek, Z. K. Keane, and J. M. Tour. “Single-molecule transistors: Electron transfer in the solid state.” *Chem. Phys.*, vol. 324, pp. 267-275, 2006.

[70] W. W. Yu, J. C. Falkner, C. T. Yavuz, and V. L. Colvin. “Synthesis of monodisperse iron oxide nanocrystals by thermal decomposition of iron carboxylate

salts," *Chem. Commun.*, pp. 2306–2307, 2004.

[71] P. J. Freud and A. Z. Hed. “”Dynamics of the electric-field-induced conductivity transition in magnetite. *Phys. Rev. Lett.*, vol. 23, pp. 1440–1443, 1969.

[72] T. Burch, P. P. Craig, C. Hedrick, T. A. Kitchens, J. I. Budnick, J. A. Cannon, M. Lipsicas, and D. Mattis. "Switching in magnetite: A thermally driven magnetic phase transition," *Phys. Rev. Lett.*, vol. 23, pp. 1444–1447, 1969.

[73] A. Salazar, A. Oleaga, A. Wiechec, Z. Tarnawski, and A. Kozlowski. "Thermal diffusivity of $Fe_{3-x}Zn_xO_4$," *IEEE Trans. Magn.*, vol. 40, pp. 2820–2822, 2007.

[74] M.J. Panzer and C.D. Frisbie. "High carrier density and metallic conductivity in poly(3-hexylthiophene) achieved by electrostatic charge injection." *Adv. Func. Mater.*, vol. 16, pp. 1051–1056, 2006.

[75] R. Waser and M. Aono. "Nanoionics-based resistive switching memories," *Nat. Mater.*, vol. 6, pp. 833–840, 2007.

[76] A. Beck, J. G. Bednorz, Ch. Gerber, C. Rossel, and D. Widmer. "Reproducible switching effect in thin oxide films for memory applications," *Appl. Phys. Lett.*, vol. 77, pp. 139–141, 2000.

[77] I. G. Baek, M. S. Lee, S. Seo, M. J. Lee, D. H. Seo, D.-S. Suh, J. C. Park, S. O. Park, H. S. Kim, I. K. Yoo, U-In Chung, and I. T. Moon. "Highly scalable non-volatile resistive memory using simple binary oxide driven by asymmetric unipolar voltage pulses," *Tech. Dig. IEDM*, vol. 4, pp. 587–590, 2004.

[78] B. J. Choi, D. S. Jeong, S. K. Kim, C. Rohde, S. Choi, J. H. Oh, H. J. Kim, C. S. Hwang, K. Szot, R. Waser, B. Reichenberg, and S. Tiedke. "Resistive

switching mechanism of TiO_2 thin films grown by atomic-layer deposition," *J. Appl. Phys.*, vol. 98, pp. 033715, 2005.

[79] R. S. Potember, T. O. Poehler, and D. O. Cowan. "Electrical switching and memory phenomena in Cu-TCNQ thin films," *Appl. Phys. Lett.*, vol. 34, pp. 405–407, 1979.

[80] L. Ma, S Pyo, J Ouyang, Q Xu, and Y Yang. "Nonvolatile electrical bistability of organic/metal-nanocluster/organic system," *Appl. Phys. Lett.*, vol. 82, pp. 1419–1421, 2003.

[81] J. C. Scott and L. D. Bozano. "Nonvolatile memory elements based on organic materials," *Adv. Mater.*, vol. 19, pp. 1452–1463, 2007.

[82] A. Asamitsu, Y. Tomioka, H. Kuwahara, and Y. Tokura. "Current switching of resistive states in magnetoresistive manganites," *Nature*, vol. 388, pp. 50–52, 1997.

[83] K. Szot, W. Speier, G. Bihlmayer, and R. Waser. "Switching the electrical resistance of individual dislocations in single-crystalline $SrTiO_3$," *Nat. Mater.*, vol. 5, pp. 312–320, 2006.

[84] Y. Taguchi, T. Matsumoto, and Y. Tokura. "Dielectric breakdown of one-dimensional Mott insulators Sr_2CuO_3 and $SrCuO_2$," *Phys. Rev. B*, vol. 62, pp. 7015–7018, 2000.

[85] D. C. Kim, S. Seo, S. E. Ahn, D.-S. Suh, M. J. Lee, B.-H. Park, I. K. Yoo, I. G. Baek, H.-J. Kim, E. K. Yim, J. E. Lee, S. O. Park, H. S. Kim, U-In Chung, J. T. Moon, and B. I. Ryu. "Electrical observations of filamentary conductions

for the resistive memory switching in NiO films," *Appl. Phys. Lett.*, vol. 88, pp. 202102, 2006.

[86] S. K. Arora, H.-C. Wu H. Yao, W. Y. Ching, R. J. Choudhary, I. V. Shvets, and O. N. Mryasov. "Magnetic properties of ultrathin magnetite films grown by molecular beam epitaxy," *IEEE Trans. Magn.*, vol. 44, pp. 2628–2631, 2008.

[87] Y. Zhou, X. Jin, and I. V. Shvets. "Enhancement of the magnetization saturation in magnetite (100) epitaxial films by thermo-chemical treatment". *J. Appl. Phys*, vol. 95, pp. 7357–7359, 2004.

[88] A. Koblischka-Veneva, M. R. Koblischka, Y. Zhou, S. Murphy, F. Muücklich, U. Hartmann , and I. V. Shvets "Electron backscatter diffraction analysis applied to [001] magnetite thin films grown on MgO substrates." *J. Magn. Magn. Mater.*, vol. 316, pp. 663–665, 2007.

[89] S. K. Arora, R. G. S. Sofin, I. V. Shvets, and M. Luysberg. "Anomalous strain relaxation behavior of Fe_3O_4/MgO (100) heteroepitaxial system grown using molecular beam epitaxy." *J. Appl. Phys.*, vol. 100, pp. 073908, 2006.

[90] J. Yan, G.V.R. Rao, M. Barela, D.A. Brevnov, Y. Jiang, H. Xu, G.P. López, and P.B. Atanassov. "Growth of patterned nanopore arrays of anodic aluminum oxide." *Adv. Mater.*, vol. 15, pp. 2015–2018, 2003.

[91] H. Asoh, A. Oide, and S. Ono. "Fabrication of self-ordered nanohole arrays on si by localized anodization and subsequent chemical etching," *Appl. Surf. Sci.*, vol. 252, pp. 1668–1673, 2005.

[92] D. J. Young and M. Cohen. "Oxidation behavior of chromium between 300°C and 600°C," *J. Electrochem. Soc.*, vol. 124, pp. 769–86, 1977.

[93] R.J. Hussey, D.F. Mitchell, and M.J. Graham. "The growth and structure of oxide films formed on single crystal (100) and polycrystalline Cr between 550 and 900°C," *Werkstoffe und Korrosion*, vol. 38, pp. 575–583, 1987.

[94] D. Caplan and G. I. Sproule. "Effect of oxide grain structure on the high-temperature oxidation of Cr," *Oxid. Met.*, vol. 9, pp. 459–472, 1975.

[95] Y. Zhou, X. Jin, and I. V. Shvets. "Enhancement of the magnetization saturation in magnetite, (100) epitaxial films by thermo-chemical treatment," *J. Appl. Phys*, vol. 95, pp. 7357–7359, 2004.

[96] K. Szot, R. Dittmann, W. Speier, and R. Waser. "Nanoscale resistive switching in $SrTiO_3$ thin films,". *Phys. Status Solidi*, vol. 1, pp. R86–R88, 2007.

[97] C Li, X Zhang, Cheng, and Y Sun. "Electric field induced phase transition in charge-ordered $LuFe_2O_4$," *Appl. Phys. Lett.*, vol. 93, pp. 152103, 2008.

[98] L. J. Zeng, H. X. Yang, Y Zhang, H. F. Tian, C Ma, Y. B. Qin, Y. G. Zhao, and J. Q. Li. "Nonlinear current-voltage behavior and electrically driven phase transition in charge-frustrated $LuFe_2O_4$," *Europhys. Lett.*, vol. 84, pp. 57011, 2008.

[99] A. Fursina, S. Lee, R. G. S. Sofin, I. V. Shvets, and D. Natelson. "Nanogaps with very large aspect ratios for electrical measurements," *Appl. Phys. Lett.*, vol. 92, pp. 113102, 2008.

[100] S. Volz. *Microscale and Nanoscale Heat Transfer.* Springer-Verlag Berlin Heidelberg, 2007.

[101] J. W. McPherson, J. Kim, A. Shanware, H. Mogul, and J. Rodriguez. "Trends in the ultimate breakdown strength of high dielectric-constant materials," *IEEE*

Trans. Electron Devices, vol. 50, pp. 1771–1778 , 2003.

[102] N. Sugimoto, S. Onoda, and N. Nagaosa. "Field-induced metal-insulator transition and switching phenomenon in correlated insulators," *Phys. Rev. B*, vol. 78, pp. 155104, 2008.

[103] A. A. Fursina, R. G. S. Sofin, I. V. Shvets, and D. Natelson. "The origin of hysteresis in resistive switching in magnetite is Joule heating," *Phys. Rev. B*, vol. 79, pp. 245131, 2009.

[104] Y. B. Nian, J. Strozier, N. J. Wu, X. Chen, and A. Ignatiev. "Evidence for an oxygen diffusion model for the electric pulse induced resistance change effect in transition-metal oxides," *Phys. Rev. Lett.*, vol. 98, pp. 146403, 2007.

[105] M. Quintero, P. Levy, A. G. Leyva, and M. J. Rozenberg. "Mechanism of electric-pulse-induced resistance switching in manganites," *Phys. Rev. Lett.*, vol. 98, pp. 116601, 2007.

[106] A. Chainani, T. Yokoya, T. Morimoto, T. Takahashi, and S. Todo. "High-resolution photoemission spectroscopy of the Verwey transition in Fe_3O_4," *Phys. Rev. B*, vol. 51, pp. 17976–17979, 1995.

[107] D. Schrupp, M. Sing, M. Tsunekawa, H. Fujiwara, S. Kasai, A. Sekiyama, S. Suga, T. Muro, V. A. M. Brabers, and R. Claessen. "High-energy photoemission on Fe_3O_4: Small polaron physics and the Verwey transition," *Europhys. Lett.*, vol. 70, pp. 789–795, 2005.

[108] S. K. Park, T. Ishikawa, and Y. Tokura. "Charge-gap formation upon the Verwey transition in Fe_3O_4," *Phys. Rev. B*, 58(7):3717–3720, 1998.

[109] A. Pimenov, S. Tachos, T. Rudolf, A. Loidl, S. Schrupp, M. Sing, R. Claessen, and V. A. M Brabers. "Terahertz conductivity at the Verwey transition in magnetite," *Phys. Rev. B*, vol. 72, pp. 035131, 2005.

[110] M. Fonin, Yu. S Dedkov, R. Pentcheva, U. Rüdiger, and G. Güntherodt. "Magnetite: a search for the half-metallic state," *J. Phys.: Condens. Matter*, vol. 19, pp. 315217, 2007.

[111] A. Yanase and K. Siratori. "Band structure in the high temperature phase of Fe_3O_4," *J. Phys. Soc. Jpn.*, vol. 53, pp. 312–317, 1984.

[112] T. Oka, R. Arita, and H. Aoki. "Breakdown of Mott insulator: a nonadiabatic tunneling mechanism," *Phys. Rev. Lett*, vol. 91, pp. 066406, 2003.

[113] V. Kiryukhin, D. Casa, J. P. Hill, B. Keimer, A. Vigliante, Y. Tomioka, and Y. Tokura. "An X-ray-induced insulator-metal transition in a magnetoresistive manganite," *Nature*, vol. 386, pp. 813–815, 1997.

[114] S. Yamanouchi, Y. Taguchi, and Y. Tokura. "Dielectric breakdown of the insulating charge-ordered state in $La_{2-x}Sr_xNiO_4$," *Phys. Rev. Lett.*, vol. 83, pp. 5555–5558, 1999.

[115] H. B. Michaelson. "The work function of the elements and its periodicity," *J. Appl. Phys.*, vol. 48, pp. 4729–4733, 1977.

[116] M Fonin, R Pentcheva, Yu. S. Dedkov, M Sperlich, D. V. Vyalikh, M. Scheffler, U. Rüdiger, and G Güntherodt. "Surface electronic structure of the Fe_3O_4 (100): Evidence of a half-metal to metal transition," *Phys. Rev. B*, vol. 72, pp. 104436, 2005.

[117] V. V. Shchennikov, S. V. Ovsyannikov, A. E. Karkin, S. Todob, and Y Uwatokob. “Galvanomagnetic properties of fast neutron bombarded Fe_3O_4 magnetite: A case against charge ordering mechanism of the Verwey transition,” *Solid State Commun.*, vol. 149, pp. 759–762, 2009.

[118] D Kim and J. M. Honig. “Seebeck coefficients of $Fe_{3-y}Ti_yO_4$ and $Fe_{3-x}Zn_xO_4$ single crystals and their interpretation,” *Phys. Rev. B*, vol. 49, pp. 4438–4444, 1994.

[119] T. Tokunaga, Y. Kaneko, J. P. He, T. Arima, A. Sawa, T. Fujii, M. Kawasaki, and Y. Tokura. “Colossal electroresistance effect at metal electrode/$La_{1-x}Sr_{1+x}MnO_4$ interfaces,” *Appl. Phys. Lett.*, vol. 88, pp. 223507, 2006.

[120] N. Shah, D. Pekker, and P. M. Goldbart. “Inherent stochasticity of superconductor-resistor switching behavior in nanowires,” *Phys. Rev. Lett.*, vol. 101, pp. 207001, 2008.

[121] R. Varga, K. L. García, M. Vázquez, A. Zhukov, and P. Vojtanik. “Switching-field distribution in amorphous magnetic bistable microwires,” *Phys. Rev. B*, vol. 70, pp. 024402, 2004.

[122] R. G. S. Sofin, S. K. Arora, and I. V. Shvets. “Study of magnetoresistance of epitaxial magnetite films grown on vicinal MgO (100) substrate,” *J. Appl. Phys.*, vol. 97, pp. 10D315, 2005.

[123] J. M. De Teresa, A. Fernández-Pacheco, L Morellon, J. Orna, J. A. Pardo, D. Serrate, P. A. Algarabel, and M. R. Ibarra. “Magnetotransport properties of Fe_3O_4 thin films for applications in spin electronics,” *Micro. Engn.*, vol. 84, pp. 16601664, 2007.

[124] A. Garg. "Escape-field distribution for escape from a metastable potential well subject to a steadily increasing bias field," *Phys. Rev. B*, vol. 51, pp. 15592–15595, 1995.

List of Publications

S. Lee, A. A. Fursina, J. T. Mayo, C. T. Yavuz, V. L. Colvin, R. G. S. Sofin, I. V. Shvets and D. Natelson. "Electrically-Driven Phase Transition in Magnetite Nanostructures," Nature Mater. **7**, 130–134 (2008).

A. A. Fursina, S. Lee, R. G. S. Sofin, I. V. Shvets and D. Natelson. "Nanogaps with Very Large Aspect Ratios for Electrical measurements," Appl. Phys. Lett. **92**, 113102 (2008).

A. A. Fursina, R. G. S. Sofin, I. V. Shvets and D. Natelson. "Origin of Hysteresis in Resistive Switching in Magnetite is Joule Heating," Phys. Rev. B **79**, 245131 (2009).

A. A. Fursina, R. G. S. Sofin, I. V. Shvets and D. Natelson. "Interplay of Bulk and Interface Effects in the Electric-Field-Driven Transition in Magnetite," Phys. Rev. B **81**, 045123 (2010).

A. Sinitskii, A. A. Fursina, D. V. Kosynkin, A. L. Higginbotham, D. Natelson, and J. M. Tour "Electronic Transport in Monolayer Graphene Nanoribbons Produced by Chemical Unzipping of Carbon Nanotubes," Appl. Phys. Lett. **95**, 253108 (2009).

A. Sinitskii, A. Dimiev, D. A. Corley, A. A. Fursina, D. V. Kosynkin, J. M. Tour "Kinetics of Diazonium Functionalization of Chemically Converted Graphene Nanoribbons," ACS Nano, **4**, 1949-1954 (2010).